Modeling, Optimization and Analysis of Electromobility Systems

Domingues, Gabriel

2018

Document Version:
Publisher's PDF, also known as Version of record

Link to publication

Citation for published version (APA):
Domingues, G. (2018). *Modeling, Optimization and Analysis of Electromobility Systems*. Department of Biomedical Engineering, Lund university.

Total number of authors:
1

LUND UNIVERSITY

PO Box 117
221 00 Lund
+46 46-222 00 00

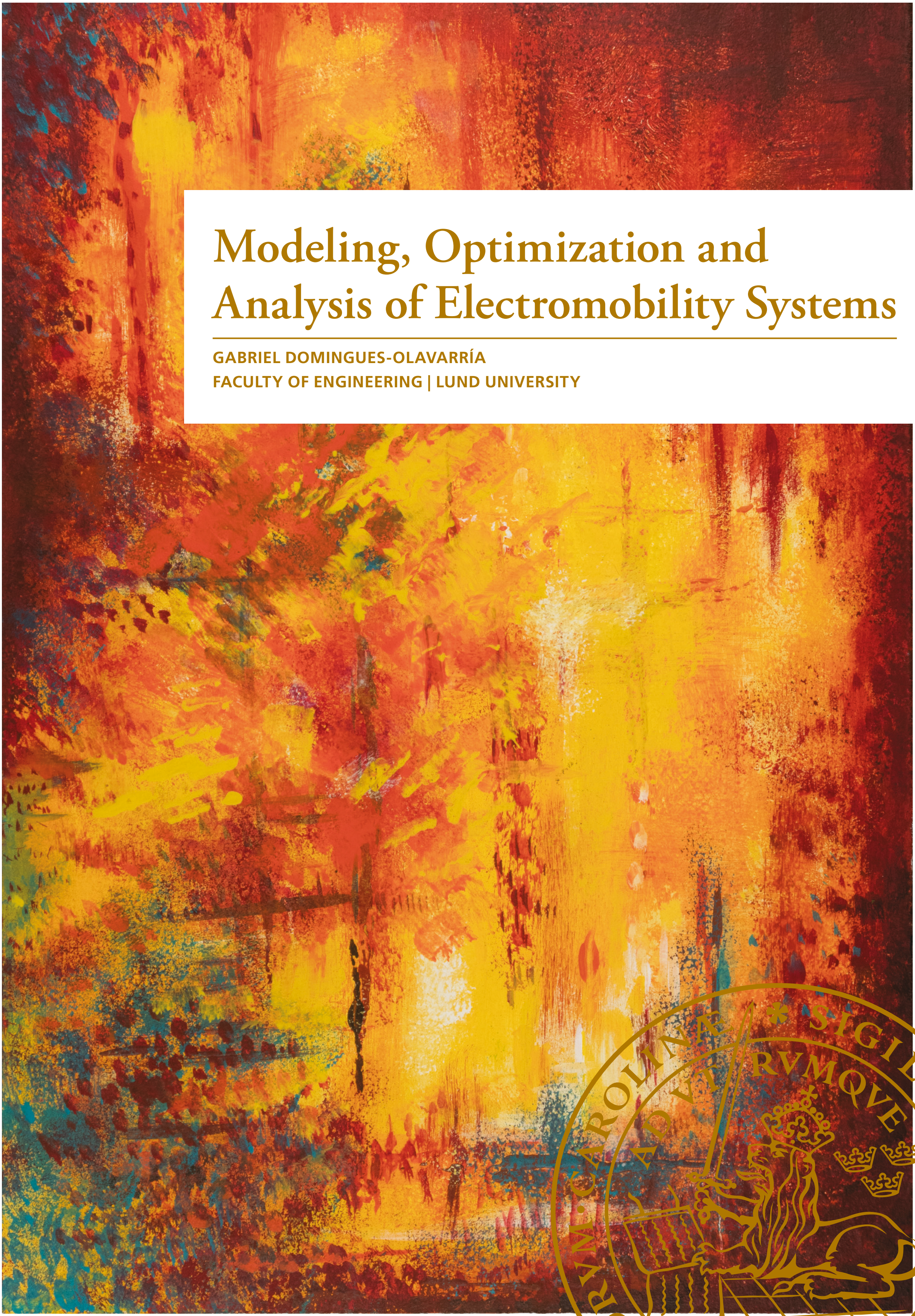

Modeling, Optimization and Analysis of Electromobility Systems

GABRIEL DOMINGUES-OLAVARRÍA
FACULTY OF ENGINEERING | LUND UNIVERSITY

Modeling, Optimization and Analysis of Electromobility Systems

Modeling, Optimization and Analysis of Electromobility Systems

by Gabriel Domingues-Olavarría

LUND
UNIVERSITY

Thesis for the degree Doctor of Philosophy in Engineering
Thesis advisors: Prof. Mats Alaküla, Assoc. Prof. Avo Reinap, Dr. Francisco J. Márquez-Fernández
Faculty opponent: Torbjörn Thiringer

To be presented, with the permission of the Faculty of Engineering of Lund University, for public criticism in the E:1406 lecture hall, Electrical Engineering Building, Ole Römers väg 3 on Friday, the 23th of November 2018 at 10:15.

Organization
LUND UNIVERSITY

Division of Industrial Electrical Engineering and Automation
Box 118, SE–221 00 LUND
Sweden

Document name
DOCTORAL DISSERTATION

Date of disputation
2018-11-23

Sponsoring organization

Author(s)
Gabriel Domingues-Olavarría

Title and subtitle
Modeling, Optimization and Analysis of Electromobility Systems

Abstract

Due to an increase in environmental awareness and an improved understanding on the impact of human activity on our planet's climate, there is a strong desire both from governments and the general public to reduce harmful pollution and emissions. This requires action on different fronts, like decarbonizing electricity generation, industrial activity and not least the transport sector. This thesis aims to contribute to the development of a sustainable road transport system. There are several technologies that could achieve this goal, but the scope of this work is limited to automotive electrification in the form of hybrid and battery electric vehicles. Such vehicles currently seem to be the most promising technology, having a larger market share than e.g fuel cell electric vehicles.

In order to increase the pace of automotive electrification it is necessary to understand the factors that are currently hindering its adoption. First, the higher cost of electrified vehicles when compared with their conventional counterpart is seen by most potential buyers as their main drawback, despite lower operating and maintenance costs. Second, their limited range and long recharging times cause range anxiety on the drivers and generate concerns over the capabilities of the vehicles to provide the expected service and level of convenience. Finally, the lack of charging infrastructure poses a challenge for potential users.

In order to develop an understanding on how to address these issues, the present work takes a holistic approach that starts with the development of performance and cost models for the main components required in an electromobility system. These models are used to optimize the design of an electric powertrain for passenger vehicles. Three electrical machine topologies and two powertrain concepts are considered in this optimization. The results point out that significant cost benefits can be obtained from an increase in the top speed of the electric traction machine as well as the addition of a second speed to the transmission. Additionally, the developed methodology allows exploring a large space of search in a way that reduces development times and associated costs.

Moving the focus to a higher level of abstraction, the described models are used to analyze the implications of deploying alternative forms of charging infrastructures in a national context. This analysis shows that a large deployment of a dynamic charging infrastructure accessible by both passenger and commercial vehicles significantly reduces the societal cost of electrification. This is due to the possibility of reducing the required battery capacity on-board the vehicles without affecting their driving range.

Key words
Electromobility, Electric Vehicles, Hybrid Vehicles, Charging, Modeling, Optimization

Classification system and/or index terms (if any)

Supplementary bibliographical information

Language
English

ISSN and key title

ISBN
978-91-88934-95-6 (print)
978-91-88934-94-9 (pdf)

Recipient's notes

Number of pages
169

Price

Security classification

I, the undersigned, being the copyright owner of the abstract of the above-mentioned dissertation, hereby grant to all reference sources the permission to publish and disseminate the abstract of the above-mentioned dissertation.

Signature

Date 2018-10-15

Modeling, Optimization and Analysis of Electromobility Systems

by Gabriel Domingues-Olavarría

LUND
UNIVERSITY

Cover illustration front: An abstract painting titled “Energy” from Monica Olavarría, the author’s mother.

Funding information: The thesis work was financially supported the Swedish Energy Agency.

Faculty of Engineering, Division of Industrial Electrical Engineering and Automation

ISBN: 978-91-88934-95-6 (print)
ISBN: 978-91-88934-94-9 (pdf)
CODEN: LUTEDX/(TEIE-1090)/1-169/(2018)

Printed in Sweden by Media-Tryck, Lund University, Lund 2018

"Whether you believe you can do a thing or not –
you are right".
-Henry Ford

Contents

Acknowledgements

Two days before the test print, I'm sitting alone at the university proof reading the thesis once more, looking for that final typo that I would probably not find but I'm sure some of you will. Taking a break from it, I get to think about the road that has brought me here, to write what I hope are the last pages of my PhD thesis. This road has taken me from my home country to the other side of the world (Lars, I know it is technically not the other side of the world, but bear with me here) where I have had the chance of learning a lot of new things and work in a variety of interesting and exciting projects. But the highlight of the journey has been the fantastic group of people that I have had the luxury to share it with, and to whom I would like to thank.

First of all, I would like to express my gratitude to my supervisor Prof. Mats Alakula. Since we first met, you have always been a source of encouragement, motivation and support. After all our meetings, I always left full of ideas and overcharged with energy to tackle new problems. It is an amazing experience to work with you.

I would also like to thank Assoc. Prof. Avo Reinap. Even when you have been full of work, your door has always been open for me to come in and discuss things with you, from work philosophy to details of electrical machines. You understood that in most cases I did not need a straight answer, but rather something to think about.

My gratitude goes also to Dr. Francisco Marquez. Fran, despite your age, you are the kind of person that is always willing to help and motivate others. In many ways, you are one of the people that made this work possible.

My very cheerful and optimistic honorary Mexican, Pontus Fyhr, also deserves a big thank. I have learned a lot from our discussions, your many lessons on mechanical engineering and even our arguments over the selection of variable names.

I would also like to thanks all my colleagues at the division of Industrial Electrical Engineering and Automation (IEA) of Lund University, for fostering an amazing work environment full of interesting discussions and exchange of ideas. Especially, I want to thank Ulf Jeppsson, Ulrika Westerdahl, Carina Lindström and Getachew Darge, for all the amazing and hard work you guys do for our division. Additionally, I would like to thank all of those that at one point or another were my fellow PhD students and lunch companions: Sebb, Anton, Phil, Bobbie, Max, Lars, Rasmus, Zhe, Evripidis, Xavi, Sam, and all others for sharing this journey with me, you are awesome!

I want to express my gratitude to all the people involved in the HighSpeed and MFEA projects. In particular I would like to thank Kristoffer Nilsson, Gustaf Lagunoff, Anders Göransson, Karin Carlsson and Henrik Engdahl, for sharing your knowledge and pushing the projects forward. It has been great to work with all of you.

But not all in life is work and therefore, I would like to thank all my friends that one way or another helped me remain sane through this journey: Aless, Reinaldo, Vero, Cesar, David, Mingo, Ingvi, Aneta, Jonas, Pamela, Johan, Filip, Katarina, Tobias, Björn and Emmy. Those that I have accidentally forgotten to mention, I thank you too!

Marta, Cheché, Simón, Sebastián, Juana, Nelson, Felipe and Luisa, thanks a lot for being my Foster family in Sweden.

I would also like to thank my amazing family, for always being there to encourage and support me no matter how far apart we are. To my little (not so little) cousin, Andrea Ingino, thanks! Not only for helping me read proof the thesis, but also for making me feel closer to home. Mamá y Papá, no me alcanzan las páginas para agradecerles por todo, este logro es de ustedes también! Sofía y Oscar David (A.K.A. Winni), gracias por estar siempre pendiente, aunque estemos lejos, saben que los quiero y siempre pueden contar conmigo. A mi nona, a mi abuela, a mis tíos y primos, gracias por estar siempre ahí, son lo máximo!

Last but definitely not least, I would like to thank my loving girlfriend Ana, for your unconditional support and love throughout my whole PhD. This would not have been possible without you!

Gabriel Domingues-Olavarría
October, 2018

Popular summary

In recent years it has become undeniable that human activity is affecting, in a negative way, our planet's climate. In order to mitigate this situation, efforts are being made to reduce the emissions of greenhouse gases and pollutants to the atmosphere. One of the major contributors to these types of emissions is the transport sector, particularly cars and trucks.

In this context, technologies such as battery electric vehicles (BEVs), fuel-cell vehicles and bio-fuels are among some of the solutions that could enable cleaner road transport. In spite of the wide range of alternatives technologies, recently, BEVs have received remarkable attention, with almost all major OEMs currently producing and selling at least one BEV model.

Although this sounds promising, both the total number of BEVs on the roads as well as their market share are relatively low in comparison to the overall size of the automotive market. In order for BEVs to take a more significant portion of the market they must overcome a series of drawbacks. First, their higher up-front cost when compared to conventional vehicles; second, their limited range and finally the lack of a refueling (charging) infrastructure are the main aspects currently hindering the mass adoption of electric vehicles.

This thesis addresses the issue of developing a sustainable transport system based on BEVs from a holistic perspective. In order to do so, the performance and cost drivers of the main components of the system are identified and modeled. This includes detailed modeling of power electronics converters, electrical machines and mechanical transmissions. At the vehicle level, these models are used in the optimization of electric powertrains while at the transportation system level they are used to analyze the implications of the deployment of alternative charging infrastructure solutions.

As previously mentioned, the developed component models are used to optimize the design of an electric powertrain. In this context, the powertrain for a passenger vehicle, with similar specifications as a Nissan Leaf, is optimized considering three alternative EM topologies and two powertrain configurations. Although it is possible to optimize for different objectives such as reducing energy consumption, weight and/or cost this work aims at minimizing the latter as it tends to be one of the main targets for the automotive industry.

From this optimization study it is possible to conclude that for a cost optimized powertrain, both its cost and weight reduce together with an increase in the gear ratio of the transmission and speed of the electrical machine, for the studied topologies, geometries and materials. Moreover, the addition of a second speed to the transmission enables an increase in the power density of the electrical machine which translates into a lower system cost. One important aspect to keep in mind is that the initial assumptions on the cost of raw materials and components have a great impact on the final results. Therefore, slight variations on these assumptions might result into a different optimal solution.

It is also interesting to adopt a higher level of abstraction to analyze the implications of deploying alternative forms of charging infrastructure. This analysis is particularly relevant nowadays that new technologies to enable dynamic charging of electric vehicles, also known as electric road systems (ERS), are being developed and tested. In this context, this thesis aims to compare the societal cost of implementing both static and dynamic charging infrastructures at a nation-wide level under different scenarios.

Such analysis is performed both for Sweden and Denmark. The results point out that a large scale implementation of a dynamic charging infrastructure, usable by all vehicle types, would significantly decrease the societal cost of road transport electrification. This is due to the fact that this infrastructure facilitates a significant reduction of the battery capacity required on-board the vehicles, especially for passenger cars, which is a dominant driver for the societal cost of road transport electrification.

Nomenclature

$\$_x$	Specific cost of the transmission component x [€/kg]
α_{pm}	Angular pitch of the permanent magnet [rad]
α_{so}	Angular pitch of the slot opening [rad]
α_s	Angular pitch of the slot [rad]
$\hat{B}_c$	Peak flux density in the core [T]
$\hat{I}$	Peak current [A]
μ	Magnetic permeability [H/m]
ω	Angular speed [rad/s]
ω_{opt}	Inertia term for the PSO
ϕ	Pressure angle [deg]
Ψ	Flux linkage [Vs]
$\Re$	Reluctance [1/H]
$\vec{i_{dq}}$	Current vector in the dq plane [A]
$\vec{v_{dq}}$	Voltage vector in the dq plane [V]
A_c	Core cross section area [m^2]
A_p	Area product [m^4]
A_w	Winding cross section area [m^2]
A_{chip}	Semiconductor chip area [mm^2]
B	Width of the contact band [m]

$B_{cap,x}$	Battery capacity for vehicle x [kwh]
$B_{t/y}$	Flux density in tooth or yoke [T]
C_1	Cognitive scaling parameter for PSO
C_2	Social scaling parameter for PSO
C_f	Surface condition factor [-]
C_h	Hardness ratio factor [-]
C_p	Elastic coefficient [Pa$^{0.5}$]
C_{comp}	Depreciated cost of the electromobility related components [€/kWh]
C_{emob}	Electromobility equivalent energy cost [€/kWh]
C_{ERS}	Cost of the ERS segmet [€]
C_e	Electric energy cost [€/kWh]
C_{fuel}	Cost of fossil fuels needed to provide the same amount of tractive energy as 1 kWh of electricity used by an electric powertrain [€/kwh]
C_{inf}	Depreciated cost of the charging infrastructure [€/kWh]
$C_{on-board}$	Cost of on-board components [€]
C_{rate}	Charging/discharging rate of the battery [1/h]
d_c	Core depth at airgap [m]
d_{pp}	Distance between air-pockets [m]
d_{pr}	Distance between air pocket and rotor outer radius [m]
d_{range}	Driving range [km]
$d_{x,year}$	Average yearly driving distance for vehicle x [km]
E	Modulus of elasticity [Pa]
E_{sw}	Switching energy [J]
e_x	Energy consumption per km for vehicle x [kwh/km]
F	Width of the cantilever beam or face width of the gear [m]

f_s	Operating frequency [Hz]
f_{sw}	Switching frequency [Hz]
Fd^2	Volume factor [m^3]
g	Airgap length [m]
h_t	Height of the tooth [m]
h_{ap}	Air-pocket's height [m]
h_{pm}	Permanent magnet height [m]
h_{tt}	Height of the tooth tip [m]
I	Geometry factor for pitting resistance [-]
I_{ave}	Average current [A]
I_{nom}	Nominal current [A]
I_{rms}	RMS current [A]
J_{rms}	RMS current density [A/m^2]
K	Contact load factor [Pa]
k_0	Cost constant proportional to the ERS power [k€/MW]
K_1	Material dependent constant [1/Pa]
k_1	Cost constant proportional to road length [k€/km]
K_2	Material dependent constant [1/Pa]
k_2	Cost constant proportional to ERS hardware length [k€/km]
k_a	Relationship between semiconductor area and nominal current [mm^2/A]
K_b	Rim factor [-]
K_f	Waveform coefficient [-]
k_i	Interest rate [-]
K_m	Load distribution factor [-]
K_o	Overloading factor [-]

K_r	Reliability factor [-]
K_s	Size factor [-]
K_t	Temperature factor [-]
K_v	Dynamic factor [-]
k_v	Compensation factor for blocking voltage [-]
K_w	Winding fill factor [-]
k_{as}	Assembly cost factor [-]
k_A	Scaling factor for axial length of the EM [-]
k_{batt}	Usable fraction of the installed battery capacity [-]
k_{eddy}	Eddy current loss factor [$\mathrm{Wm^3/(HzT)^2}$]
k_{ERS}	Fraction of the road length equipped ERS hardware [-]
k_{ex}	Excess or anomalous loss factor [$\mathrm{Wm^3/(HzT)^{1.5}}$]
k_{hyst}	Hysteresis loss factor [$\mathrm{Wm^3/(HzT^2)}$]
k_{iron}	Factor that scales the initial width of the stator tooth and yoke [-]
k_{nt}	Scaling factor for the number of turns of the EM [-]
k_{ov}	Scaling factor for overloading of the EM [-]
k_{side}	Ratio between the side of the chip and the side of the power module stack [-]
L	Inductance [H]
l	Length [m]
l_{ap}	Air-pocket's length [m]
L_{ERS}	Length of the electrified road [km]
l_{gap}	Airgap length of the EM [m]
m	Modulation index [-] or gear's module [mm]
m_g	Gear ratio [-]
m_{fd}	Gear's aspect ratio [-]

m_{ps}	Ratio between the planet and the sun diameters [-]
N	Transformation ratio [-]
N_p	Number of poles [-]
N_t	Number of turns [-]
N_{iter}	Number of iterations [-]
N_{lanes}	Number of electrified lanes [-]
N_{tp}	Number of turns in the primary winding [-]
N_{ts}	Number of turns in the secondary winding [-]
P_{cond}	Conduction losses [W]
P_{cu}	Copper losses [W]
P_{fe}	Iron losses [W]
P_{sw}	Switching losses [W]
pf	Power factor [-]
q	Number of slots per pole and phase [-]
R_1	Radius of the 1'st cylinder [m]
R_2	Radius of the 2'nd cylinder [m]
R_c	Learning ratio [-]
$R_{ce/f}$	Collector-emitter or forward resistance [Ω]
$r_{ce/f}$	Inverse of the slope of the normalized current vs on-state voltage curve [ΩA]
r_{pm}	Permanent magnet radial position [m]
r_{ri}	Rotor inner radius [m]
r_{ro}	Rotor outer radius [m]
r_{si}	Inner stator radius [m]
r_{slot}	Radius of the slot corner [m]
r_{so}	Outer stator radius [m]

R_s	Stator resistance [Ω]
$R_{th,js}$	Thermal resistance junction to ambient [°C/W]
s_c	Contact stress [Pa]
S_f	Safety factor [-]
S_h	Safety factor for pitting [-]
s_t	Bending Stress [Pa]
T	Torque [Nm] or temperature [°C] depending on the context
t	Thickness of the cantilever beam or gear's tooth [m]
t_a	Amortization time [years]
T_a	Ambient temperature [°C]
T_j	Junction temperature [°C]
TC_r	Temperature coefficient for the $r_{ce/f}$ of the semiconductor [ΩA/°C]
TC_V	Temperature coefficient for semiconductor on-state voltage [V/°C]
TC_{sw}	Temperature coefficient for the switching losses of the semiconductor [1/°C]
V	Voltage [V]
v	Poisson's ratio [-]
$v(t)$	Voltage as function of time [V]
$v_{ave,x}$	Average speed of vehicle x [km/h]
$V_{ce/f}$	Collector-emitter or forward voltage [V]
V_{tooth}	Volume of the stator tooth [m^3]
V_{yoke}	Volume of the stator yoke [m^3]
W	Applied force [N]
W_c	Core width at airgap [m]
W_t	Tangential force [N]
W_{yk}	Width of the stator yoke [m]

x	Distance between the root of the tooth and the intersection of the line perpendicular to the line tangent to the root tooth [m]
Y	Lewis' form factor [-]
Y_j	Geometry factor for bending strength [-]
Y_n	Stress cycle factor [-]
Z_n	Stress cycle factor [-]
z_g	Number of teeth in the gear [-]
z_p	Number of teeth in the pinion [-]
AADT	Annual average daily traffic
AGMA	American gear manufacturing association
BEV	Battery electric vehicle
CAD	Computer aided design
CCS	Combined charging system
CPSR	Constant power speed range
ECE	External combustion engine
EM	Electrical machine
EREV	Extended range electric vehicle
ERS	Electric road systems
EV	Electric vehicle
FCEV	Fuel cell electric vehicle
FEM	Finite element method
FSCW	Fractional slot concentrated winding
GHG	Greenhouse gasses
HEV	Hybrid electric vehicle
ICE	Internal combustion engine

IGBT	Insulated-gate bipolar transistor
IPMSM	Interior permanent magnet synchronous machines
IPT	Inductive power transfer
ISG	Integrated starter-generator
LDV	Light duty vehicle
MMF	Magneto-motive force [A]
MSE	Modified Steinmetz equation
MT	Mechanical transmission
MTPA	Maximum torque per ampere
OBC	On-board charger
OEM	Original equipment manufacturer
PCB	Printed circuit board
PEC	Power electronics converter
PHEV	Plug-in hybrid electric vehicle
PSO	Particle swarm optimization
RCD	Residual current device
SOC	State of charge
SPMSM	Surface mounted permanent magnet synchronous machine
SV-PWM	Space vector pulse width modulation
THD	Total harmonic distortion
TIM	Thermal interface material

Chapter 1

Introduction

1.1 Background

During the early ages of the automotive industry, several technologies were available to replace horses as the main means of propulsion for carriages. By 1900 the most promising technologies were: internal combustion engines (ICEs), external combustion engines (ECEs) in the form of steam engines, and electric motors [1]. All of these technologies had advantages and drawbacks that ultimately would decide their fate. Early ICE vehicles were hard to operate, noisy, dirty and needed to be manually cranked, but offered a long range while using a relatively cheap and widely available fuel. On the other hand, long starting times, limited range due to the need of carrying water, and the occasional risk of explosions hindered the adoption of steam engines in personal vehicles despite having fewer moving parts than ICEs, their quiet operation and fast acceleration. Similarly, electric vehicles (EVs) offered a clean and quiet operation but suffered from short range, higher cost, insufficient access to electricity in rural areas and excessive weight, which made them hard to drive in unpaved roads.

It was not until the beginning of the series production of ICE vehicles, the invention of the electric starter and the increase in the availability of gasoline and lubricants that the ICE started to take over the automotive market [2]. Although, their dominance continues in today's market, in recent years traction electric motors have made a comeback into the automotive industry, mainly in the form of hybrids (HEVs), plug-in hybrids (PHEVs), fuel cell (FCEVs) and battery electric vehicles (BEVs). This is shown by the fact that between 2010 and 2016 the market share of these vehicle types (excluding HEVs) increased from 0.01% to 1.10% and their number rose from 16 thousand to 2 million in the same period of time [3]. Moreover, several international organizations and corporations such as the

International Energy Agency (IEA), Bloomberg and British Petroleum (BP) project that both their market share and total number of electrified vehicles will increase significantly in the upcoming $20 - 30$ years [3–6].

The comeback of the electric traction motor has been motivated by several factors. The first and maybe the most influential is the global increase in environmental awareness and the firm decision from most governments to take action in order to limit the effects of climate change, as clearly shown by the fact that 197 parties have signed the Paris Agreement and 170 have ratified it [7]. As part of the aforementioned agreement, each signing party has submitted its own ambitious goals for reduction of greenhouse gas (GHG) emissions; for example, United States[1] has the goal of reducing their emissions of GHG between $26 - 28\%$ by 2025 compared to 2005 while China has aimed to obtain 20% of its energy from low-carbon sources and to reach a peak in their CO_2 emissions by 2030. It is worth noting that these two countries account for about 35% of the global CO_2 emissions [8].

In order to achieve these targets, it is essential to reduce the emissions produced by the transport sector which accounts for about 25% of the CO_2 emissions globally, of which $3/4$ can be attributed to road transport in particular [9]. For this reason, governments around the globe have focused efforts on tightening emission standards for road vehicles and on providing incentives to cleaner alternatives to the ICE. In this context, automotive electrification is seen as one of the most promising solutions to reduce the emissions derived from road transport, specially when coupled with a decarbonization of the electricity generation. In general, electrified vehicles produce significantly less tailpipe emissions than their conventional counterparts, and plug-in vehicles (PHEVs and BEVs) in particular do not produce any tailpipe emission while covering distances within their battery range. However, for plug-in vehicles, it is important to consider the emissions corresponding to the generation of the electricity used, as this has the most significant impact on the overall emissions associated to these vehicle types [10].

Other aspects that have motivated the comeback of the electric traction motor into the automotive market are the volatility in the price of fossil fuels and concerns over their future supply. Transport of goods and people is essential to keep the society and the economy working and 29% of the energy consumed worldwide is destined to this task, with fossil fuels being the dominant energy source in the transport sector, accounting for 96% of the total energy used [11]. Nonetheless, as fossil fuels are a local resource, most countries rely on imports in order to fulfill their energy needs. Moreover, a reduced number of players have a very significant influence in the international market. The top 10 net exporters and importers account for about 75% of the crude oil market [11]. For this reason, political, economical or social changes in the major exporter/importer countries can derive into significant swings in the prices of these fuels. Additionally, the future supply of fossil fuels

---

[1] In 2017 the U.S. government decided to withdraw from the Paris Agreement. However, this decision will not be effective until 2020.

cannot be warranted indefinitely, since they are non-renewable resources. In this context, automotive electrification allows not only to lower the dependency of road transport from fossil fuels by reducing the fuel consumption of the vehicles, but it can also enable a transition to replace fossil fuels by electricity, which can be produced locally from a wide range of renewable sources such as hydro, solar, wind, tidal and geothermal.

All the aforementioned factors have pushed for an increase in research and technological innovation in the field of automotive electrification. Efforts have been focused on reducing the cost and size while increasing the efficiency and performance of electric powertrains and battery packs. The latter component has received special attention as, in most cases, it constitutes the major cost and weight driver in electric and hybrid vehicles. In this context, between 2012 and 2017 the volumetric and gravimetric energy density values have increased from 220 to 290 Wh/l and 120 to 160 Wh/kg respectively [3,12], while their cost has fallen from 500 $/kWh in 2008 to around 300 $/kWh in 2014 [13]. More recent estimates yield an even lower cost of battery packs, in the range of 227-190 $/kWh [3,14,15]. On the other hand, the performance and cost of power electronics converters (PECs) and electrical machines (EMs) have also improved significantly in the latest years. In particular the cost of the electric drive has dropped from 30 $/kW in 2012 to 15 $/kW in 2014, according to the U.S. Department of Energy (DoE) and is targeted to reach 8 $/kW by 2022 [16,17]. Additionally, the power density is targeted to increase form 1.1 to 1.4 kW/kg and from 2.6 to 4 kW/l between 2012 and 2022 [17].

Despite all these, it is clear that additional work is needed in order to ensure a significant penetration of electric and hybrid vehicles in the automotive market. In this regard, the cost of the vehicles needs to be further reduced in order to make them competitive with their conventional counterpart without the need for subsides or incentives. A fraction of the required cost reduction can be expected to come from technological improvements at the component level, economies of scale and the emergence of new technologies and materials. However, further cost reductions can be achieved by optimizing the system as a whole instead of optimizing the different components separately, which imposes artificial constraints in the design process. Furthermore, system integration and the addition of extra functionalities (e.g. charging or energy transfer between the traction and the service battery) in the powertrain have the potential of reducing the overall cost of the vehicle. Moreover, if the scope of the system is expanded past the vehicle itself, the optimization of the type and placement of the charging infrastructure required by plug-in vehicles presents a big opportunity to reduce the overall cost of electrification.

1.2 Scope and Objectives

This thesis addresses the issue of developing an environmentally sustainable transport system based on battery electric vehicles from a holistic perspective. In order to do so, the performance and cost drivers of the main components of an electric powertrain are identified and modeled. Among the components included in this work are the power electronics converters (PECs), the electrical machines (EMs) and the mechanical transmissions (MTs). The battery pack however, is not considered within the scope of this work. The aforementioned models serve as the foundation for a comprehensive powertrain optimization. Finally, This information is used to assess the societal cost of electrifying nationwide automotive fleets under different scenarios.

The main objectives of this thesis are:

- To optimize the design of electric powertrains taking into consideration efficiency, size, cost and performance.
- To quantify the cost impact of different electrification scenarios for a nationwide fleet.

1.3 Contributions

The main contributions of this work are:

- Compilation of knowledge regarding the factors that affect the cost, size and performance of the main components in an electric powertrain. This knowledge is then translated into computationally efficient models to be used in the optimization of an electric powertrain.
- Build a bridge between two disciplines, electrical and manufacturing engineering, thus fostering a better understanding on how design decisions affect the required manufacturing processes and vice-versa.
- Development of an optimization tool that allows to evaluate the impact of powertrain layout, machine topology, geometry and winding arrangement in the overall cost, efficiency and size of the powertrain. This tool is aimed for use during the predesign stage, where a large number of powertrain combinations need to be evaluated and considered in order to find a design that is worth to optimize further.

- Detailed assessment of the consequences and impact of different design decisions, based on the interactions and trade-offs between the different components in an electric powertrain.
- Evaluation of the societal cost of electrifying a nationwide fleet, specifically applied to Sweden and Denmark, in several scenarios considering different charging infrastructure alternatives. This allows to identify the main cost drivers for the fleet electrification and to quantify the cost effectiveness of different charging solutions.
- Development of a metric to determine which roads are most beneficial to electrify from a societal perspective, i.e. provide the highest ratio between benefit and electrification cost for their expected traffic volumes.

1.4 List of publications

I **From Chip to Converter: A Complete Cost Model for Power Electronics Converters**

G. Domingues-Olavarría, P. Fyhr, A. Reinap, M. Andersson and M. Alaküla
IEEE Transactions on Power Electronics, vol. 32, no. 11, pp. 8681-8692, Nov. 2017

II **Optimization of Electric Powertrains Based on Scalable Cost and Performance Models**

G. Domingues-Olavarría, F. J. Márquez-Fernández, P. Fyhr, A. Reinap, M. Andersson and M. Alaküla
IEEE Transactions on Industry Applications, pp. 1

III **Electric Roads: Analyzing the Societal Cost of Electrifying All Danish Road Transport**

G. Domingues-Olavarría, F. J. Márquez-Fernández , P. Fyhr, A. Reinap and M. Alaküla
World Electric Vehicle Journal, vol. 9, no. 1, Jun. 2018

IV **Scalable performance, efficiency and thermal models for electric drive components used in powertrain simulation and optimization**

G. Domingues, F. J. Márquez-Fernández, P. Fyhr, A. Reinap, M. Andersson and M. Alaküla

2017 IEEE Transportation Electrification Conference and Expo (ITEC), Jun. 2017

V **Performance and manufacturability tradeoffs of different electrical machine designs**

P. Fyhr, **G. Domingues**, A. Reinap, M. Andersson and M. Alaküla
2017 IEEE International Electric Machines and Drives Conference (IEMDC), May 2017

VI **Design and cost optimization of electrified automotive powertrain**

G. Domingues, A. Reinap and M. Alaküla
2016 International Conference on Electrical Systems for Aircraft, Railway, Ship Propulsion and Road Vehicles & International Transportation Electrification Conference (ESARS-ITEC), Nov. 2016

VII **Electric roads: The importance of sharing the infrastructure among different vehicle types**

F. J. Márquez-Fernández, **G. Domingues-Olavarría**, L. Lindgren and M. Alaküla
2017 IEEE Transportation Electrification Conference and Expo, Asia-Pacific (ITEC Asia-Pacific), Aug. 2017

VIII **Electric roads: Reducing the societal cost of automotive electrification**

P. Fyhr,**G. Domingues**, M. Andersson, F. J. Márquez-Fernández, H. Bängtsson and M. Alaküla
2017 IEEE Transportation Electrification Conference and Expo (ITEC), Jun. 2017

IX **STAR-C — A novel converter topology**

A. Holmström, **G. Domingues**, P. Fyhr and H. Bängtsson
Mediterranean Conference on Power Generation, Transmission, Distribution and Energy Conversion (MedPower 2016), Nov. 2016

X **Direct electromagnetic actuation on high ratio gears**

A. Reinap, M. Alaküla and **G. Domingues-Olavarría**
2016 XXII International Conference on Electrical Machines (ICEM), Sept. 2016

XI **Alternative EV powertrain topologies designed for operation in a conductive electric road system**

A. Karlsson, **G. Domingues-Olavarría** and M. Alaküla
2018 International Conference on Electrical Systems for Aircraft, Railway, Ship Propulsion and Road Vehicles & International Transportation Electrification Conference (ESARS-ITEC), Nov. 2018

XII **EV powertrain topologies for electric road applications**

A. Karlsson, **G. Domingues-Olavarría** and M. Alaküla
31st International Electric Vehicle Symposium and Exhibition, EVS 2018

Chapter 2

Electrified and electric vehicles

In this chapter an overview of different electrified and electric vehicle types, powertrain configurations and alternative charging solutions is presented. The goal is to provide the reader with a picture of the state of the art regarding different electrification technologies and to better understand how the work presented in the upcoming chapters fits in the context of automotive electrification.

2.1 Vehicle types

Road vehicles can be classified depending on the combination of energy storage(s) and propulsion system that they use. In this context, the energy storage can usually be chemical (hydrogen, fossil and alternative fuels), electro-chemical (batteries and supercapacitors), mechanical (flywheels) and even pneumatic or a combination of them [18]. The propulsion system for road vehicles commonly consists of an ICE and/or an EM.

An useful metric to help with the classification of road vehicles is the hybridization factor, sometimes referred to as hybridization level, which is defined as the ratio between the power of the EM(s) and the total installed power on the vehicle (EMs + ICE) [19]. This metric is tightly related to the extent of the benefits and drawbacks associated with electrification. The hybridization factor is a continuous scale, where at the bottom, with a hybridization level of zero, are the conventional fossil fuel vehicles, and at the top, with a hybridization level of one, are battery electric (BEVs) and Fuel cell vehicles (FCEVs). In between the extreme points of this scale are a variety of HEVs. In this section the most common vehicle types that use EMs for propulsion are presented.

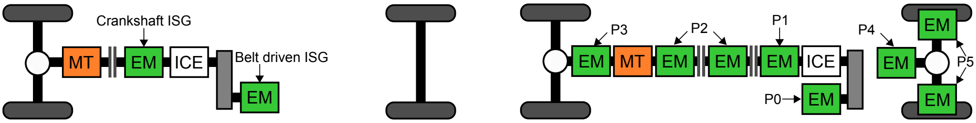

(a) Micro hybrid

(b) Mild hybrid

Figure 2.1: Powertrain configuration for micro and mild hybrids.

2.1.1 Hybrid electric vehicles

By definition, hybrid vehicles obtain the energy required for propulsion from at least two different sources, the primary one which is usually a fossil fuel and the secondary one which tends to be a battery. Although, other variants of hybrid vehicles exist, this work is focused on HEVs as they are the most common and commercially available kind. The basic idea behind a HEV is to combine the best aspects of both the ICE and the EM in order to reduce the fuel consumption and emissions without sacrificing the driving range while at the same time limiting the increase in the vehicle's cost and in some cases improving performance. Depending on their level of hybridization, HEVs can be classified in:

Micro hybrids: they represent the simplest and hence cheapest level of hybridization, and usually provide the lowest gains in terms of reduction in fuel consumption (in the range of $2-10\%$ [20]). In these vehicles, the starter and alternator are replaced by a single and more powerful EM, which usually operates at 12V (standard for most ICE passenger cars). This EM is often referred to as Integrated Starter-Generator (ISG), which can be belt driven or mounted directly on the crankshaft (see Fig. 2.1a). Either of these implementations allow to turn off the ICE while the vehicle is standing still as the EM can crank it in a relatively short period of time when needed. In this way, the fuel consumption can be reduced, specially during city driving where stops are frequent. Additionally, depending on the powertrain configuration, limited regenerative breaking is possible, as well as some electric propulsion in configurations with higher battery voltage. The term micro hybrid includes vehicles with hybridization factors below 10% [21].

Mild hybrids: they imply an increase in both battery voltage ($\geq 42V$) and hybridization factor (below 25% [21]) with respect to the micro hybrids. Consequently they provide higher reductions in fuel consumption (in the range of $10-20\%$ [20]) and the possibility to assist the ICE with electric propulsion, particularly at low speeds. As shown in Fig. 2.1b mild hybrids can be implemented in several ways, for example: the EM can be connected to the ICE via a belt ($P0$); mounted on the crankshaft ($P1$); placed on the gearbox input ($P2$) or output ($P3$); it can be mounted directly on the driving axle ($P4$); or inside the wheel hub ($P5$). These configurations affect the amount of energy that can be recovered from regenerative breaking, the system cost and whether or not it is possible to use the EM to crank the ICE.

Full hybrids: with a hybridization factor between $25-50\%$ [21] these vehicles are equipped with EMs and battery packs powerful enough to provide a significant amount of propulsion to the vehicle. This yields to even further reductions in fuel consumption (in the range of $20-50\%$ [20]) and the possibility of enhancing safety and performance significantly. Moreover, they may provide full electric driving within a limited range, and depending on the configuration, start and stop functions can also be included. It is worth noticing that as with all the previously mentioned hybrid vehicles, the total energy used for propulsion ultimately comes from fossil fuels and hybridization only allows to increase the efficiency on which that energy is being converted.

Plug-in hybrids: are basically full hybrid vehicles with the possibility of recharging the on-board battery using an external source (e.g. the electricity grid). They provide the same hybridization benefits as full hybrids with the added advantage of usually having a longer all-electric range as they tend to be equipped with battery packs of higher capacity. Their hybridization factor is usually above 50% [21].

Extended range electric vehicles: with respect to plug-in hybrids (PHEVs), they provide both an increase in the all electric range (usually by means of battery packs of higher capacity) and also a decrease in the required size of the ICE. Extended range electric vehicles (EREVs) drive most of the time in full electric mode and the function of the ICE is to increase the driving range rather than to provide propulsion.

Moreover, depending on the ways in which the energy can flow between the different energy storages and the wheels, the HEV architectures can be classified in:

- *Parallel hybrid*: this architecture might be the simplest way of electrifying a conventional vehicle and it can be implemented in a variety of ways. The basic idea is to add an EM to the conventional powertrain in a position where it can provide some level of propulsion to the wheels. In this architecture both the ICE and the EM can propel the vehicle separately or simultaneously and do so through the same axle (Fig. 2.2a) or different ones (Fig. 2.2b). As the required number of components added to the powertrain is rather limited, parallel hybridization tends to be a cost effective solution and by far the dominant architecture at low hybridization levels (micro and mild hybrids). Moreover, it makes it possible to downsize the ICE as the EM can assist with boost of power when needed.

- *Series hybrid*: in this architecture the ICE does not have any way of transmitting mechanical energy directly to the wheels. Instead, the ICE drives a generator (EM) that charges the battery pack and a different EM (or several) is in charge of propelling the vehicle. An example of this architecture is presented in Fig. 2.2c. As the ICE is not coupled to the wheels, it can operate at the highest efficiency point for the required power. Additionally, depending on the size of the energy storage it is possible

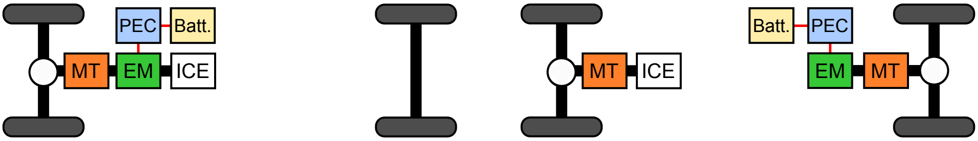

(a) Parallel hybrid

(b) Through the road parallel hybrid

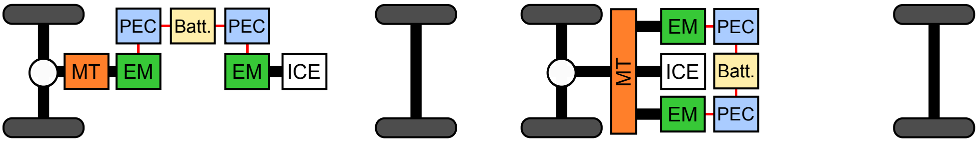

(c) Series hybrid

(d) Complex hybrid

Figure 2.2: Powertrain configuration for parallel, series and complex hybrids.

to reduce the rated power of the ICE. For example, for a sufficiently large energy storage the ICE can be sized to the average power needed in a given drive cycle. On the other hand, for a small energy storage, the ICE needs to be sized to the required peak traction power. The sweet spot is likely to be somewhere in between these two extreme cases, and therefore the correct sizing of the ICE and energy storage is an interesting optimization problem. The main drawback of this configuration is that a high number of energy conversions are performed to transform chemical into mechanical energy. Moreover, in series hybrids not all the power installed is available for propulsion, which results in somewhat poorer utilization of the equipment and, in most cases, a more expensive solution than a parallel hybrid vehicle. This is the dominant configuration for extended range electric vehicles (EREVs).

- *Complex hybrid*: in this architecture two EMs and an ICE are used together with a planetary gear transmission in order to provide all the advantages of series and parallel hybrids (see Fig. 2.2d). One of the main benefits of this configuration is the extended flexibility: by adjusting the load of the EMs and the speed of one of them, it is possible to operate the ICE in high efficiency regions most of the time. However, this architecture requires an elevated number of components and it is more complex to implement and control than the previously presented ones, which usually results in a higher cost as well.

2.1.2 Battery electric vehicle

If a vehicle uses a battery pack as its only means of on-board energy storage and an EM(s) as its only means of propulsion, it is by definition a BEV. Similarly to PHEVs, the battery pack in BEVs needs to be regularly recharged from an external source (e.g. the electricity grid). However, when compared with PHEVs, BEVs generally offer a longer all-electric range and simpler powertrains, both in terms of hardware and control. On the other hand, they tend to have a higher initial cost, offer an overall shorter driving range, require longer recharging times and are more sensitive to the lack of charging infrastructure [22].

2.1.3 Fuel cell vehicles

In FCEVs chemical energy (usually stored in a high pressure hydrogen tank) is transformed by a fuel cell into electricity that can then be used directly to propel the wheels or be stored into a battery or a supercapacitor; which acts as an energy buffer and helps providing bursts of power when needed. Thus, if the strict definition of a hybrid vehicle is used, a FCEV would need to be considered a hybrid. However, unlike the HEVs previously presented, in FCEVs the energy from both storages (chemical and electro-chemical) is transformed into mechanical energy by an EM. This vehicle type offers no tailpipe emissions, long driving ranges, quick refueling and it does not require any behavioral changes on the user side with respect to conventional vehicles. However, it suffers from a high initial cost and a lack of refueling infrastructure. Moreover, FCEVs have a lower grid to wheels efficiency than BEVs as the production of hydrogen and its posterior transformation back into electricity are low efficiency processes [23].

2.2 Powertrain configurations

The powertrains in BEV, FCEV and some HEV architectures, such as series and through the road parallel hybrids, can be arranged in a variety of ways, as electric powertrains offer the vehicle designers a higher level of flexibility compared to conventional ICE ones. In this section, the most important distinctions between different powertrain configurations are highlighted. It is worth pointing out that although all diagrams in Fig. 2.3 assume the use of batteries, the same powertrain configurations could be implemented with other forms of energy storage.

In an electric powertrain the propulsion can be concentrated in a single axle (as shown in the first column in Fig. 2.3) or distributed through several (see second column in Fig. 2.3) without the need for a mechanical link between them. Having propulsion in different axles increases traction, safety and improves the handling of the vehicle, features that can be attractive both for passenger and heavy vehicles. Additionally, having several propelling axles has the potential to increase reliability and enable limb-home functions, allowing the vehicle to keep driving (at a reduced performance) after a component has failed. On the other hand, a propulsion system concentrated in a single axle, in general presents a smaller foot print, a lower cost, and requires a simpler control algorithms, making it a

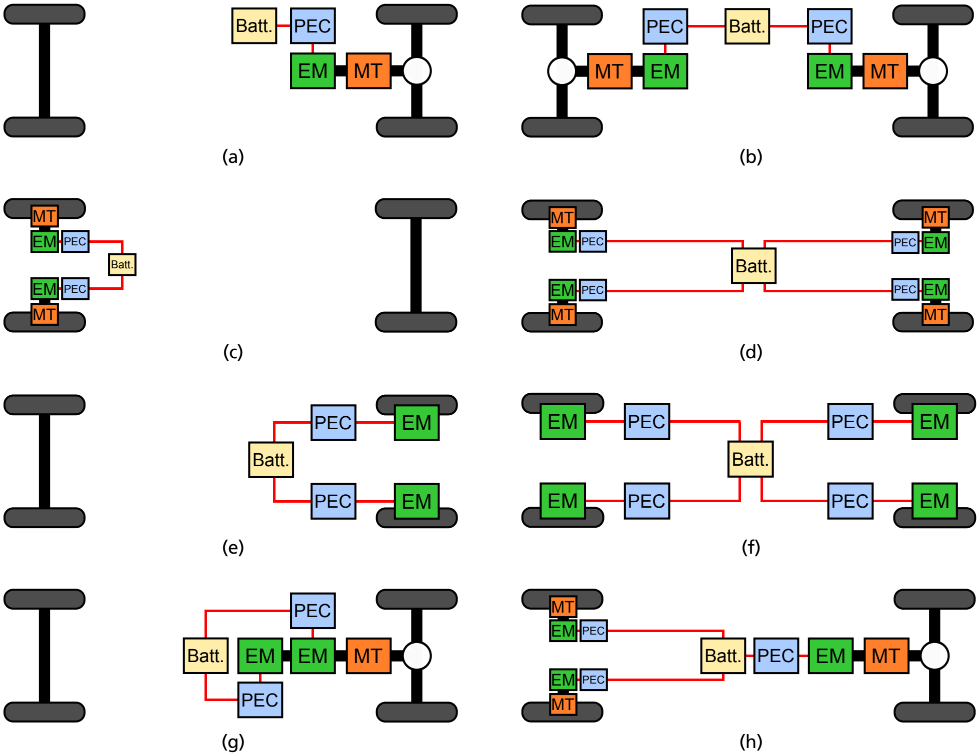

Figure 2.3: Alternative powertrain configurations.

strong candidate for lower cost vehicles.

Another consideration is the number of EMs used for traction, the powertrain can consist of a single EM per driven axle (see Fig. 2.3a) or an EM per driven wheel (refer to Fig. 2.3c-f)). In the first case the differential action is achieved by means of a mechanical differential (in the same way as it is done in conventional vehicles); in the second case the differential action is achieved by independent control of the different EMs attached to the wheels, something sometimes referred to as electrical differential. Using a single EM per driven axle provides a more robust and simpler system, with less failure points and usually a lower cost. However, having an EM propelling each driven wheel increases the flexibility of installation (as differential and prop shafts can be spared) and allows for additional features such as torque vectoring and more accurate traction control. An alternative to the two aforementioned configurations is the use of several EMs mounted on the same axle and coupled to a differential (as shown in Fig. 2.3g). This configuration does not provide torque vectoring but can allow the implementation of limp-home functions, expansion of the high efficiency regions by the use of different EMs and/or gear ratios and increase commonality in the components used in different vehicle models from the same original equipment manufacturer (OEM).

Moreover, as electric powertrains are significantly lighter than their conventional counterpart, there is the possibility of having either part or all of it in a fixed position relative to the wheels. A powertrain attached to the chassis is sprung with respect to the wheels. This reduces the vibrations but limits the flexibility of installation as cardan joints and prop shafts are needed in order to transfer power to the wheels. On the other hand, an unsprung powertrain offers a higher level of flexibility of installation and smaller footprints but its components are exposed to a harsher environment and need to withstand higher levels of vibrations. Additionally, increases in the unsprung mass tend to decrease the overall comfort of the vehicle. Powertrains based on wheel motors (as shown in Fig. 2.3e,f) are the most common example of a totally or partially unsprung powertrain, but other configurations are also possible.

Finally, if several axles are being propelled, it is possible to combine alternative configurations or components in the different axles (an example is shown in Fig. 2.3h), potentially decreasing the energy consumption by increasing the high efficiency operating regions of the powertrain. This alternative is particularly interesting in commercial vehicles as they have higher utilization than passenger vehicles and the energy cost represents a more significant share over their total cost of ownership [22].

2.3 Charging

Plug-in vehicles (BEVs, PHEVs and EREVs) in general have the need to recharge their battery packs periodically. This can be done in a variety of ways, which ultimately have a direct effect on both, the on-board and off-board components required.

2.3.1 Static charging

The most common way of charging a plug-in vehicle is to do it while it is standing still through a conductive connection. In this context, the standards IEC 61851 [24] and SAE J1772 [25] define four different charging modes for Europe and United States of America respectively. It is worth highlighting that the charging modes defined in IEC 61851 are extremely similar to the charging levels defined in SAE J1772 with the main difference being related to the grid connection available in Europe and United States. In this section a quick overview of the different charging modes described in IEC 61851 is presented, as it is the most relevant standard in Europe.

Mode 1: it is the simplest charging mode as it takes advantage of widely available infrastructure and basically implies the use of standard plugs. In mode 1 the maximum current is limited to 16 A and the connection can be single phase (230 V) or three phase (400 V) which allows for charging powers up to 3.7 kW and 11 kW respectively. All the required components are placed on-board the vehicle and no communication to any external equipment is needed. However, this charging mode relies on the supply side being equipped with a residual current device (RCD).

Mode 2: opens the possibility to double the transferred power from Mode 1. This is done by allowing a maximum current of 32 A instead of the 16 A allowed by the previous mode, increasing in this way the charging power to 7.4 kW or 22 kW for a single or a three phase connection respectively. Unlike mode 1, mode 2 requires a control device to be placed between the grid and the vehicle. This device is usually mounted on the charging cable or in close proximity to the power outlet. The main functions of this device are to stop the charging operation when a fault is detected and to communicate with the vehicle to limit the maximum charging power.

Mode 3: unlike modes 1 and 2 requires the use of dedicated charging stations, that are permanently connected to the grid. The charging station provides all the control and safety features described for mode 2. The maximum charging power is also increased by the use of a 63 A connection, allowing to transfer 16 kW or 44 kW for a single or a three phase connection respectively.

Mode 4: introduces DC charging. Thus all the charging equipment is placed off-board the vehicle unlike all the charging modes previously presented. It allows for a maximum charging rate of 240 kW, with an output of up to 600 V DC and 400 A. Currently there are two dominant standards for DC charging, CHAdeMO and the Combined Charging System (CCS). However, the latter offers a higher level of flexibility as it allows for both AC and DC charging through the same connector. For this reason, it could be expected that in the near future CCS will become the dominant standard in Europe and United States. Additionally, Tesla uses its own standard in their super charger stations [26].

So far a description of the different static conductive charging modes, both for AC and DC, have been presented. However, static charging of plug-in vehicles can also be performed wirelessly. There are several alternative technologies that can be used to this end [27], being inductive power transfer (IPT) the most common one. In this charging method the vehicle is equipped with a receiving coil and some on-board electronics while a transmitting coil is placed either on or under the surface of the road. A magnetic coupling is established between the receiving and transmitting coil allowing to transfer energy between the charging station and the vehicle. Wireless charging offers several advantages, for example, it is easy to operate and does not require the user to handle any electrical equipment or cables, it provides galvanic insulation thus increasing safety and the required time to initiate and terminate the charging is significantly reduced compared to conductive connections. However, drawbacks include higher cost, lower power density, bulkier on-board equipment and lower system efficiency [28].

2.3.2 Dynamic charging

In recent years, the idea of charging plug-in vehicles while they are moving has gained momentum and a variety of different technologies focused on enabling dynamic charging have emerged. These technologies are often referred to as Electric Road Systems (ERS) and in general they all provide the same basic benefits, such as allowing vehicles to have smaller battery packs without sacrificing their driving range, avoiding long charging stops and possibly reducing the need for fast charging infrastructure. Without focusing on particular solutions, ERS can be classified depending on their physical location with respect to the road and the form of energy transfer. Following these criteria, five different groups can be distinguished in the literature: overhead conductive, road bound conductive, road bound inductive, road bound capacitive and road side conductive.

Overhead conductive: Overhead conductive electric roads consist of two supply lines placed above the road at a height of around five meters. The vehicles need to be equipped with a connection device, usually known as pantograph due to the existing similarities with railway applications, in order to establish contact with the supply lines. Additionally, this connection device must compensate both the lateral and vertical movements of the vehicle respect to the supply lines. This technology is only suitable to supply vehicles that are relatively tall (trucks and buses) as the large clearance between the power supply lines and the road surface makes mounting a suitable connection device in smaller vehicles impractical. From a safety perspective, overhead conductive ERS are advantageous since the supply lines are hard to be accidentally reached by humans or animals, thus long stretches can be energized (> 1km) at once.

This technology is currently being tested in public roads in Sandviken, Sweden [29], where contact lines supplying 650-750 Vdc are placed in a two kilometer stretch of highway and plug-in Hybrid trucks equipped with pantographs connect to them in order to drive in full electric mode.

Despite being a relatively mature technology in other applications such as trolley buses and, to a certain extent, trams and railways (although in these the current return path is through the steel wheels), higher driving speeds and potentially higher utilization of the infrastructure introduce new challenges that need to be addressed.

Road bound conductive: The term road bound ERS refers to a group of dynamic charging solutions that are characterized by presenting power conductors placed in close proximity to the surface of the road. An electrical connection between the ERS and the vehicle is established by means of a retractable current collecting device, hereinafter referred to as pick-up, placed placed underneath the vehicle, that makes contact with the power conductors. From an electric safety perspective, this family of solutions tends to present significantly shorter energized segments in comparison with overhead ERS, as the conductors are placed in easy reach of humans and animals. The design of both the pick-up and the power conductors on the road depends heavily on the specific road bound conductive ERS solution.

For example, in [30] the power conductors are placed inside grooves made to the surface of the road, similar to a slot car. In this system, segments of around 50 m are energized when the vehicle is on top of them. One advantage of this solution is that it allows the energy supply to be either AC (reducing the cost of infrastructure) or DC (reducing the cost on-board the vehicles).

On the other hand, an ERS solution is presented in [31] where two flat conductors are placed in the middle of the lane, parallel to the road. Segments of 22 m are energized in order to supply the vehicle with 750 Vdc. This solution comes inspired from previous experiences in trams and railways.

Yet another approach is shown in [32], where the conductors are placed a few centimeters above the surface of the road in a single track. Unlike previous concepts, the positive and negative terminals are not placed side by side. Instead, this solution places the terminals in-line with each other, alternating positive and negative segments with some insulation distance in between segments. In order to close the electrical circuit, any vehicle needs to be in contact with at least two segments (one positive and one negative). For this reason, the segment length needs to be significantly shorter than in the previous concepts (1 m), which can be perceived as an advantage in terms of safety as only the segments directly underneath the vehicle are electrified in a given point in time.

Road bound inductive: In an inductive ERS energy is transfered from the road to the vehicle without the need for a conductive connection. As for the case of static inductive charging, this energy transfer is achieved by means of two sets of coils, the primary (placed on the road) and the secondary (placed underneath the vehicle). Energy is transfered from the primary to the secondary coil by magnetic induction, in what could be described as a gapped transformer.

Despite the maturity of inductive energy transfer in consumer electronics and static charging of EV, new challenges come when this technology is used for dynamic charging. One of these challenges is the need for a good tolerance to lateral misalignments and vertical displacement, as keeping the coils at the same relative position respect to the road while the vehicle is moving is particularly difficult. Furthermore, the need for a high power density on the secondary coil, in order to minimize the added weight to the vehicle, and the need for an arrangement of coils that allows to supply vehicles of different sizes, and therefore required power levels, are other challenges that need to be addressed. Finally, in order to ensure the safety of the system, it is needed to contain and limit the magnitude of the leakage fields.

An example of an inductive ERS was demonstrated in 2009 by KAIST [33], as part of the OLEV project. Moreover, an economical analysis of this technology is presented in [34] showing that the cost savings due to the downsizing of the required battery pack for the same driving mission are greater than the cost of installing the dynamic charging infrastructure.

Road bound capacitive: Another approach to contact less energy transfer to a vehicle while in motion is through capacitive power transfer. In this case, a capacitive coupling is built between metal plates on the road and the vehicle. This coupling is used to transfer power from the road to the vehicle by means of high frequency voltages and currents.

The main advantage of this system is the simplicity and low cost of the electrodes as no coupling coils are needed. On the other hand, high frequency inverters and rectifiers are needed for this implementation which may lead to a higher system cost.

This technology has been shown in [35] where a capacitive ERS able to deliver 900 W to the battery is implemented and tested on a single seater vehicle in a 2.4 m stretch. This technology requires additional work to increase both the efficiency and power transfer capabilities in order to be applicable to more conventional vehicles.

Road side conductive: Conductive ERS are not limited to be placed above or below the vehicle. The Japanese OEM Honda has proposed to place the power conductors on the side of the road [36], which allows both passenger and heavy vehicles to take advantage of the infrastructure while keeping the road surface unchanged. This can potentially translate into lower maintenance cost for the road and lower installation cost for the ERS.

This system has been tested at transfer powers of up to 450 kW and driving speeds up to 200 km/h [37, 38]. However, further test in public roads are needed in order to ensure the reliability and safety of the system.

2.3.3 Challenges and opportunities

It is expected that the majority of the electric energy consumed by plug-in vehicles will be provided by overnight charging [39–41], as it is the most convenient and possibly cheapest way of charging for most users. However, access to night chargers is becoming an issue, specially in cities, where not all users have access to a private garage or a dedicated parking spot with power outlets [42]. Finding solutions for these users represents a challenge, and alternatives such as installing charging posts in street parking spots, retrofitting power outlets to existing electric infrastructure (e.g. street lamps), allowing home owners to place extension cords from their houses to their vehicles, etc. are proposed [43]. However, as these solu-

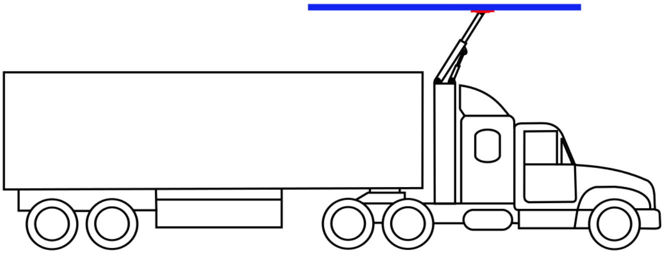

(a) Overhead conductive

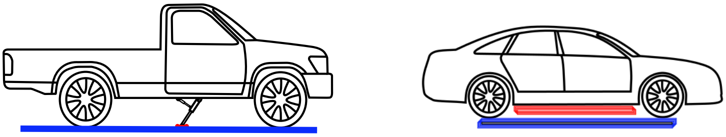

(b) Road bound conductive **(c)** Road bound inductive

(d) Road bound capacitive **(e)** Road side conductive

Figure 2.4: Different ERS technologies. The energy supply is shown in blue while the the pick-up is shown in red.

tions do not cover the needs of all users, destination-, public- and/or fast-charging could be the only viable alternatives in some cases. In this context, ensuring easy access to reliable charging infrastructure is essential to increase the market penetration of plug-in vehicles.

Moreover, in a scenario where only static charging is implemented at a significant scale, fast charging infrastructure becomes a necessity to reduce the range anxiety of the users and to enable long distance traveling. Nevertheless, the correct dimensioning, placement and roll-out of this infrastructure represents a challenge. An initial deployment with enough coverage is needed in order to increase the adoption of plug-in vehicles, but at the same time low infrastructure utilization can be expected during this initial phase [44], making fast charging infrastructure an unattractive investment from the economical viewpoint. Furthermore, the fast charging infrastructure should expand at a pace that keeps up with the demands from a growing plug-in vehicle market, and new business models combined with some government support may be required to create the right incentives for a private deployment and operation of fast charging infrastructure [22, 42].

Increasing the availability of charging infrastructure can have added benefits other than facilitating charging. Light duty vehicles in general spend most of their time parked and are only used a few hours a day, if charging infrastructure is widely available both at home and at frequent destinations (e.g. work places, shopping malls, etc.) a large portion of the vehicle fleet can be connected to the grid at any point in time, not necessarily for charging only but also to provide benefits both to the vehicle owner and the grid [45]. The range of services that vehicles can provide varies depending on the type of connection and the ways in which the energy can flow between the grid and the vehicle [46]. For example, with a unidirectional energy transfer, the vehicle charging can be scheduled to take advantage of periods of low energy prices, or to provide grid services such as peak shaving and load shaping to ease the integrations of renewable generation to the grid. However, these services are only available as long as the vehicle battery is bellow its maximum allowable state of charge (SOC). On the other hand, bidirectional energy transfer allows to implement some additional services, such as valley filling, active power regulation, harmonic filtering, etc [47]. Regardless of the type of services that the vehicle is delivering it is important to ensure that the vehicle's owner is being compensated for the additional cost and/or degradation of the on-board components and for keeping the vehicle plugged even when it does not requires charging. Additionally, it is important to guarantee that the vehicle has enough charge when the owner requires it, as vehicle usability should remain a priority [48].

In this context, on-board chargers (OBC) are essential to allow vehicles to take advantage of cheaper and more abundant charging infrastructure. However, they are expensive components, specially when rated for high power. An alternative that promises to reduce the overall cost of the vehicle while enabling high charging power, is to integrate parts of the OBC into the electric powertrain [49–51]. These solutions tend to reduce the component count at the expense of a more complex control and a generally lower efficiency when compared with dedicated OBC. Although there is clear evidence that parts of the automotive industry consider integrated OBC as a cost effective solution [52, 53] and that presently it is a hot topic for research in academia [54–56], a study comparing the cost effectiveness of an integrated OBC vs a dedicated one, accounting not only for the initial cost but also for the cost of lost energy, is missing in the literature to determine the true cost effectiveness of these solutions.

Another technology that has the potential to disrupt the automotive industry in general and charging of plug-in vehicles in particular is autonomous driving. This technology allows to increase the vehicles' utilization and possibly reduce the fleet size. An obvious impact of autonomous vehicles is that automatic connection (either conductive or inductive) to the charging infrastructure will not be any more a convenience for the user but rather a necessity for the vehicle. Additionally, autonomous vehicles providing transportation services such as car pooling/sharing, delivering goods, etc. are in direct competition with the use of vehicles to provide grid services, as the former one relies on the vehicle being available for driving as soon as possible (i.e. short charging times) and the latter benefits from having a large number of vehicles being parked and plugged to the the grid at any point in time. A study of the interaction between autonomous vehicles and the possibility of providing grid services can be quite interesting as literature on the topic is scarce.

Chapter 3

Component modeling

In order to optimize or analyze electromobility systems it is necessary to use models that can accurately describe the performance, size and cost of the components that comprise such systems. Moreover, it is important to find a balance between the accuracy of the models and their execution time in order for them to be a valuable tool in practical applications. In this context, this chapter describes in detail how power electronics converters (PECs), electrical machines (EMs) and mechanical transmissions (MTs) are modeled both in terms of performance and cost. The models presented in this chapter serve as the foundation for the work presented in Chapters 4 and 5.

3.1 Power electronics converters

An electrified vehicle has a variety of power electronics converters (PECs) that fulfill functions such as traction, charging and even energy transfer between the traction and the service battery. In this context, any accurate evaluation of a powertrain design or charging system requires a detailed understanding of the factors affecting the performance and driving the cost of a PEC. In this section, the methodology used to model the performance and cost of a complete PEC is presented. The material described next is an extension of the work previously published in [57].

In this work, a bottom-up approach is taken. The first step in this process is to define the basic characteristics of the converter under study. Knowing the converter's topology is essential since it provides information on the layout and required set of components. Although several topologies can achieve the same type of energy conversion and the PEC can be implemented as a single unit or in multiple modules, the advantages and drawbacks have to be pondered beforehand in order to select the most beneficial topology and configuration for the application. Alternatively, an external loop can be added to the design and cost estimation process to optimize the selection of the PEC's topology.

In a similar manner, the operating point(s) and modulation scheme have to be specified in advance, due to the fact that they play an essential role when determining the stresses on the different components. Additionally, information about the operating conditions and available cooling needs to be provided in order to ensure that the converter can operate effectively in the targeted environment and that the enclosure fulfills the demands of the application.

After all the input parameters are defined, the next step consists in determining which components need to be designed and which can be selected directly from a component database. The general approach is that all the signal and control components (i.e. microcontroller, voltage and current sensors, CAN transceiver, etc.) are selected from a component database while power electronic components (i.e. power modules, inductors, transformers, DC-link capacitors, snubbers, filters, etc.) are designed and optimized to work under the specified operating points and predefined conditions.

Once all the components are either selected or designed, the layout is established based on the size of the components and the topology of the converter. The size and number of layers of the control PCB is determined as a function of the components that must be mounted and the required connections to other components. At this point the sizes of all the components are available and their layout is known, so the process continues with an estimation of the housing and cold plate or heat sink dimensions.

The sizing methodology used for designing the major power electronics components is presented next.

3.1.1 Semiconductor devices

When selecting semiconductor devices for a PEC, the objective generally is to determine the minimum required size of all the semiconductor devices in the converter that ensures the desired performance under the specified operating conditions. In order to achieve this, a similar approach as the one presented in [58] is adopted in this work. This approach results particularly interesting since it does not restrict the selection of semiconductor devices to those readily available in the market; instead, given a semiconductor technology, this approach allows to optimize the size of each device according to the needs of the application. This approach is feasible in reality if the expected production volumes are large enough, otherwise the use of off the shelf components may result in a more cost effective solution.

The size of the semiconductor influences the electrical and thermal characteristics of the device. The selected sizing approach requires the development of a database of compon-

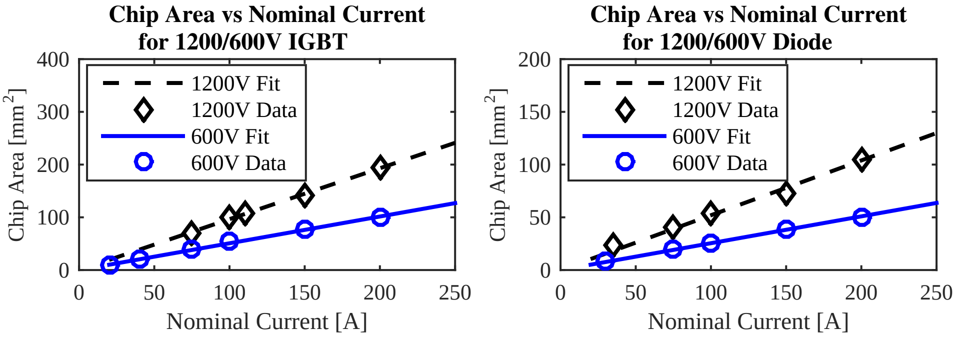

Figure 3.1: Area as function of nominal current for 600/1200V IGBTs and Diodes.

ents where both their electrical and thermal attributes are correlated with their chip area. Although most datasheets do not specify the area of the semiconductor; a relationship between the nominal current of the device and its chip area can be extracted from bare die datasheets. An example of this can be observed in Fig. 3.1 where the chip area is expressed as a function of the nominal current of the device for IGBTs and diodes rated for 600 V and 1200 V. The relationship between chip area and nominal current can be described using (3.1), where a different k_a is obtained for each semiconductor technology and rated voltage (see table 3.1).

$$A_{chip} = k_a I_{nom} \tag{3.1}$$

The next step consists in modeling the losses as a function of the operating conditions and chip area. In line with the standard procedure in the literature, only conduction and switching losses are considered when computing the total power losses in the semiconductor devices.

$$P_{cond\ T/D} = R_{ce/f} I_{rms}^2 + V_{ce_o/f_o} I_{ave} \tag{3.2}$$

Equation (3.2) shows how the conduction losses are computed. The rms and average current (I_{rms} and I_{ave}) are given by the operating point and modulation scheme. On the other hand, the on-state resistance (R_{ce} and R_f for IGBTs and diodes respectively) and the threshold voltage (V_{ce_o} for IGBTs and V_{f_o} for diodes) are properties that depend on the temperature, rated voltage of the device and, for the on-state resistance also its size.

The left column of Fig. 3.2 shows the current vs voltage curves for 600 V IGBTs and diodes. Each color represents devices with different nominal currents; continuous and dashed

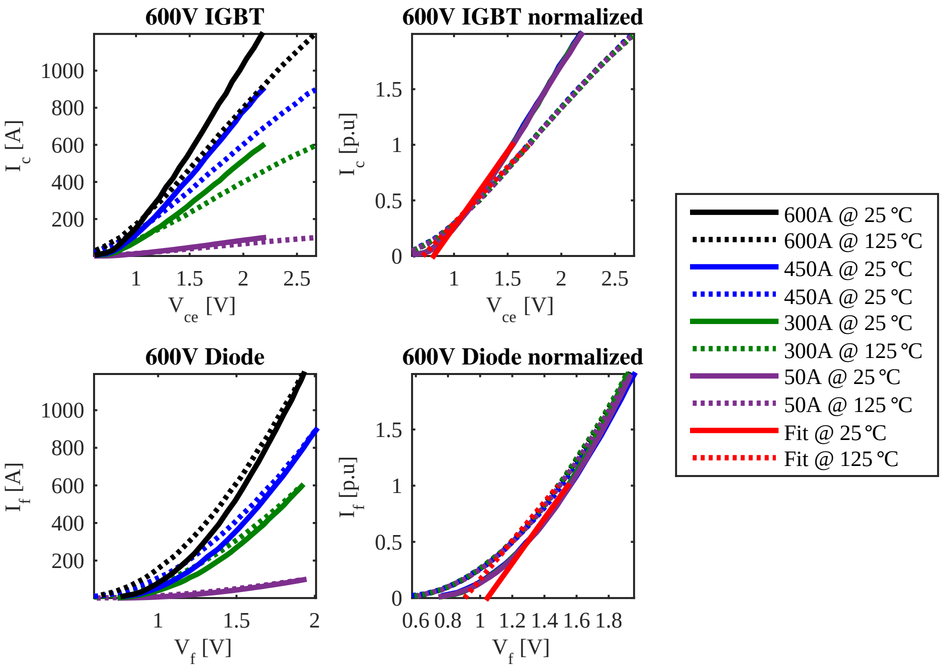

Figure 3.2: Current vs on-state voltage for 600 V IGBTs and diodes with different nominal currents.

lines are used to depict the curves at different temperatures (25°C and 125°C respectively). When these curves are normalized with respect to the nominal current of the devices (see right column of Fig. 3.2) it can be seen that for both temperatures the curves for all the devices lay on top of each other. Several remarks can be made from this figure. The first one is that the threshold voltage only depends on the rated voltage of the device and the operating temperature but not on its chip area; the second one is that the temperature influence on the threshold voltage and resistance of the device can be decoupled from its size and the final the final remark is that the resistance of the device is inversely proportional to its size at a given operating temperature. Although, the aforementioned remarks are to be expected when one takes a close look at the internal structure of the different semiconductor devices [59], the proposed approach aims to quantify the influence of both temperature and chip area on the on-state resistance and threshold voltage of the device using only information available in datasheets and without needing to know the exact internal structure of the semiconductor device. This allows to estimate the performance of devices that use the same semiconductor technology and rated voltage but have a different chip size and/or operate at a different temperature.

From the curves presented in Fig. 3.2 the threshold voltage at different temperatures can be obtained as the point where the approximated curve (shown in red on the right column of Fig. 3.2) crosses the x-axis. Moreover, as datasheets usually provide such curves for at least two temperatures, a compensation factor is calculated as presented in (3.3) and used to compute the threshold voltage at any temperature as shown in (3.4) [60]. On the other hand, it is possible to calculate the resistance of the device as shown in (3.5) where $r_{ce/f}$ is the inverse of the slope of the normalized current vs on-state voltage curve and TC_r is the temperature coefficient for $r_{ce/f}$ which can be determined as shown in (3.6). All the calculated values for 600 V and 1200 V IGBTs and Diodes are presented in Table 3.1.

$$TC_V = \frac{V_{ce_o/f_o@T_1} - V_{ce_o/f_o@T_2}}{T_1 - T_2} \tag{3.3}$$

$$V_{ce_o/f_o}(T_j) = V_{ce_o/f_o@T_1} + TC_V(T_j - T_1) \tag{3.4}$$

$$R_{ce/f}(T_j, A_{chip}) = \frac{k_a}{A_{chip}}\left(r_{ce/f@T_1} + TC_r(T_j - T_1)\right) \tag{3.5}$$

$$TC_r = \frac{r_{ce/f@T_1} - r_{ce/f@T_2}}{T_1 - T_2} \tag{3.6}$$

Table 3.1: Semiconductor devices parameters

	IGBT		Diodes	
V_{rated}	$600V$	$1200V$	$600V$	$1200V$
$k_a\ [mm^2/A]$	0.507	0.9651	0.2546	0.5197
$V_{on@25^\circ C}\ [V]$	0.8093	0.8816	1.0451	1.03
$V_{on@125^\circ C}\ [V]$	0.71	0.7905	0.9037	0.8504
$TC_V\ [V/^\circ C]$	-0.00099	-0.00091	-0.0014	-0.0018
$r_{on@25^\circ C}\ [\Omega A]$	0.7336	0.8196	0.5005	0.6255
$r_{on@125^\circ C}\ [\Omega A]$	0.9869	1.1999	0.5812	0.8154
$TC_r\ [\Omega A\,/^\circ C]$	0.0025	0.0038	0.000806	0.0019
$TC_{sw}\ [1/^\circ C]$	0.0025	–	0.006	–

Modeling the switching losses of semiconductor devices is a more challenging undertaking as they are affected not only by the current, blocking voltage, temperature and chip area of the device but also by the driver characteristics. Without the possibility of doing extensive lab testing to adjust all these dependencies, the selected approach implies correlating the switching energy losses provided in the datasheets of commercially available devices with their chip area and the switched current.

The switching losses are calculated as described in (3.7). The switching frequency (f_{sw}) is a parameter defined beforehand. T_j and V represent the operating temperature and blocking voltage while T_{ref} and V_{ref} are the reference values at which the energy losses are defined

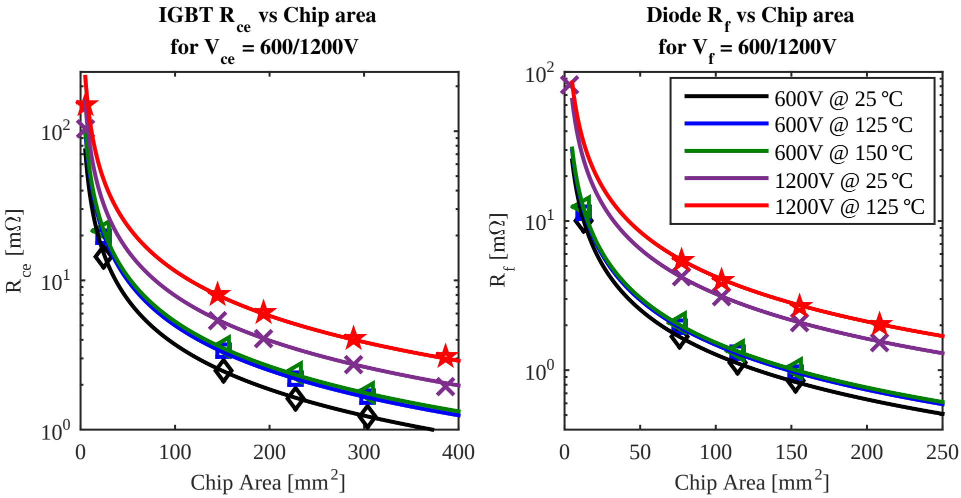

Figure 3.3: On-state resistance as function of die area for 600/1200 V IGBTs and Diodes at different operating temperatures. The markers represent the values taken directly from the datasheets while the lines are calculated using (3.5).

in the datasheets. TC_{sw} is the temperature coefficient for the switching losses, which can be calculated as shown in (3.8). The obtained values for TC_{sw} are presented in Table 3.1 for 600 V devices, however, the datasheets compiled for 1200 V devices only provide the switching energy losses for one temperature value, which makes it impossible to calculate TC_{sw}. For this reason, the temperature coefficient for the switching losses calculated for 600 V devices is also used for the 1200 V ones. k_v is a compensation factor to account for changes in the blocking voltage and its value is taken from [60]. Finally, the energy losses are represented by E_{sw}. This last parameter is described as a function of the current and chip area of the device as it can be seen in Fig. 3.4 where the losses for diodes and IGBTs rated for 600 and 1200 V are depicted.

$$P_{sw} = f_{sw} E_{sw}(A_{chip,I}) \left(\frac{V}{V_{ref}}\right)^{k_v} \left(1 + TC_{sw}(T_j - T_{ref})\right) \tag{3.7}$$

$$TC_{sw} = \frac{\frac{E_{sw}\,@T_1}{E_{sw}\,@T_{ref}} - 1}{T_1 - T_{ref}} \tag{3.8}$$

It is worth mentioning that as the presented energy losses are taken directly from datasheets they are measured under specific testing conditions and by use of a recommended value for the gate resistor. Terms to compensate for different operating temperature and voltages are included in Eq. (3.7). However,if a different gate resistor value is to be used, it is necessary to experimentally measure the losses in the devices and add them to the database creating a new surface on top or below the ones presented in Fig. 3.4. In this work, the size of the semiconductors devices in the converters is calculated assuming that the recommended gate resistor is selected.

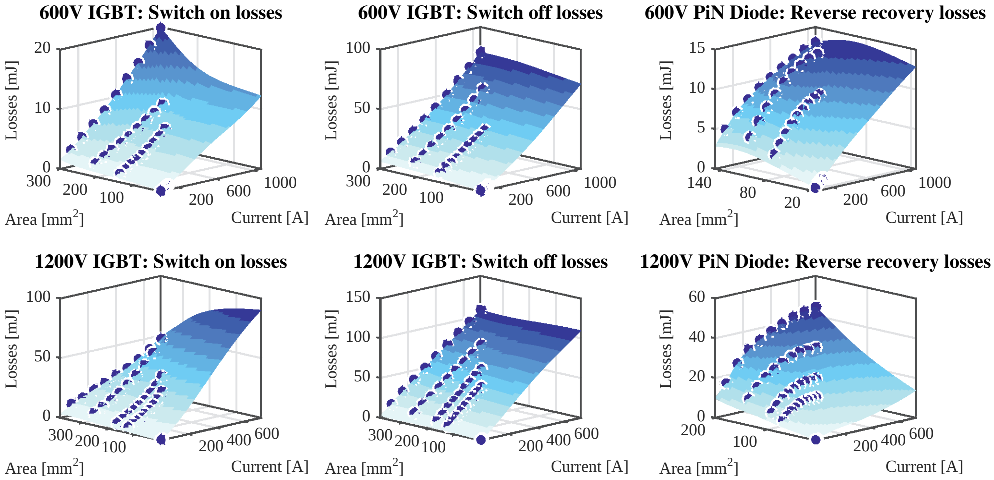

Figure 3.4: Switching energy losses for 600V and 1200V IGBT's and diodes as function of chip area and current. The blue dots are the losses extracted from the datasheets and the surfaces are the fitted losses.

Since this work focuses on electric powertrains for vehicles and charging infrastructure, the power levels of interest range from some tens of kW to a few hundred. In this range, the dominant enclosure for semiconductor devices is the power module. This type of packing provides a good thermal conductivity between the semiconductor device and the heatsink or cold plate, which enables higher power densities. Alternatively, discrete devices packed in through-hole enclosures can be used in conjunction with PCBs in low power applications in order to reduce costs. However, the advantages of this implementation are significantly reduced when several devices need to be connected in parallel [61]. For the exposed reasons, and to allow the model to be valid in a wide power range, the present work assumes power modules to be the package of choice for semiconductor devices.

With the package defined beforehand, the thermal resistance between the junction of the semiconductor and the heatsink can be determined as it mostly depends on the structure of the power module and the thermal interface material (TIM). The silicon itself only accounts for about 4% of the total thermal resistance [60]. Taking this into consideration, the thermal resistance between the junction and the heatsink of any semiconductor device can be modeled as a function of its area and the distance to surrounding chips as shown in Fig. 3.5a. The surface represents the values calculated from a 3D finite element model (presented in Fig. 3.5b); the blue dots are the values for thermal resistance calculated according to [58]. It can be seen that for a k_{side} of around 2.3 the results from the finite element model match quite well with those available in the literature, however, small discrepancies can be observed at high chip sizes. This can be due to differences in the power module structure used to generate both expressions and/or that the range of chip sizes explored in Fig 3.5a is outside the range of the data used to generate the expression shown in [58].

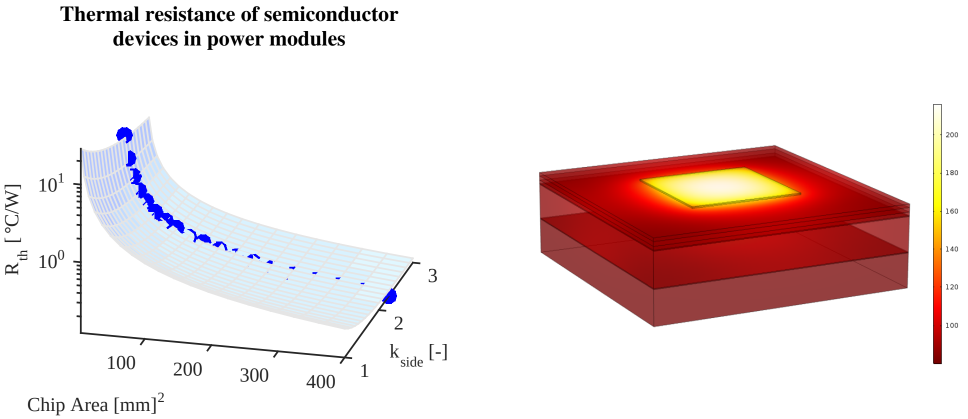

(a) Thermal Resistance

(b) 3D Finite Element model

Figure 3.5: (a) Thermal resistance as function of chip area and ratio between the side of the chip and the side of the power module stack. (b) 3D thermal model used.

$$T_j = T_a + R_{th,js} P_{loss} \tag{3.9}$$

Once the loss and thermal modeling of semiconductor devices is complete, an iterative procedure is carried out in order to determine the minimum size of the device required for a given application. The input data to the iterative procedure are the technology of semiconductor, currents, blocking voltage, switching frequency and heatsink temperature. As the first step of this process, a preliminary estimation of the area is carried out and the losses produced by a chip of that size are estimated. By use of those losses and the heatsink temperature, the junction temperature is calculated (3.9). If T_j is greater or lower than the predefined maximum value, the size of the chip is adjusted and the process is repeated until the junction temperature is around the desired level. At this point, the size of the semiconductor device is optimized for the application. This process can be observed in the semiconductor section of Fig. 3.9. This procedure is then repeated for each semiconductor in the converter. It is important to keep in mind that this sizing procedure is based on average temperature and losses, meaning that peak temperatures can exceed the maximum allowable junction temperature. Finally, it is worth noticing that the described loss estimation and sizing methodology for IGBTs and diodes are also applicable to other transistor and diode technologies or voltage ratings, as long as it is described how their chip area affects their thermal and electrical characteristics.

After the total area of all the semiconductor devices is estimated, it is possible to calculate the number and size of power modules required to accommodate all the devices. The ratio between the power module and semiconductor area is usually in the range of 4-10 and is tightly related to the k_{side} used to estimate the thermal resistance. Reducing this ratio increases the thermal coupling between chips (as shown in Fig. 3.5b) but reduces the size and/or number of power modules which effectively reduces the cost. Finding an optimal value for this ratio requires an in-depth thermal analysis which would be very time consuming. Therefore, in this work k_{side} is selected to be fixed at 2.3 based on experience and analysis of commercial modules. Once the size and number of power modules and semiconductor devices are calculated, it is possible to estimate the cost of the power module using the cost model presented in [62].

3.1.2 Magnetic components

The procedure to design inductors and transformers is well known and vastly explained in the literature [63–65]. As for the previous components, this work focuses on producing an estimation of the true size with material specifications and winding arrangement for the inductor or transformer rather than on providing a final, complete and detailed design.

In this context, the employed sizing procedure starts with collecting the required input data. Operating conditions and frequency, available cooling, current and voltage waveforms and transformation ratio or inductance are among the essential parameters required to determine the size and eventually the cost of the specific inductor/transformer.

The winding configuration is defined beforehand by the designer, who has to ponder the benefits and drawbacks of one configuration respect to the others in the application under consideration. For example, the main benefit of round wires is their lower cost compared to alternative solutions. On the other hand, edge and foil winding provide a high fill factor, while at the same time provide lower AC copper losses than round conductors at high frequencies. Finally, litz wires are an interesting alternative to further reduce the AC losses in the winding at the expense of a higher cost and lower fill factor. Table 3.2[1] shows a representative range of costs for different types of windings. It should be noted that the specific cost depends on a variety of factors such as copper purity, conductor thickness, size, insulation class, purchasing volumes etc. Therefore, values outside this range could be expected. Similarly, the core material is preselected in order to reduce computational time. Depending on the application, the designer can select between electrical steel or ferrites of

---

[1] The presented cost ranges are obtained directly from industrial partners, for publicly available data please refer to [62]

different lamination thickness and/or grades; other core materials such as iron powder cores and Nanocristalline alloys could also be used but are not currently included in this work. Table 3.3[2] presents some of the attributes of different soft magnetic materials. It is worth noting that within each category there exists a large number of products and grades each with its own performance characteristics and associated cost. If it is desired to optimize the winding configuration or core material selection, an external loop can be added to the design of the magnetic component in order to test the different alternatives.

Table 3.2: Cost of different winding materials

Winding type	round wire	flat wire	foil	litz
Cost [€/kg]	$6-20$	$6-20$	$9-40$	$15-60$

Once all the required input data have been gathered, and the winding configuration and core material have been selected, the optimization of the magnetic component's geometry can be initiated. The first step consist in proposing a set of core geometries based on the requirements of the application. The core size is intentionally not discretized to standard sizes according to manufacturers' databases. Instead, it is assumed that all core dimensions can be freely varied (as shown in Fig. 3.6a). For each core geometry, analytic equations and reluctance networks are used to calculate the airgap(s) length (if applicable), the operating flux densities and to define possible winding arrangements that allow to achieve the desired inductance or transformation ratio.

For both inductors and transformers, the area product appears as an important quantity relating the winding and core cross section area with the energy stored (in the case of inductors) and the apparent power (in the case of transformers). This quantity is often used to select the size of magnetic cores, but it can only be used directly if good guidelines for the operating flux and current densities are available for similar applications and cooling conditions, which is not often the case. Nonetheless, all cores that are feasible solutions for the application at hand must fulfill the area product condition. However, not all cores that fulfill the area product condition would be feasible solutions for the application as this condition does not include thermal constraints and high frequency effects. With this in mind the main sizing equations for inductors and transformers are presented next:

Inductors

The area product condition for inductors is presented in (3.10), where $\hat{I}$ and I_{rms} are the peak and rms current respectively, K_w is the fill factor, the winding and core areas are represented by A_w and A_c respectively, J_{rms} is the current density and $\hat{B}_c$ is the peak flux density in the

---

[2] Material characteristics are summarized from [64–69]. The presented cost ranges are obtained directly from industrial partners, for publicly available data please refer to [62]

Table 3.3: Soft magnetic materials properties

Material	Ferrites	Amorphous (Fe)	Nanocristalline	Electrical Steel	GOES
Permeability μ_r [-]	$100-20k$	$10k-150k$	$15k-150k$	$1k-10k$	$20k-80k$
B_{peak} [T]	$0.2-0.5$	$0.7-1.8$	$1.2-1.5$	$1.2-2$	2
resistivity [$\mu\Omega$ m]	10^2-10^8	$1.2-2$	$1-2$	$0.15-0.7$	$0.46-0.49$
Cost [€/kg]	5.5	16	23	$1-15$	$1.2-2.5$

core. The area product condition is used to perform a preliminary screening of cores that would require either a too high current or flux densities in order to fulfil the demands of the application. This reduces computational time as unfeasible solutions are ruled out early in the evaluation process.

The required number of turns (N_t) can be calculated as a function of the desired inductance, peak current and maximum allowable flux density as shown in (3.11). Analyzing the reluctance of the geometry presented in Fig. 3.6a, the inductance can be expressed according to (3.12), where the reluctance of each element is calculated as shown in (3.13). It is important here to adjust the effective area of the airgap [70] in order to account for the effect of fringing flux, which affects the airgap's reluctance. In this work, the approach presented in [63] is used (3.14) as it is simple to compute and provides good accuracy. By combining (3.11)-(3.14) it is possible to calculate the required air gap length.

$$A_p = A_w A_c \geq \frac{L\,\hat{I}\,I_{rms}}{K_w\,J_{rms}\,\hat{B}_c} \tag{3.10}$$

$$N_t = \left\lceil \frac{L\hat{I}}{A_c\hat{B}_c} \right\rceil \tag{3.11}$$

$$L = \frac{N_t^2}{\Re_c + \sum \Re_g} \tag{3.12}$$

$$\Re = \frac{l}{\mu A} \tag{3.13}$$

$$A_g = (W_c + g)(d_c + g) \tag{3.14}$$

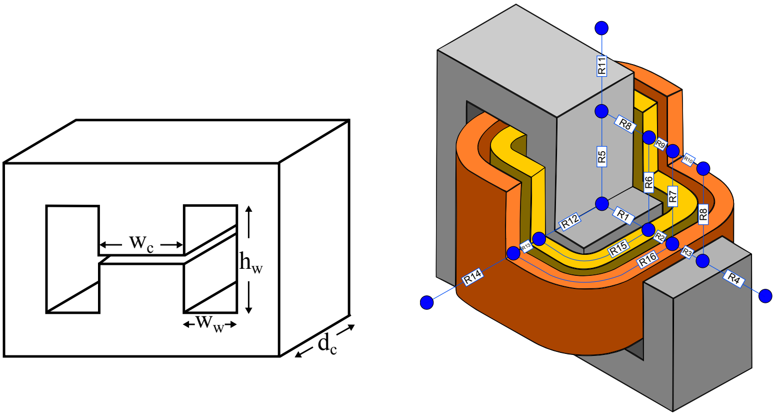

(a) Core geometry **(b)** Thermal Network

Figure 3.6: (a) Transformer/inductor core geometry (b) Lumped parameter thermal model.

Transformer

The area product condition for transformers is presented in (3.15), where $\sum VA$ is the sum of the apparent power in the different windings, K_f is the waveform coefficient (ratio between the rms and average value of the voltage) and f_s is the operating frequency. This expression is used in the same way as the area product expression for inductors previously explained. The number of turns in the primary winding of a transformer can be calculated according to Faraday's law as shown in (3.16); consequently, using the predefined transformation ratio (N), it is possible to compute the required number of turns in the secondary winding 3.17.

$$A_p = A_w A_c \geq \frac{\sum VI}{K_f K_w f_s J_{rms} \hat{B}_c} \tag{3.15}$$

$$N_{tp} = \left[\frac{\int_0^{DT} v(t) dt}{\hat{B}_c A_c} \right] \tag{3.16}$$

$$N_{ts} = [N_{tp} N] \tag{3.17}$$

Once both the airgap length (if applicable) and the windings layout are defined for the specific core geometry, it is necessary to evaluate if the proposed solution fulfills the thermal constraints. This requires a good estimation of the copper and core losses. In order to accurately compute the copper losses, a 2D analytic approach similar to the one presented in [65, 71–73] is taken. The selected approach uses the method of images to model the effect of the core in the distribution of the H-field in the windings. Moreover, airgaps can

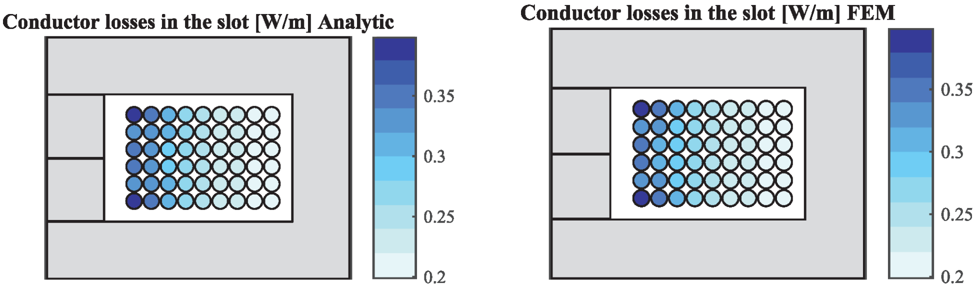

(a) Analytical calculation (b) Finite element

Figure 3.7: Comparison between the copper losses calculated analytically and by use of FEM.

be modeled as an additional current conductor with a magneto-motive force (MMF) equal to that in the actual airgap. In this way, it is possible to include proximity and skin effect losses in the conductor and to account for losses due to fringing flux from the air gap in a computationally efficient manner. In order to assess the accuracy of this approach, the results obtained from it have been compared to 2D finite element simulations for a certain slot geometry and winding layout (see Fig. 3.7). In this comparison each conductor carries a triangular wave current with a duty cycle of 25%, an average value of 3.3A, a peak of 4 A and a frequency of 10 kHz. The maximum discrepancy in the calculations occurs close to the airgap where the analytic method overestimates the losses up to 10% respect to the losses obtained by FEM. The average error in the winding is below 4.5% which is regarded as sufficiently accurate to be used for sizing magnetic components. On the other hand, the core losses are calculated using the modified Steinmetz equation (MSE) [74].

With all the losses calculated, a thermal network is used to estimate the hot spot temperature in the windings of the inductor or transformer. Since for sizing purposes only the steady state temperatures are of interest, the thermal network presented in Fig. 3.6b considers only the thermal resistances. Moreover, it is assumed that the components are potted; this is both to provide some level of mechanical protection and to improve heat transfer to the cooling surfaces.

In this work, the use of analytical calculations and thermal and reluctance networks is preferred over finite element analysis due to their fast execution and sufficiently high accuracy. However, it is worth noticing that additional steps need to be performed prior to the production of a final design. For example, the stray inductance and capacitance need to be calculated, the estimated losses can be compared with results from finite element simulations, the manufacturability of the proposed winding solution needs to be verified, etc.

Summarizing, the size of these components is determined as follows: first a large set of core geometries is proposed. Each one of the proposed cores is then evaluated to see if it fulfills the requirements of the application at hand; the number of turns, airgap length (if applicable) and operating flux densities are calculated. Once this is done, the copper and core losses are calculated and it is verified that the hot spot temperature is below the maximum allowable temperature for the selected winding class. From the initial set of proposed core geometries a subset of feasible cores is found. The final step is to select one geometry from this subset of feasible cores according to a criterion predefined by the designer. This criterion can be highest efficiency, lowest weight or minimum cost. This process is described in the inductor and transformer column of Fig. 3.9.

3.1.3 Capacitors

Among the bulkiest and most expensive components of the PEC are the power capacitors. Together with the magnetic components (i.e. transformers and inductors) they determine, to a great extent, the required dimensions of the housing.

In order to select the most appropriate capacitor for the application, several aspects need to be considered. First, the capacitor technology needs to be defined. The most common type of capacitors used in power electronics are metallized film and electrolytic. Depending on the application, one capacitor technology may be better suited than another. However, in general it can be said that electrolytic capacitors have a greater capacitance density, shorter life expectancy and lower current handling capabilities than film capacitors. The second aspect to consider is the voltage rating of the capacitor, which has to be selected to provide a margin with respect to the nominal operating voltage. This allows the capacitor to cope with voltage transients and extends its life expectancy. Thirdly, the capacitor must withstand the current stresses it is subject to without overheating or accelerating its degrading process. As a first approximation, the rated rms current at the operating frequency and temperature can be used as a guide [75], although in a final design a thorough analysis of the losses and the thermal cycling is required. Finally, it needs to be ensured that the peak and inrush currents are within the limits of the selected capacitor.

To demonstrate how the capacitor technology influences its characteristics, Fig. 3.8 presents the volume and current handling capabilities of capacitors for DC-link application as a function of technology, voltage and capacitance. It can be noticed that for a given voltage rating, both the volume and current are quite linear with the capacitance. Deviations from this approximation can be explained by the fact that capacitor manufacturers do not optimize the packaging of each capacitor independently but instead they try to reduce the number of packaging alternatives that they offer in their product range. It is worth mentioning that similar figures can be obtained for capacitors meant to be used in other applications such as snubbers and filters. However they are out of the scope of this work.

A database including capacitor technology, volume, cost, voltage rating and current handling capabilities is created in order to determine the capacitor characteristics for a given

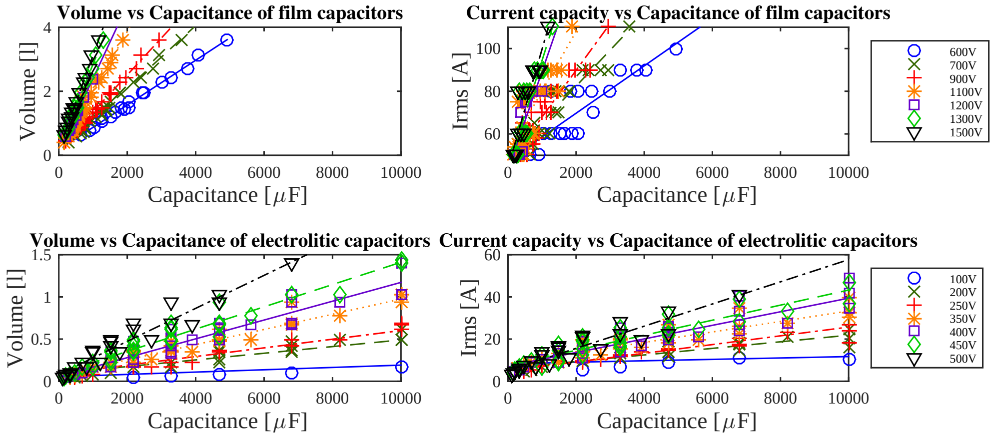

Figure 3.8: DC-link capacitors characteristics.

application. Interpolation is used to estimate the values if the required capacitor is not among the set of samples used to construct the database. This approach is feasible in reality since most capacitor manufacturers offer the alternative to produce tailored capacitors as long as they utilize existing technologies and the production volumes are large enough. Once all the characteristics of the capacitor are defined, its cost can be estimated using the cost model presented in [62].

3.1.4 Signal and control electronics

As previously mentioned, for cost purposes, all the required voltage, current and temperature sensors, communication and control processors, connectors and gate drivers are selected from a component database. The cost of sensors is dependent of the desired resolution, bandwidth and range; while the cost of gate drivers is associated with their peak current, driver voltage and whether isolation is required or not. On the other hand, the processors are manually selected before hand and the same processors are assumed to be used for converters of different power but intended for the same application. It is important to point out that a complete design of the different PCBs required is not part of this work. Nevertheless, a fixed offset cost is added to the PCB to account for all small electronic components such as capacitors, resistors, operational amplifiers, voltage regulators etc. In this way the major cost drivers related to signal and control electronics can be accounted for.

As it is presented in upcoming sections, the control unit and all signal electronics are a substantial cost driver in low power converters as a significant portion of their cost do not scale with the converter's power rating. Thus accounting for it is extremely important when comparing system designs that use converters of different power levels.

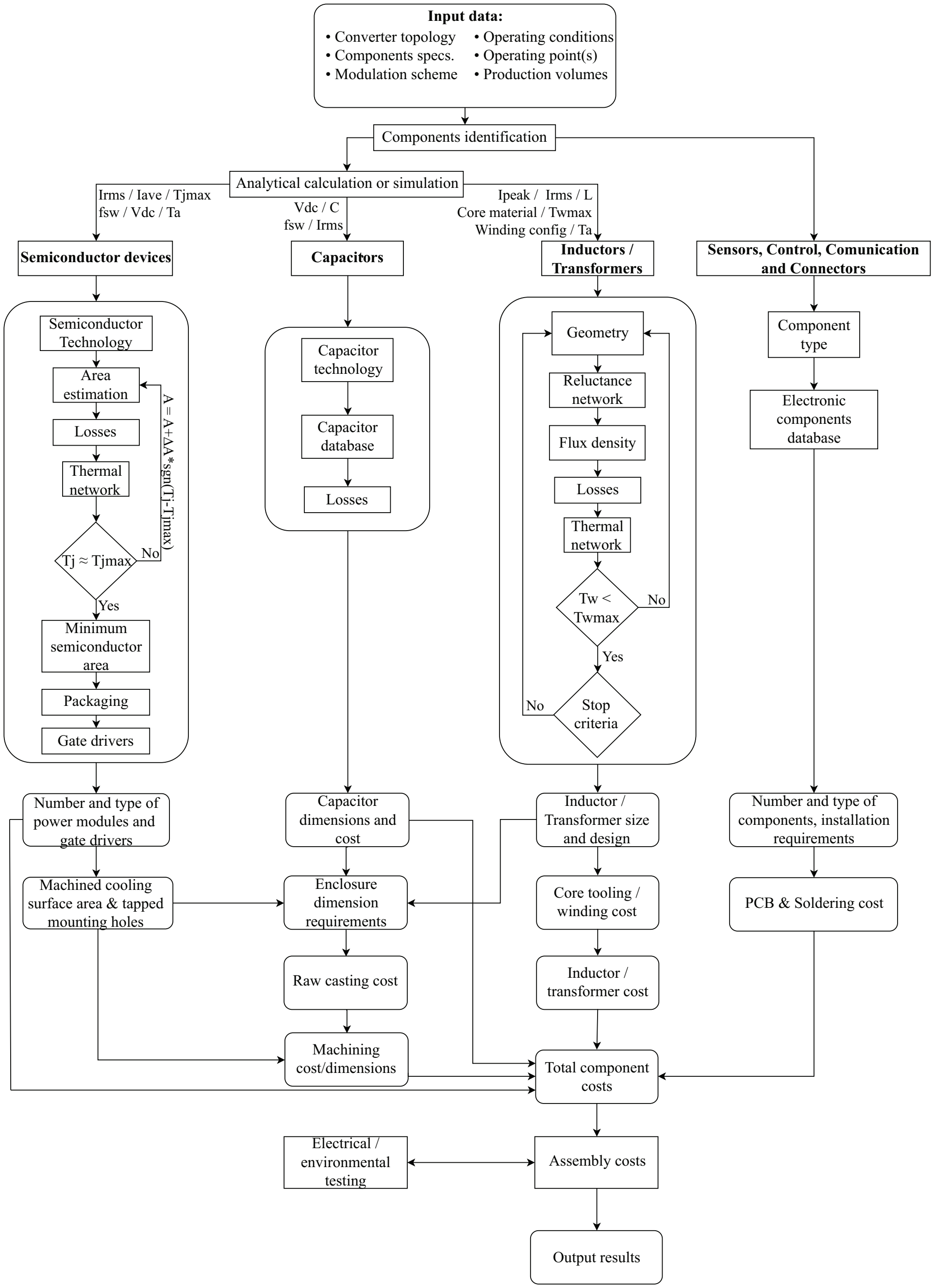

Figure 3.9: Flowchart describing the design and manufacturing of the main components of the power electronics converter as well as the assembly and testing of the complete converter.

3.1.5 Manufacturing and assembly

Once the main components in the PEC are sized and/or selected a good estimation of the dimensions and material cost of the converter can be obtained. Nonetheless, to transform silicon dies, copper wires, soft magnetic materials, capacitors, etc. into a functional converter several manufacturing processes need to be performed. For example, at the component level, the inductor's and transformer's coils need to be wound, their cores blanked and stacked or purchased, the different parts need to be assembled together and finally the completed component needs to be potted and tested. Similarly, capacitors need to be purchased, connected and potted while semiconductor devices are assumed to be purchased already packed in power modules. The housing needs to be cast or formed from metal sheets and the connectors need to be put in place. At the converter level, the different components need to be placed in the housing and connected together, cooling surfaces need to be machined to improve heat transfer and finally the whole unit needs to be sealed and both environmental and electrical testing need to be carried out in order to ensure that the converter performs as expected. All this is summarized in Fig. 3.9.

An in-depth analysis of the manufacturing steps needed to produce a PEC is out of the scope of this work. However, all the aforementioned manufacturing steps require different levels of investment and labor, ultimately contributing to the final cost of the converter. Moreover, design decisions define requirements and can even become constraints for the selection of the appropriate manufacturing processes and vice versa, existing production equipment, manufacturing tolerances, etc. are aspects that should be taken into consideration during early stages of the design.

3.1.6 Cost modeling

In automotive electrification, besides fulfilling performance requirements, cost reduction tends to be one of the main objectives. In order to accurately assess the cost effectiveness of a given solution it is necessary to develop tools able to estimate the cost of the different components using similar assumptions and constraints. For this reason, a complete cost model for PECs is developed in this work [57]. This model does not aim to calculate the cost of existing converters but rather to provide a cost estimation early in the design process, even before the first prototype is built, when there is still time to make adjustments or improvements. At this stage, not all the details of the converter are known, for example the control unit is not fully designed, the geometry of the housing is not yet optimized, etc. However, all major components are defined with sufficient level of detail so that a fairly accurate estimation can be carried out.

The developed cost model consists of two interconnected parts, one is the design and selection of all major components (previously explained) and the other one is the selection and optimization of all the manufacturing processes required to produce both the components themselves and the converter as a whole. This work focuses on the first part while the second one is described in high level of detail in [76].

The presented PEC model can be used to study the influence of relevant design parameters (e.g. rated power, DC-link voltage, production volumes, etc) on the overall cost of a converter for a certain application as it is shown in upcoming sections. It can also be included in the optimization of larger systems (e.g. electric powertrains). To be effective, it is important that the developed model is able to automatically transform requirements and inputs into cost estimations in a computationally effective manner. As inputs, this model requires not only all the information needed to size the different components (explained in detail in previous sections), but also data regarding the cost of "raw" materials and purchased components, cycle times and yield of different manufacturing processes, labor costs, etc. [76]. The input requirements are transformed by the first part of the PEC model ("design and selection") into geometrical and material definitions that are taken by the second section of the model ("manufacturing") to optimize the selection of manufacturing steps, and output the estimated cost of the converter at different production volumes. Additionally, the second section of the model also to provides a good idea on required manufacturing steps and level of investments needed for the converter under study.

3.1.7 Results

As it is stated at the beginning of this section, the developed model aims to estimate the performance, dimensions and cost of a given PEC. This model can be used both in the development of particular converters or in the optimization of larger systems in which the converter plays a key roll (as it is presented in upcoming chapters of this thesis). In order to demonstrate the type of results that can be expected from this model, the properties of a traction PEC for an electrified vehicle are estimated. In this context, a sensitivity analysis of the main design parameters affecting the cost of the converter is presented and examples of different efficiency maps that can be extracted from the model are shown.

This application represents an interesting case of study since it is highly sensitive to cost variations and some cost projections are available. For example, in [77] is reported that by 2015 a reasonable figure for an automotive PEC is 8 $/kW.

The selected converter topology is a three-phase, two-level, voltage source converter and the modulation scheme is SV-PWM. The converter is assumed to be liquid cooled with a cold plate temperature of 80 $^\circ C$. Due to the harsh environment that the converter is expected to operate in, an IP67 ingress protection level is selected.

As an example, a sensitivity analysis is only out based on production volumes, rated power

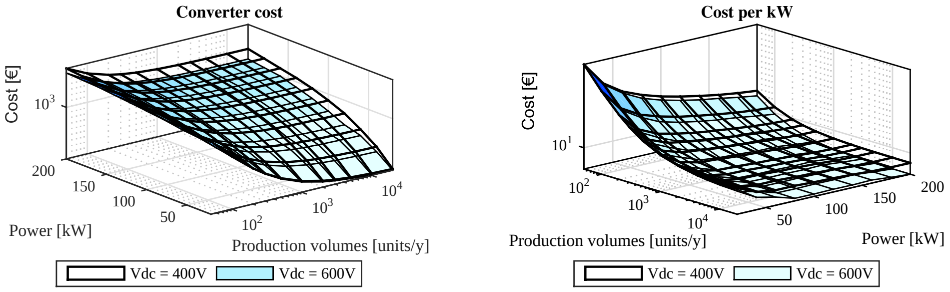

(a) Converter cost

(b) Converter cost per kW

Figure 3.10: Manufacturing cost (a) and manufacturing cost per kilowatt (b) of three-phase automotive converters for EV/HEV application. Each surface represents a different dc-link voltage rating, 600V (blue) and 400V (Transparent with black lines).

and dc-link voltage level. The switching frequency remains the same for all converters at 10 kHz and the semiconductor devices are Si Diode and field stop IGBT3 − 4. Film self-healing capacitors are used in the dc-link.

Fig. 3.10a shows the estimated manufacturing cost of a PEC rated for different powers and voltages under varying yearly production volumes. The first thing that can be noticed is that, for "high" power converters, the rated voltage has an impact on the cost. This can be explained by looking into the way that the two main components of the converter react to changes in the voltage/current combinations. Semiconductor devices normally lose current handling capabilities and increase their cost for the same die area at higher voltages, but simultaneously, as the voltage increases the current demands in the converter are reduced since the power is maintained constant. This leads to a slight increase in the cost of semiconductors for converters of lower voltages. On the other hand, the capacitor volume and current handling capabilities increase together with the voltage ratings but the capacitance requirement drops due to a drop in the current through the dc-link capacitor, reducing the final cost of the dc-link capacitor for converters of higher voltages.

The second aspect that is important to observe in Fig. 3.10a is that, at low production volumes, the impact of the rated power in the cost is low. The reason for this phenomenon is that at low production volumes most of the cost of the converter is related to covering the investments in production machines, tooling, fixtures and test equipment and the cost of the converter's components only represent a small fraction of the total cost. However, with an increase in the production volumes, the investment costs are distributed over a larger number of units and the cost of an individual converter drops significantly. This drop on the production cost also increases the cost difference between converters of different power levels.

A commonly used figure of merit for automotive PECs is their cost per kilowatt. Fig. 3.10b

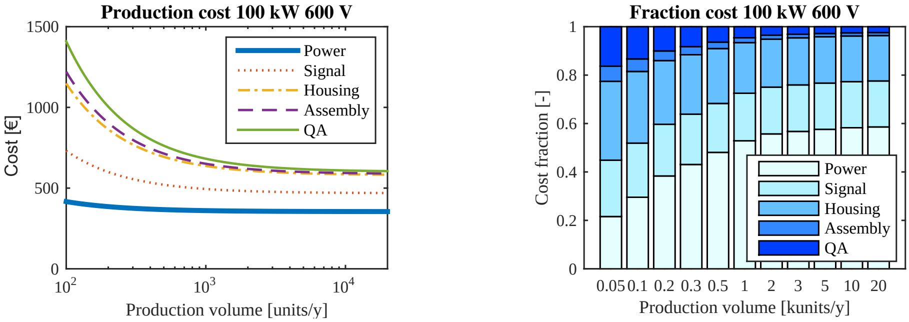

(a) Cost breakdown **(b)** Relative cost breakdown

Figure 3.11: Cost breakdown of a 100kW 600V automotive traction converter.

presents the cost per kilowatt for the same converters presented in Fig. 3.10a under the same voltage, power and production volume scenarios. It can be noticed that the cost per kilowatt drops together with increased rated power of the converter. The main reason for this behavior is that some of the converter's costs do not scale significantly with power (i.e control unit, transceivers, sensors) meaning that they have a greater impact in the total cost of lower power converters. Therefore, the use of constant figures of cost per kilowatt, as it is usually done in the literature, may produce to misleading results, hence the use of more accurate cost models, like the one presented in this work, is encouraged. Alternatively, if high level of detail in the cost estimation is not required, a linear cost function with a term that does not depend on the power rating of the converter can provide a better approximation than figures of cost per kilowatt.

Now that the cost tradeoffs have been described at a macro level, it is worth zooming into one particular converter to better understand the different elements that constitute the manufacturing cost and how they relate to production volumes. For this example it is assumed that the same converter design is used at all production volumes, which in reality is not likely to be the case, since a more cost effective solution may be based on off the shelf components if production volumes are expected to be low. Figure 3.11a presents a cost breakdown of a converter with a rated power of 100 kW and a dc-link voltage of 600 V. The same data is presented in relative values in Fig. 3.11b. It can be noticed that at low production volumes the costs related to the manufacturing of the housing, assembly and quality assurance dominate over the cost of the power and signal components. However, as production volumes increase, the investments in manufacturing equipment can be distributed among a higher number of converters, thus their relative influence on the overall cost of a converter is reduced while the impact of the power and signal components simultaneously increases. This is particularly important since it shows that an analysis based solely on material cost does not result in accurate estimations, specially at low production volumes. Therefore, in order to produce fair comparisons it is necessary to account for the additional cost incurred during manufacturing.

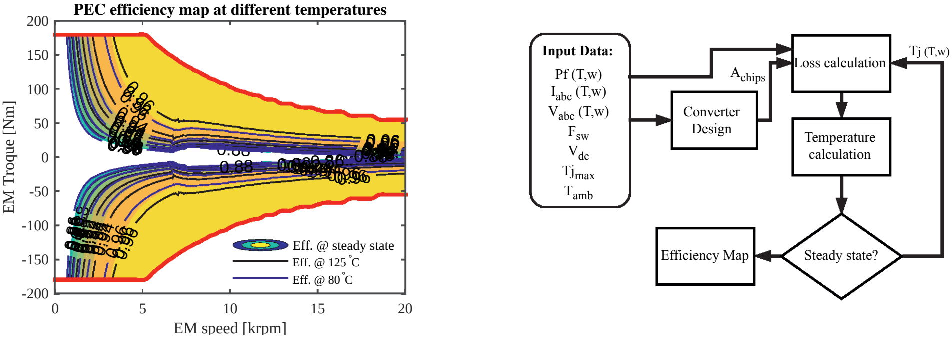

(a) PEC efficiency map at different temperatures

(b) Loss calculation procedure

Figure 3.12: Influence of the junction temperature on the efficiency map of a PEC.

The developed PEC model is capable of estimating not only the cost but also the performance of the converters. One of the most common ways of assessing the performance of a converter is by looking at its efficiency at different operating points. In the particular case of an automotive traction converter, efficiency maps can be created if the power factor, phase current and phase voltages of the EM at each torque and speed combination are known. With this information it is then possible to first size the converter for the most challenging operating point and then estimate the losses of such a converter in all possible torque and speed combinations. As it is explained previously in this chapter, the junction temperature has an impact on the magnitude of the semiconductor losses. Therefore, slight differences in the efficiency maps are to be expected depending on the current temperature of the semiconductors.

The impact of the junction temperature in the efficiency map of a converter can be clearly observed in Fig. 3.12a where efficiency maps for an automotive PEC with a rated power of 100 kW, a dc-link voltage of 600 V and using a switching frequency of 10 kHz throughout the whole speed range are calculated assuming junction temperatures of $125^{\circ} C$ and $80^{\circ} C$, in black and blue lines respectively. Additionally, Fig. 3.12a shows the steady state efficiency map, which corresponds to the expected efficiency if the operating point is sustained long enough for the thermal equilibrium to be reached. This last efficiency map is calculated using the procedure shown in Fig. 3.12b. From Fig. 3.12a it can be observed that, as expected, higher temperatures lead to slightly lower efficiencies due to the positive temperature coefficients for both the switching losses and resistance of the different semiconductors (refer to Table 3.1). However, the general shape of the efficiency map is preserved regardless of the operating temperature (within reasonable limits).

Moreover, in automotive applications it is not uncommon to adjust the switching frequency depending on the electrical frequency of the EM in order to reduce the switching losses in

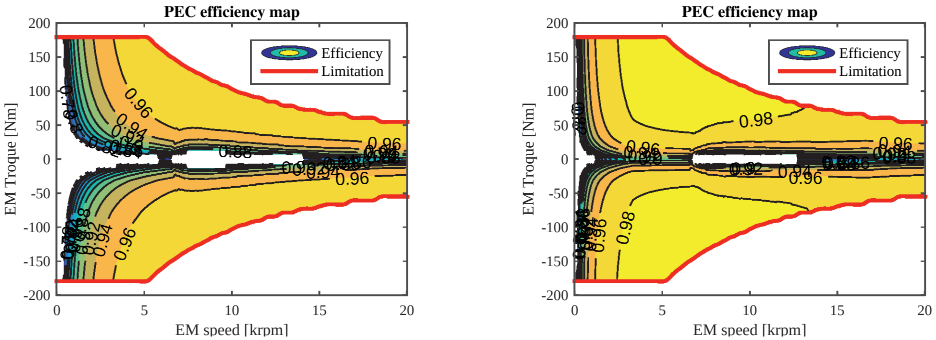

(a) Fixed switching frequency (10kHz) **(b)** Variable switching frequency (2 — 10kHz)

Figure 3.13: PEC efficiency maps using different switching frequencies.

the PEC [78]; although, this has the drawback of increasing the THD of the currents which translates into an increase in the EM losses, torque ripple, and eventually second order effects like mechanical stresses due to increased vibration levels and higher noise. Nonetheless, focusing only on the PEC losses, Fig. 3.13 shows the efficiency maps for the same PEC previously described if a fixed (Fig. 3.13a) or a continuously varying (Fig. 3.13b) switching frequency is used. In Fig. 3.13b it is assumed that the switching frequency is twelve times higher than the electrical frequency of the EM within the range of $2 - 10$ kHz. Although from these figures it is possible to observe that a significant improvement in the PEC efficiency can be achieved by reducing the switching frequency at lower speeds, it is necessary to look at the impact of this practice in the EM losses, in order to find a solution that minimizes the overall losses of the system. Additionally, instead of using a continuously varying switching frequency many applications use a discrete number of switching frequencies which would generate an efficiency map somewhere in between the ones presented in Fig. 3.13.

3.2 Electrical machines

The EM converts electrical to mechanical energy and vice versa. In many applications, they constitute the interface between the PEC and the MT. Therefore, the EM characteristics and properties have a direct impact on all the components surrounding it. The literature is abundant with works dealing with the optimization of a given EM designs to fulfill certain requirements. This work, on the other hand, takes a slightly different approach and aims to develop models and procedures to optimize larger systems in which the EM is just one of the components.

In this context, defining before hand the desired attributes of the EM is a challenging task

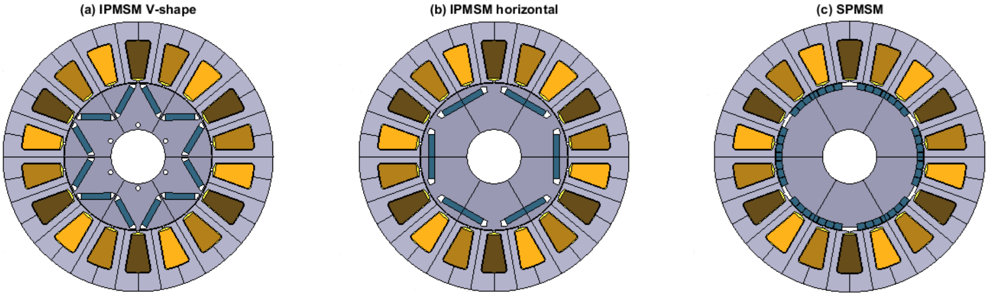

Figure 3.14: Electrical machine geometries included in this work. (a) VIPMSM, (b) IPMSM and (c) SPMSM.

as it depends on the specifics of the application and the configuration of the system under study. For example, some applications might benefit from EMs with large constant power speed range (CPSR), o high overloading capabilities while other may need higher efficiency or being easier and cheaper to manufacture. Therefore, using a single EM design to serve as a "base machine" can lead to biased results even if this initial design is then scaled. Moreover, most scaling methods ensure that the electromagnetic characteristics of the scaled machine remain similar to those of the "base machine" but they do not guarantee the same for the thermal loading. This might cause some scaled machines to require additional cooling or to not take full advantage of their thermal potential. As cooling and thermal management of the EMs is a great concern in many applications (e.g. when designing an electric power-train), in this work a more empirical approach is suggested for the selection and scaling of the EM. This approach is based on the generation of a database of relevant EM designs and the use of thermal lumped parameter models to adjust the nominal current loading when adjusting the number of turns and/or axially scaling the machine. The aforementioned database includes different EM topologies and a large number of distinct geometries.

Following, the process of characterizing the performance of an EM design, analyzing the results and storing all relevant information in an structured manner in an EM databased for its later use is described.

3.2.1 Performance characterization

In this work, three different EM topologies are considered. The first two topologies are interior permanent magnet synchronous machines (IPMSM), one with the magnets placed in "V" and one with the magnets placed tangentially. The last geometry is a surface mounted permanent magnet synchronous machine (SPMSM) as shown in Fig. 3.14. However, it should be noted that other EM topologies can be included using the same procedure as presented in this section.

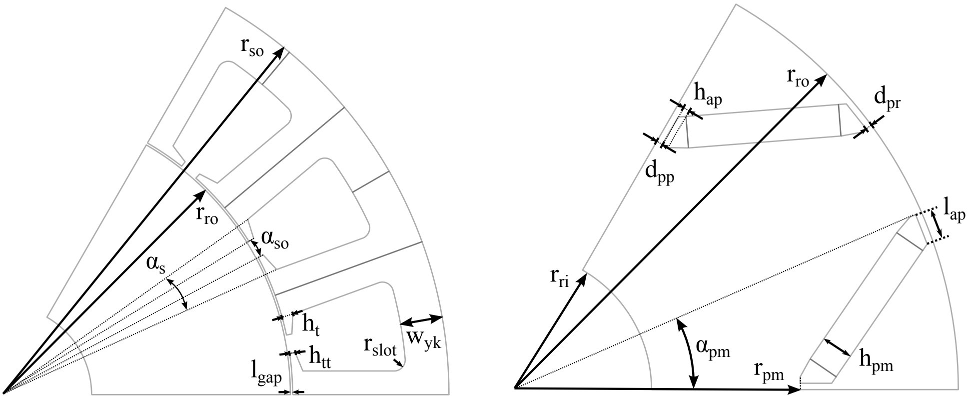

(a) Stator geometry **(b)** V-shape IPMSM rotor geometry

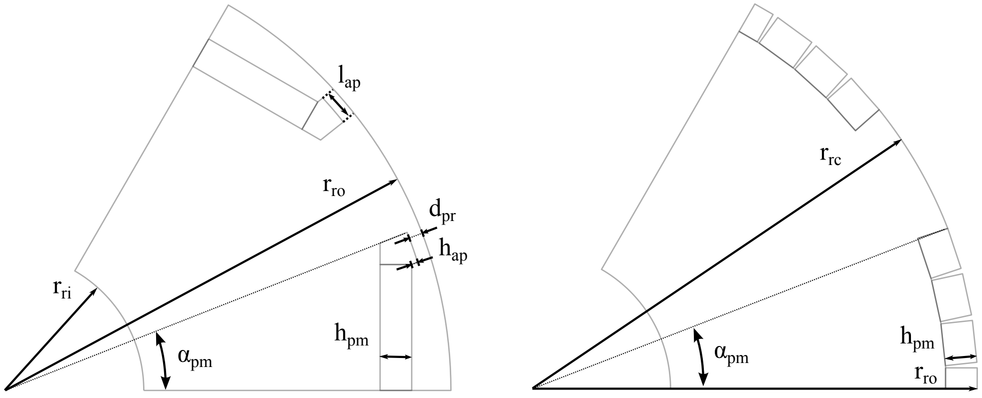

(c) IPMSM rotor geometry **(d)** SMPMSM rotor geometry

Figure 3.15: Parametrization of the different EM topologies.

In order to estimate the thermal and electromagnetic performance of a given EM design, minimum size 2D FE models (refer to Fig. 3.14 for geometry/CAD models) [79] are used. Since a large number of EM designs are to be evaluated, the process of generating each geometry in the finite element software needs to be automated, which implies that the geometries of the different topologies need to be parametrized. As it could be expected, a relatively large number of parameters is needed in order to fully define an EM geometry as it is shown in Fig. 3.15. Note that in the aforementioned figure the parametrization of the stator geometry is the same for all three topologies. Moreover, on top of the geometrical parameters presented in Fig. 3.15 the number of poles (N_p) and the numbers of slots per pole and phase (q) can also be varied.

The simulation process initiates with the generation of a specific EM geometry based on a predefined number of input parameters. First a thermal simulation is performed to identify

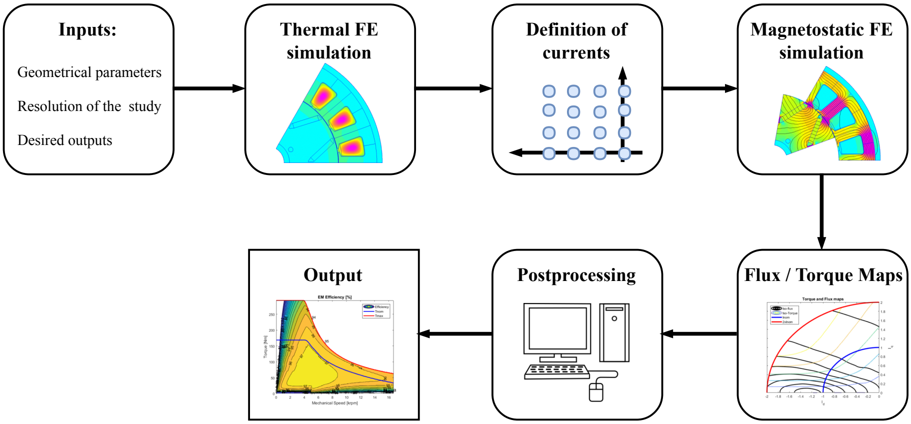

Figure 3.16: Performance evaluation of a given EM geometry.

the nominal current loading of the proposed geometry. Afterwards, a set of magneto-static simulations are carried out at different current combinations and rotor positions. The set of current combinations is defined based on the previously calculated nominal current, with simulations being carried out both below and above this value. Since all the machines under study are assumed to use distributed windings, the rotor is rotated in small steps over a span of 60 electrical degrees in order to quantify the variations in flux densities, torque and flux linkage. This process is summarized in Fig. 3.16. It is worth noticing that all FE simulations are carried out assuming single turn windings and during the post-processing this is adjusted to account for the voltage limitation.

The EM simulations carried out for this work take advantage of a software tool that has been developed in the Division of Industrial Electrical Engineering and Automation (IEA) at Lund University [80]. This tool serves as an interface between Matlab and FEMM [81] and allows the EM designer to carry out different analysis on a variety of EM topologies. In this work, the core of this software is preserved and changes on the geometries and type of analysis are implemented. Although this is a very convenient tool, the methodology and approach presented in this work is by no means limited to the used of the aforementioned software and could be implemented in most finite element packages and numerical computing environments.

Once the simulations are completed the post-processing of the obtained data begins. With the voltage limitation, number of turns and control strategy defined beforehand it is possible to determine the current combination at each operating point. In this work, maximum torque per ampere (MTPA) is selected as control strategy, thus for each torque and speed operating point the optimal current combination is selected according to (3.18).

$$\begin{aligned} Minimize : f = |\vec{i_{dq}}| \\ s.t: T(i_d, i_q) = T_{req} \\ \omega = \omega_{req} \\ |\vec{v_{dq}}(i_d, i_q, \omega)| \leq v_{max} \\ |\vec{i_{dq}}| \leq i_{max} \end{aligned} \tag{3.18}$$

Since the flux densities in the center of the stator teeth and yoke are obtained from the FE simulations and the properties of the different materials are known, it is possible to estimate the iron losses using (3.19) and (3.20). In the aforementioned equations k_{hyst}, k_{eddy} and k_{ex} are constants that can be derived from the material's datasheet as shown in Fig. 3.17 for laminated steel $M250-35A$, which results in the coefficients presented in Table 3.4. Moreover, as the stator resistance can be estimated from the EM geometry, the copper losses can be calculated as shown in (3.21). Knowing the mechanical power and the different losses it is possible to compute the efficiency map of an EM.

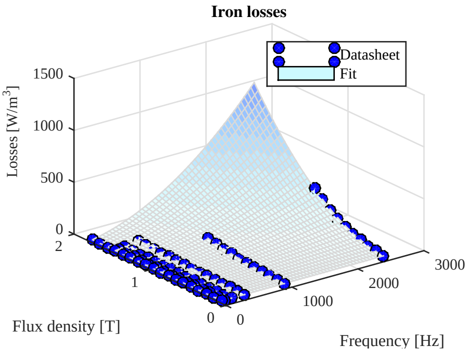

Figure 3.17: Core losses map for $M250-35A$.

Coefficient	Value
k_{hyst}	0.03336
k_{eddy}	4.049×10^{-5}
k_{ex}	3.511×10^{-7}

Table 3.4: Core Loss coefficients for $M250-35A$

$$P_{fe,tooth} = V_{tooth}\left(k_{hyst} f B_t^2 + k_{eddy}\left(f B_t\right)^2 + k_{ex}\left(f B_t\right)^{1.5}\right) \tag{3.19}$$

$$P_{fe,yoke} = V_{yoke}\left(k_{hyst} f B_y^2 + k_{eddy}\left(f B_y\right)^2 + k_{ex}\left(f B_y\right)^{1.5}\right) \tag{3.20}$$

$$P_{cu} = I_{rms}^2 R_s \tag{3.21}$$

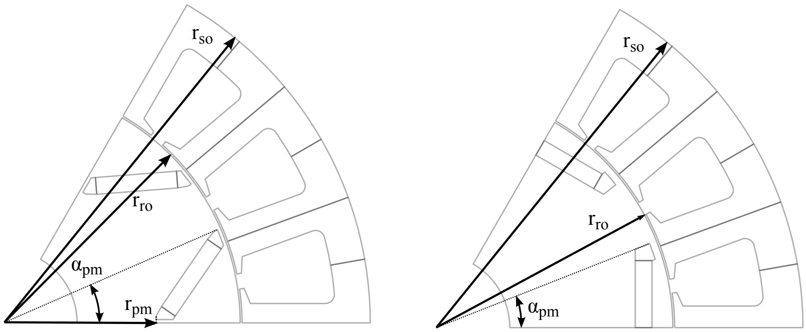

(a) Parameters varied in V-shape IPMSM (b) Parameters varied in IPMSM

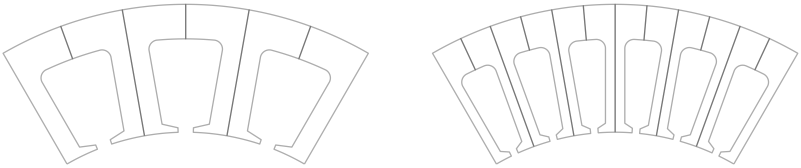

(c) Stator geom $k_{iron} = 0.9$ and $q = 1$ (d) Stator geom $k_{iron} = 0.9$ and $q = 2$

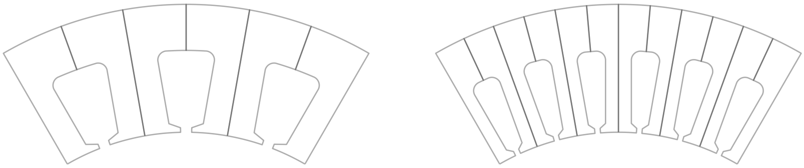

(e) Stator geom $k_{iron} = 1.2$ and $q = 1$ (f) Stator geom $k_{iron} = 1.2$ and $q = 2$

Figure 3.18: Parameters varied to create the EM database.

3.2.2 Database generation

The main objective of generating a database of EMs is to reduce the computational time during the analysis and optimization of larger systems (e.g. an electric powertrain) by using pre-computed results instead of performing time consuming simulations inside the optimization loop. With this in mind the EM database has to be comprehensive enough to capture the most relevant interactions between different design parameters, but sufficiently small in order for it to be considered a practical tool. In this context, for each EM topology, some selected geometrical parameters are varied in order to map the performance implications of such changes [82]. It is the designer's job to select which geometrical parameters are to be varied and with which resolution. To do this, previous experience or preliminary tests can be of help. The parameters varied in this work to generate the EM database are: the stator outer radius (r_{so}), permanent magnet angle (α_{pm}), ratio between rotor and stator outer radii (r_{ro}/r_{so}), the slot size (k_{iron}), the number of poles and slots (q) and in the case of the V-shape IPMSM the permanent magnet inner radius (r_{pm}). It is worth mentioning that

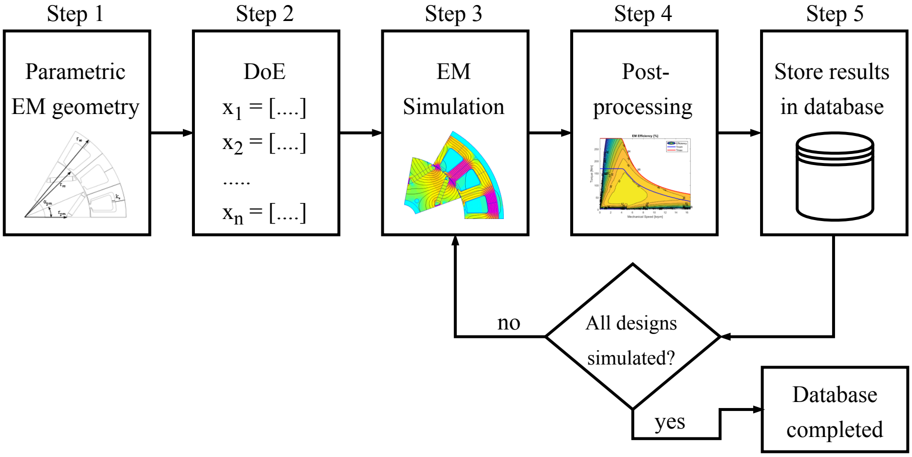

Figure 3.19: Electrical machine database generation.

k_{iron} is a dimensionless parameter that affects the slot size, while keeping the ratio between the tooth and yoke width constant. All this parameters can be observed in Fig. 3.18. Note that the geometry of the SPMSM is not shown as the varied parameters are the same as for the IPMSM. Moreover, Fig. 3.18 also shows the changes in the stator geometry when varying the slot size from its minimum to its maximum relative value for both one and two slots per pole and phase. A list of the parameters varied for each EM topology as well as the explored values is presented in Table 3.5. Only the two combinations of number of poles that give a pole pitch of about $50mm$ are studied for each EM outer radius. Taking all these parameters into consideration, the EM database generated for this work contains 3840 EM geometries, of which 1920 are V-shape IPMSM, 1280 are IPMSM and the remaining 640 are SMPMSM.

During the process of generating the EM database, each one of the selected geometries is analyzed in order to determine their thermal and electromagnetic characteristics as explained in the previous section. The obtained information is then used together with a pre-defined voltage limitation to calculate the single turn current, fluxes and losses at each torque / speed combination within the operating range of the machine according to the selected control strategy (MTPA in this case). The use of a pre-defined voltage limitation does not impose a constraint in the optimization, as this can be later modified by adjusting the number of turns as explained in section 3.2.4. By doing this, the computational time required to scale the performance of a given machine can be reduced. This process is summarized in Fig. 3.19. For each EM design, its geometry and material specifications are stored in the database, together with all the information summarized in Table 3.6.

From the aforementioned table it is possible to notice that look-up tables for the losses, power factor, fluxes and currents as a function of the torque and speed vectors are stored.

Table 3.5: Parameters varied to create the EM database

V-shape IPMSM

Parameter	Values	Units
r_{so}	$[85; 100; 120; 145; 170]$	mm
k_{iron}	$[0.9; 1; 1.1; 1.2]$	-
${}^{r_{ro}}/_{r_{so}}$	$[0.6; 0.65]$	-
q	$[1; 2]$	-
N_p	$[6; 8; 10; 12]$	-
α_{pm}	$({}^{\pi}/_{N_p})[0.7; 0.78; 0.86; 0.95]$	rad
r_{pm}	$(r_{ro} - r_{ri})[0.5; 0.6; 0.7]$	mm

IPMSM

Parameter	Values	Units
r_{so}	$[85; 100; 120; 145; 170]$	mm
k_{iron}	$[0.9; 1; 1.1; 1.2]$	-
${}^{r_{ro}}/_{r_{so}}$	$[0.5; 0.55; 0.6; 0.65]$	-
q	$[1; 2]$	-
N_p	$[6; 8; 10; 12]$	-
α_{pm}	$({}^{\pi}/_{N_p})[0.7; 0.78; 0.86; 0.95]$	rad

SPMSM

Parameter	Values	Units
r_{so}	$[85; 100; 120; 145; 170]$	mm
k_{iron}	$[0.9; 1; 1.1; 1.2]$	-
${}^{r_{ro}}/_{r_{so}}$	$[0.6; 0.65]$	-
q	$[1; 2]$	-
N_p	$[6; 8; 10; 12]$	-
α_{pm}	$({}^{\pi}/_{N_p})[0.7; 0.78; 0.86; 0.95]$	rad

Moreover, the different components of the losses are stored separately in order to facilitate the scaling process as they have different dependencies on the axial and number of turns scaling as it is explained in future sections. Additionally, as the EM model is meant to be used in conjunction with the PEC model, it is important to store the power factor at all operating points as it has an effect on the converter losses.

With the information available in the database, it is possible to axially scale and adjust the number of turns of each EM geometry in order to meet the torque/power requirements of the application and derive their efficiency and thermal characteristics.

Table 3.6: EM database parameters

Symbol	Meaning
N_p	Number of poles
T^*_{vec}	Torque vector
ω^*_{vec}	Speed vector
$I^*_{so,dq}(w,t)$	Single turn current
$\Psi^*_{so,dq}(w,t)$	Single turn linked flux
$R^*_{so,act}$	Single turn resistance inside the slot
$R^*_{so,end}$	Single turn resistance in the end windings
$pf^*(w,t)$	Power factor
$P^*_{cu,act}(w,t)$	Copper losses inside the slots
$P^*_{cu,end}(w,t)$	Copper losses in the end windings
$P^*_{hys,yk}(w,t)$	Hysteresis Losses in the stator yoke
$P^*_{eddy,yk}(w,t)$	Eddy current Losses in the stator yoke
$P^*_{exc,yk}(w,t)$	Excess Losses in the stator yoke
$P^*_{hys,th}(w,t)$	Hysteresis Losses in the stator tooth
$P^*_{eddy,th}(w,t)$	Eddy current Losses in the stator tooth
$P^*_{exc,th}(w,t)$	Excess Losses in the stator tooth

3.2.3 Thermal modeling

Thermal management of EM is a great concern, specially in traction applications. For this reason, a dynamic lumped parameter thermal model is used in this work to ensure that the thermal constraints are always satisfied both during the scaling process (to define nominal current loadings) and throughout the different drive cycle simulations. Moreover, the aforementioned thermal model is used in the drive cycle simulation to monitor the temperature evolution of the different sections of the EM, and to limit the overloading potential depending on the current hot spot temperature. The thermal model used in this work is an adaptation of the one presented in [83]. However, since the intention is to analyze different EM geometries, the thermal model is adapted to receive varying geometrical parameters and to adjust the different thermal resistances and capacitances accordingly.

The thermal model consists of 8 nodes which correspond to the temperatures in the outer case, stator yoke and teeth, winding inside the slot and in the end turns, magnets, rotor shaft and bearings as shown in Fig. 3.20. The different loss maps included in the database (refer to section 3.2.2) are used to provide the different nodes with the respective losses depending on the current operating point.

In this work, it is assumed that all EM designs use the same form of cooling: in particular, forced convection through the outer case (with a heat transfer coefficient of $600\,W/(m^2K)$) towards an $80°C$ coolant fluid. On the other hand, the thermal constraints are defined depending on the selected materials, in this case the maximum allowable temperature for the windings is set to $150°C$ (assuming insulation class F) and $120°C$ for the permanent magnets (assuming H rated). These values can be varied in order to study the impact of alternative cooling solutions or materials. However this would introduced additional degrees of freedom which, specially when optimizing larger systems (as it is presented in Chapter 4), can yield to a significant increase in the size of the optimization problem. Therefore, this values are kept constant throughout this work.

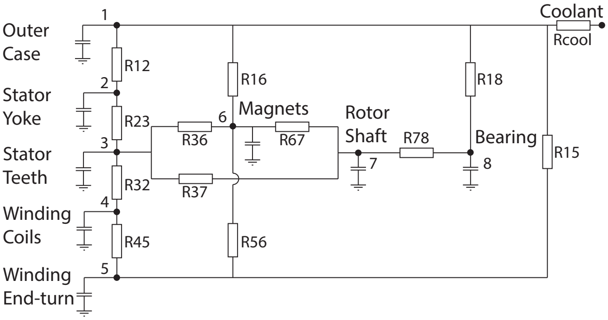

Figure 3.20: Thermal lumped parameter model for EM.

3.2.4 Scaling

The electrical machine performance and characteristics are scaled based on three factors: the change in the EM length (k_A); the desired number of turns (N_t) and the ratio between peak and nominal current (k_{ov}). Additionally, thermal and mechanical constraints are observed throughout the scaling process.

When performing axial scaling of an EM thermal aspects need to be considered. In general, when the EM is being cooled by conventional methods, a significant portion of the heat generated in the end-windings travels first into the slots and then to the stator core, from which it is dissipated by convection (natural and/or forced) in the housing or water jacket. If the cooling conditions are kept constant, when the active length of the machine is reduced its nominal current density (and therefore its performance) needs to be reduced accordingly, since the heat from the end windings represents a higher fraction of the total heat transferring from the slot to the core. On the other hand, when the machine length is increased the nominal current density can be potentially increased.

Moreover, axial scaling has other implications in the performance of the EM besides that of affecting the nominal current density. The following explanation is given assuming a single turn winding in order to focus only on the effects of axial scaling. The combined effect of the different scaling parameters are presented at the end of this section. To begin with, a change in the axial length of the EM has a linear effect on the output torque at a given current vector. At the same time, when varying the axial length of the machine, the volume of the different core sections increases proportionally but the flux densities remain unchanged (for the same current combination), which leads to a linear increase in the core losses. Additionally, the length of the end-windings is not altered by changes in the active length of the EM, thus their associated losses remain the same while the copper losses due to the fraction of the windings inside the slots scale together with the EM length.

Scaling the number of turns (N_t) is essential to adjust the EM voltage to the desired dc-link voltage and to change the base speed value. The main premise of the N_t scaling is that the current density inside the slot is kept constant, thus for a given dc-link voltage increasing N_t decreases the base speed and vice-versa. Additionally, since the current density is kept constant the EM torque does not change when the number of turns is adjusted, however, the phase currents and therefore the PEC rating and cost increase as N_t is reduced.

With current, flux and torque maps as well as the stator resistance being adjusted by the new length (k_A) and change in the number of turns (k_{nt}) of the EM, it is possible to recompute the control strategy in order to determine the optimal current combination at each torque and speed operating point. However, as previously mentioned, in this work a different approach is suggested: the precomputed look-up tables stored in the database can be used to estimate the performance at any operating point (w_n, t_n) if the speed is adjusted by the change in number of turns and the torque by the change in the active length $({}^{w_n}/_{k_{nt}}, {}^{t_n}/_{k_L})$. This implies that the presented scaling procedure is based on linear combinations and thus extremely fast to execute.

However, for N_t different than $N_{t,ideal}$ this procedure is not an exact solution to the MTPA for the scaled EM. This is due to the fact that when selecting a current vector (I_{dq}) for a given operating point (w_n, t_n), the change in the winding resistance (R_s) is being neglected. Nonetheless, the difference between the complete re-calculation of the MTPA and the results obtained by the proposed set of equations is rather small within the voltage/power levels studied in this work. This is demonstrated in Fig. 3.21 where the same EM design is scaled at different lengths and number of turns. In this figure it can be observed that the error introduced in the efficiency maps during the scaling process is very small, specially if the number of turns is not extreme, and therefore it is not expected to affect the outcome of the optimizations.

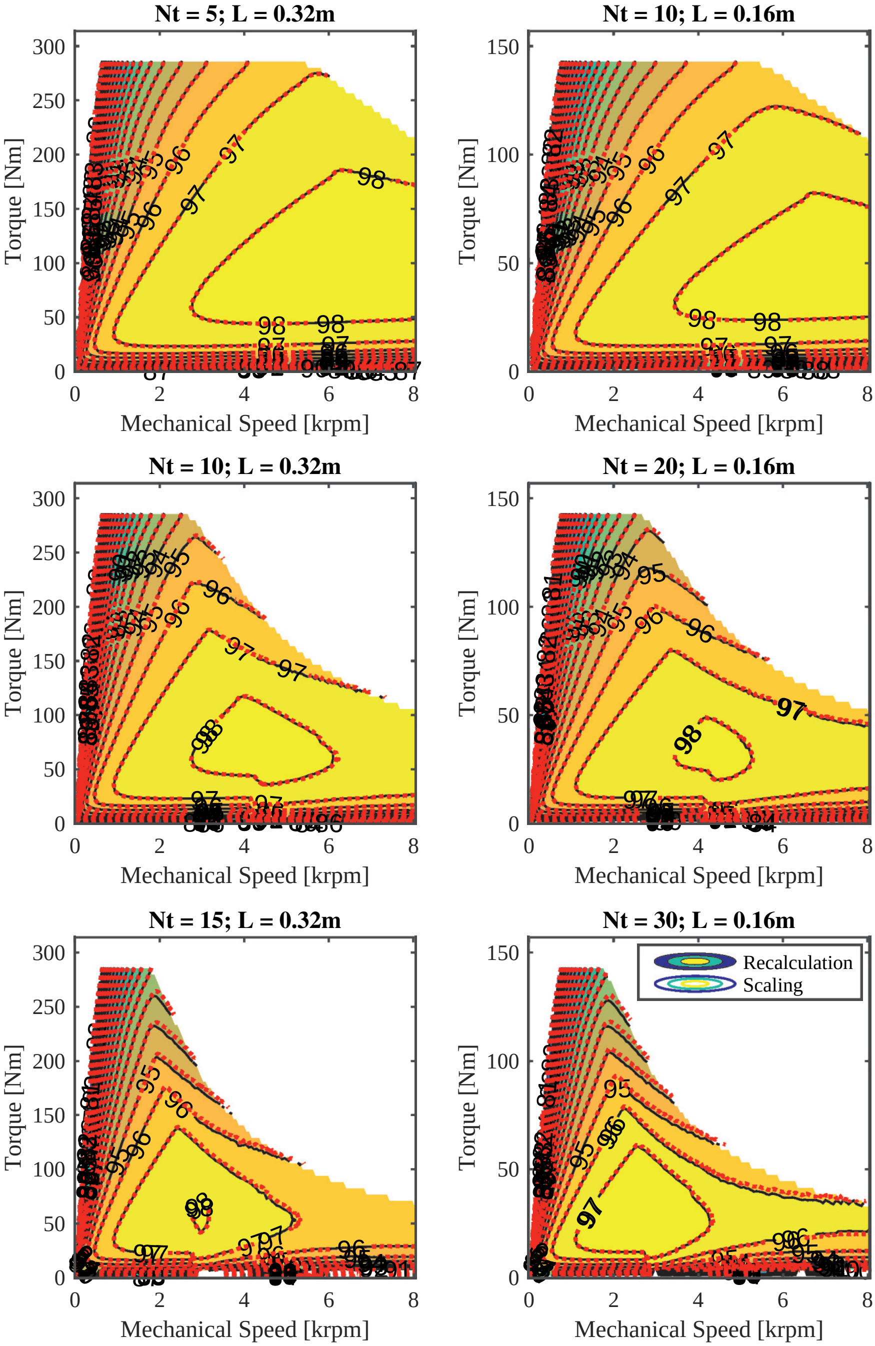

Figure 3.21: Comparison between efficiency maps obtained from recalculation of MTPA and the proposed scaling methodology.

The final scaling factor introduced in this work is the overloading factor (k_{ov}) which defines which operating points (w_n, t_n) are attainable above the nominal current loading. Its main influence is on the current rating of the PEC and therefore its cost. However, the overloading factor also limits the amount of time that a given EM can sustain peak torque. For example, given a peak torque requirement, a small machine with a high k_{ov} probably is able to sustain the overloading condition for a very short period of time and might operate at higher saturation levels (thus requiring a higher current rating from the PEC) than a larger machine with a lower k_{ov}.

$$R_s = (k_A \; R^*_{so,act} + R^*_{so,end}) \; N_t^2 \tag{3.22}$$

$$I_{s,dq}(w_n, t_n) = I^*_{so,dq}({}^{w_n}/_{k_{nt}}, {}^{t_n}/_{k_A}) / N_t \tag{3.23}$$

$$\Psi_{s,dq}(w_n, t_n) = \Psi^*_{so,dq}({}^{w_n}/_{k_{nt}}, {}^{t_n}/_{k_A}) \; k_A \; N_t \tag{3.24}$$

$$\begin{aligned} V_d(w_n, t_n) = {} & R_s \; I_d({}^{w_n}/_{k_{nt}}, {}^{t_n}/_{k_A}) \\ & - w_n \; \Psi_q({}^{w_n}/_{k_{nt}}, {}^{t_n}/_{k_A}) \end{aligned} \tag{3.25}$$

$$\begin{aligned} V_q(w_n, t_n) = {} & R_s \; I_q({}^{w_n}/_{k_{nt}}, {}^{t_n}/_{k_A}) \\ & + w_n \; \Psi_d({}^{w_n}/_{k_{nt}}, {}^{t_n}/_{k_A}) \end{aligned} \tag{3.26}$$

$$V_{s,max} = max\left(\sqrt{V_d^2(w_n, t_n) + V_q^2(w_n, t_n)}\right) \tag{3.27}$$

$$pf(w_n, t_n) = pf^*\,({}^{w_n}/_{k_{nt}}, {}^{t_n}/_{k_A}) \tag{3.28}$$

$$N_{t,ideal} = m_{max} \; V_{dc} \; / \; (\sqrt{2} \; V_{dq,max}) \tag{3.29}$$

$$P_{cu,act}(w_n, t_n) = k_A \; P^*_{cu,act}({}^{w_n}/_{k_{nt}}, {}^{t_n}/_{k_A}) \tag{3.30}$$

$$P_{cu,end}(w_n, t_n) = P^*_{cu,end}({}^{w_n}/_{k_{nt}}, {}^{t_n}/_{k_A}) \tag{3.31}$$

$$P_{fe,eddy}(w_n, t_n) = k_A \; k_{nt}^2 \; P^*_{fe,eddy}({}^{w_n}/_{k_{nt}}, {}^{t_n}/_{k_A}) \tag{3.32}$$

$$P_{fe,hys}(w_n, t_n) = k_A \; k_{nt} \; P^*_{fe,hys}({}^{w_n}/_{k_{nt}}, {}^{t_n}/_{k_A}) \tag{3.33}$$

$$P_{fe,exc}(w_n, t_n) = k_A \; k_{nt}^{1.5} \; P^*_{fe,exc}({}^{w_n}/_{k_{nt}}, {}^{t_n}/_{k_A}) \tag{3.34}$$

Considering all the previous points, the different values for the new scaled machine for a given speed/torque operation point (w_n, t_n) can be calculated using (3.22)-(3.34).

Where k_A is the ratio between desired EM length and the one used in the FE simulations (1 m). k_{nt} represents the ratio between the scaled EM's base speed and the one obtained when calculating the MTPA with the pre-defined voltage limitation. This approximates to the ratio between the ideal number of turns and the selected one $({}^{N_{t,ideal}}/_{N_t})$, and can be found with a simple line search around this point. m_{max} is the maximum desirable modulation index (0.9 in this case).

Once all these quantities are scaled, the lumped parameter thermal model described in section 3.2.3 is used to determine the new nominal current density, and both the nominal and peak torque vs speed envelopes are adjusted accordingly. After that, new efficiency and loss maps are generated to be used in powertrain simulations.

3.2.5 Manufacturing and cost estimation

As previously mentioned for the PEC, the cost effectiveness of an EM design cannot be looked upon in isolation from the system where it operates. Therefore, models able to estimate the cost of the different components under similar assumptions are needed. In this context, this work has contributed to the development of a comprehensive cost model for EMs that can be used in early stages of the design process, when a final design of the EM, its housing and cooling system is not available; however, sufficient data regarding the EM geometry, materials, expected cooling and housing type is accessible and can be used to produce accurate estimations of the EM cost to be used in comparisons, optimizations and analysis of larger systems. The main objective of this model is to help designers understand the manufacturing implications of their decisions and vice versa, help manufacturing engineers to understand the performance implications that different manufacturing techniques have on the EM, as it is shown later in this section.

In a similar approach as the one taken for the development of the cost model for PECs, two separated and yet tightly related sections can be identified in the presented cost model for EM. The first section consists of the definition of all materials and major geometrical characteristics of the EM while the second part deals with identifying the optimal set of manufacturing processes required to produce the predefined EM design. Although the process might look sequential, in the sense that the first part of the model produces an EM design and the second part analyzes the required manufacturing process in order to produce it, depending of the type of study that is being undertaken this might not be the case, since the use of some manufacturing processes imposes constraints on the EM geometry and material selection. For example, some winding techniques may result in higher or lower fill factors which in turn changes the nominal current loading of the EM. In this work, the first section of the model (geometry and materials) is developed while the second one (manufacturing) is presented in [76].

Since the developed model is intended to be used in the optimization and analysis of larger systems, it is important that it provides a fast execution and an automated transfer of information between the design and manufacturing parts of the model. Therefore, all geometrical parameters of the EM design that are relevant for either the selection of manufacturing processes or the definition of cycle times and required investments in tools and

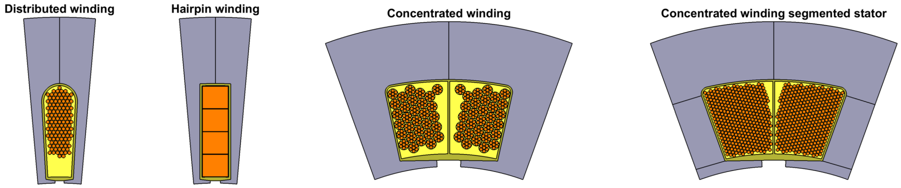

Figure 3.22: Slot filling for the four winding layouts, distributed, hairpin, concentrated needle and concentrated segmented winding.

fixtures need to be easily transferred between the two parts of the model. Moreover, information coming from the sizing models of other components can provide valuable inputs for the EM cost model. For example, in a system where the EM operates in conjunction with a MT, the gear ratio of the first mesh and the selected helix angle are important to determine the correct sizing of the bearings in the EM. Additionally, the desired production volumes have a significant impact on the selection of manufacturing processes and the amortization of the different investments; affecting in this way the overall cost of the EM.

3.2.6 Study on performance and manufacturability tradeoffs of different EM designs

Throughout the literature a variety of novel EM designs, cooling concepts, materials and alternative manufacturing techniques can be identified. However, objective comparisons that quantify the performance and cost implications of such designs are scarce. In this context, this section presents a short investigation on how different winding technologies affect both the performance and cost of an EM. The complete study can be found in [84]. The winding configurations under consideration are: (a) pulled winding using magnet wire, (b) hairpin winding, (c) needle-wound fractional slot concentrated winding (FSCW) and (d) FSCW with a fully segmented stator (refer to Fig. 3.22). Moreover, for both pulled and hairpin windings the impact of segmentation of the stator core is also analyzed. As the scope of this study is limited to compare the tradeoffs between different winding technologies, all EMs are assumed to have the same rotor geometry. Moreover, the stator geometry of the different EMs is only slightly modified in order to better suit the specific winding and to preserve the achievable copper area inside the slots.

The performance of each one of the six EM designs is characterized using the procedure presented in section 3.2.1. The nominal current density is estimated by means of 2D FE heat transfer simulations and it is assumed that all machines have the same forced cooling conditions (heat transfer coefficient = 600 $W/(m^2K)$ and To = $80^\circ C$). Magnetostatic 2D FE simulations are performed at different rotor positions and current combinations to estimate the torque, fluxes and losses. This data is post-processed in order to extract the torque vs speed characteristics of the machine, its efficiency maps and other relevant performance metrics.

Similarly, the manufacturing cost of the different designs is estimated following the procedure presented in section 3.2.5 and fully explained in [76]. By the combination of performance and production models, it is possible to develop a better understanding on the implications of different designs and manufacturing techniques.

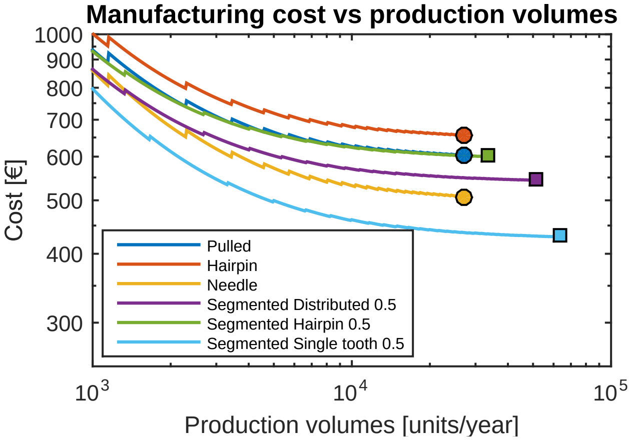

Figure 3.23: Electrical machine cost at different production volumes.

For example, Fig. 3.23 shows the estimated manufacturing cost for the different EM designs. In this figure it is possible to observe that stator segmentation yields a significant cost reduction in all cases, especially for the single tooth stator with concentrated windings. However, the lower cost of the segmented designs comes at the expense of a drop in performance. Figure 3.24 presents the estimated efficiency maps for the different EMs under consideration, accounting only for iron and copper losses (ac effects in the windings, windage, friction and magnet losses are neglected in this figure). It can be seen that for non-segmented stators, replacing the traditional pulled windings for hairpins significantly increases the fill factor, which in consequence increases the maximum produced torque and power (first and second column in Fig. 3.24) at the expense of a more complex and costly manufacturing (as illustrated in Fig. 3.23). On the other hand, a six pole machine is not the best selection for a performance comparison between distributed and concentrated windings as the combination of slot/poles for the concentrated winding version is limited to one (0.5 slots per pole and phase) yielding a low winding factor [85] and extremely large slots. This further reduces the allowable electric loading as the thermal resistance between the hotspot and the cooling medium increases with the slot size. The combination of these two effects causes a significant drop in torque and power for this machine type when compared to the other two.

Moreover, segmenting the stator introduces physical airgaps in between the different seg-

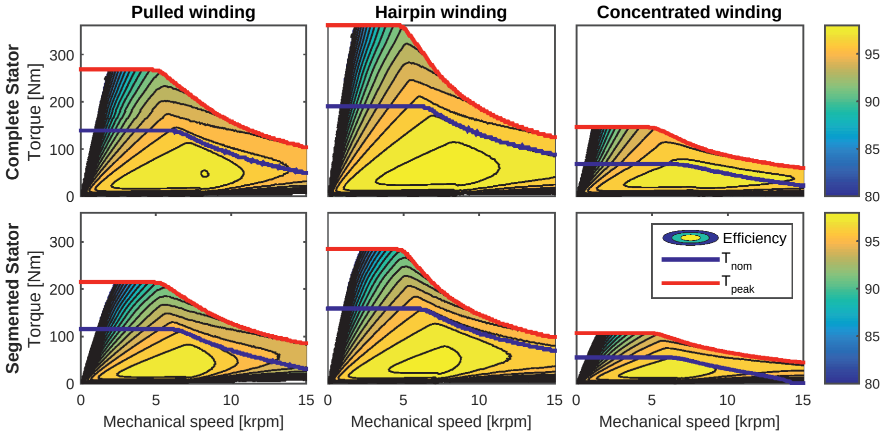

Figure 3.24: Efficiency maps for the six machine designs, including nominal and overloading torque curves.

ments (assumed in this study to be 0.1 mm in accordance with standard manufacturing tolerances [86]) that increase the reluctance of the magnetic path, reducing the flux linkage and therefore the torque/power for the same rotor and stator geometry. This can clearly be seen when comparing the first and second row of Fig. 3.24.

Another interesting aspect is the effect of the selected winding type on the frequency dependent copper losses of the machine. Figure 3.25 shows how the ac resistance increases with frequency for the four different winding types considered in this study assuming no axial transposition of the strands. It can be observed, that hairpin windings are subject to a more significant increase in the ac resistance, mainly due to the fact that they are made of a single thicker copper conductor per turn. The pulled windings and concentrated windings without segmentation have a lower increase in the ac-resistance compared to the values presented in Fig. 3.25 as random or intentional transposition of the strands is likely to occur and feasible to implement.

Several lessons can be learned from this short study. The first one, and arguably the most important one, is the need to connect traditional EM design with a detailed analysis of production systems. In order to assess the cost effectiveness of a given EM design it is necessary to understand how that EM could be produced at relevant volumes. Different manufacturing processes impose constraints in the design of the EM that could have a large impact in both its performance and cost. Moreover, although all the EMs in this study have a very similar material cost, their production cost varies significantly. This point out the importance of considering the cost incurred during manufacturing when assessing the cost effectiveness of a design.

The second lesson that can be extracted from this study is that stator segmentation is an

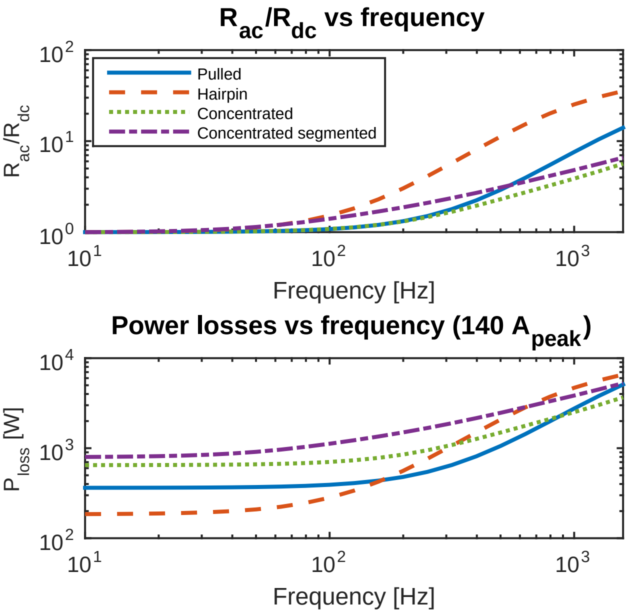

Figure 3.25: Relative AC/DC losses for the four winding types (top) and power losses at 140 A_{peak} (bottom) over frequency.

interesting alternative to reduce the material waste during production, simplify the winding process and reduce the overall cost of the machine. However, it is necessary to mitigate the loss of performance due to segmentation. In this context, several strategies can be explored, for example, the EM should be designed and optimized considering segmentation from the beginning, unlike this work where an existing design is adapted. Another strategy is to improve the manufacturing techniques in order to reduce the airgaps introduced between stator segments (smaller airgaps than the ones used in this work have been reported in the literature [87]). Additionally, it is worth studying the impact that different segmentation arrangements have in the performance of the EMs, as preliminary studies report promising results [76].

Finally, the EM design selected as base for this study is not well suited for concentrated windings, as it has a low number of poles which leads to a low winding factor. However, an independently optimized machine using concentrated windings can offer a comparable (and some times even superior) performance to that of an optimized design with distributed windings as shown in the literature. In this context, the results from this work point out that if a similar performance can be achieved with similar volume and material cost, the manufacturing cost of the concentrated winding machine can be expected to be significantly lower than its distributed winding counterpart.

3.3 Transmission

In many applications EMs benefit from operating at higher speeds and lower torques, since this allows to reduce their size and cost. In order to adjust the torque/speed of the EM to the required values, different types of MT can be used. These additional components incur their own weight and cost to the system, and it has to be considered together with that of the EM and PEC (if applicable) in order to find an optimal system solution. Therefore, data on the transmission size, weight and cost is necessary in order to determine the optimal system configuration that fulfills all the performance requirements and packing constraints of the application.

As it is the case with EMs and PECs, commercial off the shelf components only comprise a small section of the total possible transmission solutions. If these are the only components taken into consideration there is a chance that the selected solution can greatly differ from the theoretical optimum. Additionally, any conclusions regarding the tradeoffs between the transmission components and the rest of the system in terms of cost and packing would be, in the best case, incomplete.

For these reasons, a method to estimate the size and cost of different transmissions layouts based on a reduced number of performance characteristics could improve significantly the outcome of a system optimization (e.g. of an electric powertrain). Such method should required a short execution time and disregard combinations that do not comply with the packing/weight constraints. In this way, interesting configurations that are worth studying further can be identified.

This section presents a methodology to quickly estimate the size, weight and cost of several transmission types, especially those that could be used in a hybrid or full electric powertrain. The first step of this methodology is to perform a rough sizing of all the gears in the transmission following the standards from the American Gear Manufacturing Association (AGMA) in order to ensure that the actual bending and contact stresses are below the allowable levels of the materials. The next stage is to estimate the dimensions of shafts, bearings and shifting mechanisms and finally the cost is calculated based on data collected from manufacturers.

3.3.1 Stress analysis on a gear

The main challenge when designing gears is to select the right dimensions and materials in order for the gear to carry the required load, under the conditions dictated by the application and during the expected life. If a gear is undersized, the risk of failure increases. Depending on the degree on which the gear is being undersized different types of failures can occur, for extremes cases when the size of the gear is significantly smaller than the required one, the gear can suddenly break under the applied load. This is likely to happen during early stages of the gear's life. In other cases, when the gear is not so severely undersized, fatigue failures tend to occur earlier than its expected end of life, meaning that the gear would have a shorter life than the application requires. On the other hand, if the gear is oversized, the main drawbacks are presented in the form of higher cost, weight and required space.

In consequence, the design of a gear mesh consists in finding the right balance between size (volume/cost), load carrying capabilities and expected life. In order to achieve such balance, a thorough analysis of the stresses that the gear is subject to needs to be carried out, and compensation factors need to be added in order to account for operating conditions, reliability, manufacturing and mounting defects and expected life. Two major sources of fatigue related failures are the bending and contact stresses [88]. In this section, the derivation of the formulas used to calculate those stresses is presented and the application dependent factors are introduced following the standards developed by AGMA.

The analysis of the stresses in gears is outside the core expertise of the division of Industrial Electrical Engineering and Automation institution, where this work has been carried out. For this reason, the equations used to estimate the most relevant stresses that gears are subject to are derived and explained with a higher level of detail than used in previous sections, when dealing with electrical machines and power converters.

Bending Stress:

One of the most common causes of failure on the root of the gear's tooth is the fatigue produced by bending stresses that are higher than the endurance limit of the material. This failure mode is characterized by the progressive forming and propagation of cracks in the base of the tooth and can end up with the tooth completely breaking away from the gear.

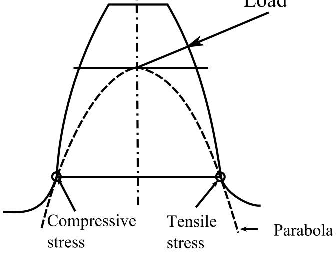

Figure 3.26: Iso-stress parabola inside the gear profile. Figure inspired in [89].

The gear's tooth can be assumed to behave like a cantilever beam, with the loaded side being subject to tensile stress and the opposite side to compressive stress. Equation (3.35) describes the stress of a cantilever beam when a force W is applied on a beam of length l, width F and thickness t. However, in order to approximate the analysis of the bending stress in a gear's tooth to that of a cantilever beam, a parabola of uniform strength is placed inside the tooth as shown in Fig. 3.26 [90]. This parabola, is tangent to the tooth profile on the root fillet, which makes the stress of the parabola and tooth equal in this point.

$$s_t = \frac{6Wl}{Ft^2} \tag{3.35}$$

If the parameters of (3.35) are modified in order to use it to analyze the stresses in the gear's root, l is now the distance between root of the tooth and the point where the load line intersects the center of the tooth, F is the face width of the gear and t is the thickness of the tooth. However, it is convenient to rewrite this formula in terms of quantities that are commonly used such as the tooth form factor and module. For this reason, the distance x is introduced in Fig. 3.27 and using similar triangles it can be written as a function of known quantities as $x = t^2/4l$ [90].

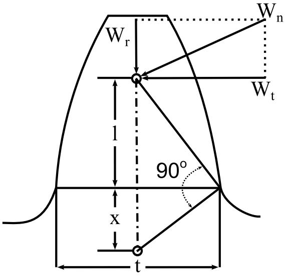

Figure 3.27: Determination of the form dependent parameter x. Figure inspired in [89].

Equation (3.36) shows the result of introducing the length x into (3.35). At this point, it is clear that x is only determined by the shape of the tooth and therefore, it allows the introduction of a dimensionless variable called the Lewis' form factor [89] as $Y = 2x/3m$ where m is the module of the tooth. This leads to the Lewis formula presented in (3.37).

$$s_t = \frac{W_t}{F(2x/3)} \tag{3.36}$$

$$s_t = \frac{W_t}{FmY} \tag{3.37}$$

The formula presented in (3.37) estimates the stress under specific conditions and might results in an over estimation of the gear loading capabilities. For example: the force is expected to act on the tip of the cantilever parabola which is not necessarily the worst load condition for those cases when several teeth are sharing the load at a given point. The stress is assumed to be evenly distributed in every point of the cross section of the iso-stress parabola, especially at the root of the tooth, neglecting in this way the stress concentration on the root fillet. The load is presumed to be constant and temporal overloading of the gear is not being accounted for. The effect of the temperature on the mechanical properties of the gear's material is not taken into consideration either and manufacturing defects are being neglected among other issues. For the exposed reasons, AGMA introduces a series of scaling factors [91, 92]. The recommended formula to estimate the bending stress acting on a gear, is defined according to AGMA in (3.38), and guidance on the selection of the aforementioned scaling factors can be found in [91, 93].

$$s_t = \frac{W_t}{FmY_j} K_o K_v K_s K_m K_b \tag{3.38}$$

Where W_t is the tangential force, F and m are the face width and module of the gear, Y_j is the geometry factor for bending strength (which differs from the Lewis' form factor) and K_o, K_v, K_s, K_m and K_b are the overloading, dynamic, size, load distribution and rim thickness factors respectively. Once the corrected bending stress on the gear is estimated, it is necessary to ensure that it is below the maximum allowable limit. To do so, the Eq (3.39) needs to be satisfied.

$$s_t \leq \frac{S_{at}}{S_f} \frac{Y_n}{K_t K_r} \tag{3.39}$$

Where S_f is the safety factor, the stress cycle factor is denoted by Y_n, K_t represents the temperature factor and K_r the reliability factor.

Contact Stress:

The compressive fatigue in the face of the gear can cause the formation of small holes or craters on the surface of the tooth (this phenomenon is called pitting). This fatigue is the result of the accumulation of compressive stresses due to the normal loads applied to the surface of the tooth (usually from the contact with another gear's tooth) [92]. Depending on the size of the holes that are formed, the gear can present micro or macro pitting, the last one being the most destructive.

A common starting point to analyze the stress on the surface of a gear tooth are Hertz's equations [89]. Following Hertz's work, the width of the contact band between two cylinders with parallel axes that are forced against each other as shown in Fig. 3.28 can be described by (3.40).

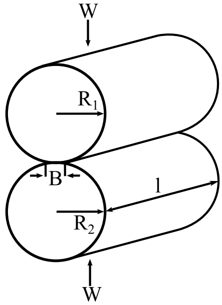

Figure 3.28: Determination of the width of the contact band when two cylinders are pressed together. Figure inspired in [89].

$$B = \sqrt{\frac{16W(K_1 + K_2)R_1R_2}{L(R_1 + R_2)}} \tag{3.40}$$

The constants K_1 and K_2 present in (3.40) depend on the Poisson's ratios (v) and modulus of elasticity (E) of the materials and are defined according to (3.41).

$$K_1 = \frac{1 - v_1^2}{\pi E_1} \tag{3.41}$$

Once the width of the contact band is known, the contact stress can be calculated as shown in (3.42).

$$s_c = \frac{4W}{\pi LB} \tag{3.42}$$

When two teeth are in contact, a similar deformation is produced on their faces and Hertz formula can be used to estimate the width of the contact band. Figure 3.29 shows how the teeth can be approximated to two cylinders in contact.

Substituting (3.42) in (3.40) and replacing the force W for $W_t/cos\phi$, the stress on the face of the gear can be estimated as presented in (3.43). It should be noted that in contrast with

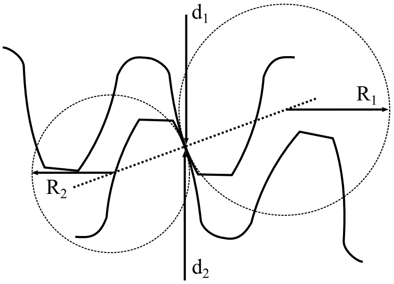

Figure 3.29: Deformation on the gear's tooth.

the bending stress the contact stress in proportional to the root square of the tangent force.

$$s_c = \sqrt{\frac{0.7}{(1/E_1 + 1/E_2) sin\phi cos\phi}} \sqrt{\frac{W_t}{Fd} \frac{m_g + 1}{m_g}} \tag{3.43}$$

In order to simplify the previous expression, the following variables are introduced:

$$C_p = \sqrt{\frac{1}{\pi^2 (K_1 + K_2)}} \tag{3.44}$$

$$I = \frac{cos\phi sin\phi}{2} \frac{m_g}{m_g + 1} \frac{F_{min}}{F} \tag{3.45}$$

Note that C_p is a constant that depends on the gears' materials, while I depends on the geometry of the teeth. Combining (3.44) and (3.45) in (3.43) a simplified equation can be written as shown in (3.46).

$$s_c = C_p \sqrt{\frac{W_t}{Fd} \frac{1}{I}} \tag{3.46}$$

In a similar way as the effective load to calculate the bending stress is obtained after applying several application dependent correction factors to the actual load, some scaling factors are included in (3.46) to account for the real conditions under which the gear is expected to operate. This results in the AGMA equation for contact stress presented in (3.47) [91].

$$s_c = C_p \sqrt{\frac{W_t}{Fd} \frac{K_o K_v K_s K_m C_f}{I}} \tag{3.47}$$

After calculating the corrected contact stress on the surface of the gear, it is necessary to ensure that it is below the maximum allowable limit. To do so, the inequality presented in (3.48) has to be fulfilled.

$$s_c \leq s_{ac} \frac{Z_n C_h}{S_h K_t K_r} \tag{3.48}$$

However, numerous industries prefer to rate the gears according the contact load factor K, which is introduced in (3.49) [94].

$$K = \frac{W_t}{Fd} \frac{m_g + 1}{m_g} = \frac{2T}{Fd^2} \frac{m_g + 1}{m_g} \tag{3.49}$$

In a similar fashion that it is possible to establish a maximum allowable contact stress, it is possible to define a maximum allowable contact load factor as shown in (3.50). This factor is widely used to quickly estimate the required dimensions of the gears for a given load.

$$K_{ac} = \frac{I}{K_o K_v K_s K_m C_f} \left(\frac{S_{ac}}{C_p} \frac{Z_n C_h}{S_h K_t K_r} \right)^2 \tag{3.50}$$

3.3.2 Gear mesh sizing

In this section, the methodology used to determine the required dimensions of a gear, based on the loads it is expected to withstand, is described. This sizing methodology is used to determine the dimensions of all the gears in the transmission once some input parameters have been defined.

Using the equations presented in previous sections to calculate the contact and bending stress of the gears, it is possible to estimate the minimum gear size needed in order to fulfill the requirements of the application. First the nominal loading condition and the gear's material are defined, the next step consists in determining the required volume of each gear in order to withstand the contact stress. Next, the face width and diameter of the gears are extracted from the volume factor using a predefined aspect ratio for the pinion gear (m_{fd}). The following step is to calculate the number of teeth for the pinion gear that results in a gear ratio closest to the required one and that has a sufficiently high safety factor for bending stress. The achieved gear ratio is computed based on the number of teeth in both gears. Finally the specifications for each gear are output together with the estimated safety factors. This procedure is depicted in Fig. 3.30 and every step is explained in detail in the following subsections.

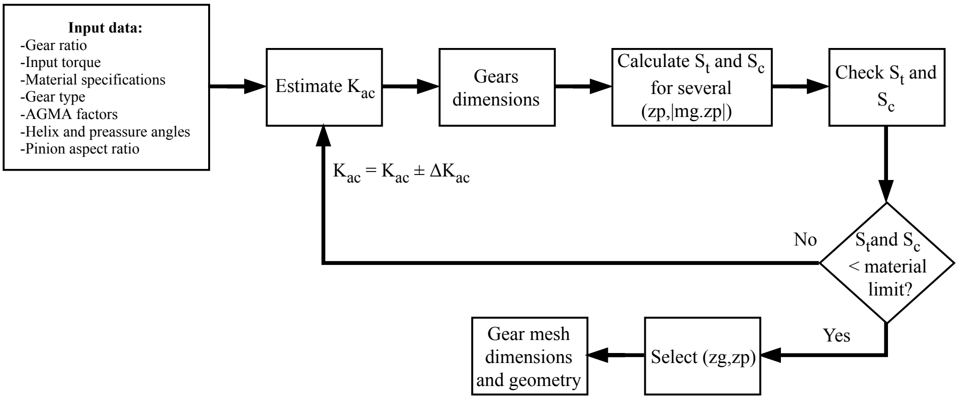

Figure 3.30: Gear mesh design procedure.

Volume Factor

Using the maximum allowable contact load factor it is possible to estimate the volume factor of the gear (Fd^2). If Eq (3.49) is rewritten and K is replaced by K_{ac}, the volume factor can be obtained as shown in (3.51).

$$Fd_p^2 = \frac{2T}{K_{ac}} \frac{m_g + 1}{m_g} \tag{3.51}$$

From (3.51) it is possible to conclude that the volume factor of the gear is proportional to the transmitted torque and inversely proportional to the maximum allowable contact load factor, meaning that gears made of a harder material or with a shorter expected life are lighter even if they are rated for the same load. Note also that the sub index p is added to the diameter in the previous equation since it refers to the pinion gear. Considering that the ratio between the pinion and mating gear diameter is given by the gear ratio ($d_g = m_g d_p$), it is possible to calculate also the volume of the factor for the gear as shown in (3.52).

$$Fd_g^2 = Fd_p^2 m_g^2 = \frac{2T}{K_{ac}}(m_g + 1)(m_g) \tag{3.52}$$

Now for the simplest gear arrangement possible (a pinion and a mating gear), the total volume factor is presented in (3.53).

$$\Sigma Fd^2 = Fd_p^2 + Fd_g^2 = (m_g^2 + 1)Fd_p^2 = \frac{2T}{K_{ac}}(m_g^2 + m_g + 1 + 1/m_g) \tag{3.53}$$

If the gears are assumed to be full discs, their total volume can be calculated as shown in (3.54). As it is presented in upcoming sections the volume factor is used to estimate the preliminary dimensions of the different gears. Additionally, in more complex transmission layouts, the volume factor is also used to optimize the selection of the ratios in the different meshes.

$$V = V_p + V_g = \frac{\pi}{4}\Sigma Fd^2 \tag{3.54}$$

Dimensions

From the volume factor, the specific face width and diameter of each gear can be obtained if the aspect ratio of the pinion (m_{fd}) is preselected. Alternatively, if packing constraints are put in place, the aspect ratio of the pinion gear can be optimized as discussed in following sections.

$$\begin{gathered} d_p = \sqrt[3]{Fd_p^2 \frac{1}{m_{fd}}} = \sqrt[3]{\frac{2T}{K}\frac{m_g+1}{m_g}\frac{1}{m_{fd}}} \\ F = m_{fd} d_p \end{gathered} \tag{3.55}$$

The aspect ratio can be varied within certain limits in order to fulfill packing constraints. According to the literature, in conventional automotive transmissions the aspect ratio is in the interval between 0.3 and 0.8, and the typical value for the first gear is around 0.65. As a starting point, the aspect ratio for the pinion gear can be selected as shown in (3.56) [92].

$$m_{fd} = \frac{F}{d_p} = \frac{m_g}{m_g + 1} \tag{3.56}$$

Number of teeth

As it is explained in the previous section, the bending stress sets the condition to select the appropriate number of teeth. the larger the number of teeth, the lower the module and, therefore, the higher the bending stress in the root of the tooth. However, depending on the selected pressure and helix angles, there is a minimum recommended number of teeth, so that interference or undercut are not produced [89]. Furthermore, there are practical benefits of having a large number of teeth such as smoother operation of the gear mesh. The relationship between the number of teeth and the bending stress is presented in (3.38) and (3.39), which can be rewritten as:

$$S_{at} \geq \frac{W_t}{b}\frac{S_f}{m}\frac{K_o K_s K_v K_m K_b K_r K_t}{Y_j Y_n} = \frac{W_t}{b}\frac{z_p S_f}{d_p}\frac{K_o K_s K_v K_m K_b K_r K_t}{Y_j Y_n} \tag{3.57}$$

With this equations it is possible to find all the viable number of teeth that fulfill the interference and bending stress conditions. If it is not possible to find a number of teeth that fulfills both the bending stress and interference conditions, the dimensions are adjusted and the process is repeated as shown in Fig. 3.30.

Achieved gear ratio

With the set of possible number of teeth in the pinion, it is possible to calculate the required number of teeth in the mating gear. This number has to be rounded to the closest integer, which causes a small discrepancy between the achieved gear ratio and the intended one. The combination of z_p and z_g that provides the lowest error between the achieved and expected gear ratio is selected.

3.3.3 Transmission sizing

There are limitless combinations of transmission layouts that could, for a given application, fulfil all the requirements. Each layout brings along advantages and drawbacks that can make it better or worse suited when compared with the other candidates. For this reason, several relevant types of transmissions are included in the present sizing and cost model. In this work the transmission layouts are divided in two major groups, the first group is composed by those transmissions that, regardless of the number of gear stages and gear meshes, have a constant gear ratio between the input and output shaft. The second group contains transmissions where the gear ratio could be varied among a discrete number of alternatives. This classification together with the specific layouts included in this work can be observed in Fig. 3.31.

This section describes the modifications on the volume factor used to determine the optimal split between meshes for each transmission layout. Once the ratio of each mesh is known, an initial estimation of the aspect ratio of the pinion gear is made. If packing constraints are in place, this estimation is optimized in order to fulfill those constraints. On the other hand, in the absence of packing constraints a fixed value that can be either predefined or selected according to recommended values in the literature [92] is used. For a given aspect ratio, the design of each gear mesh, including the definition of dimensions and number of teeth is done as explained in section 3.3.2. With the gears dimensions defined, it is possible then to estimate a rough size of the housing as the minimum envelope needed to enclose all gears. Additionally, the shaft and bearing can also be roughly designed/selected based on the gear dimensions and loads. The overall procedure for sizing a MT is shown in Fig. 3.32.

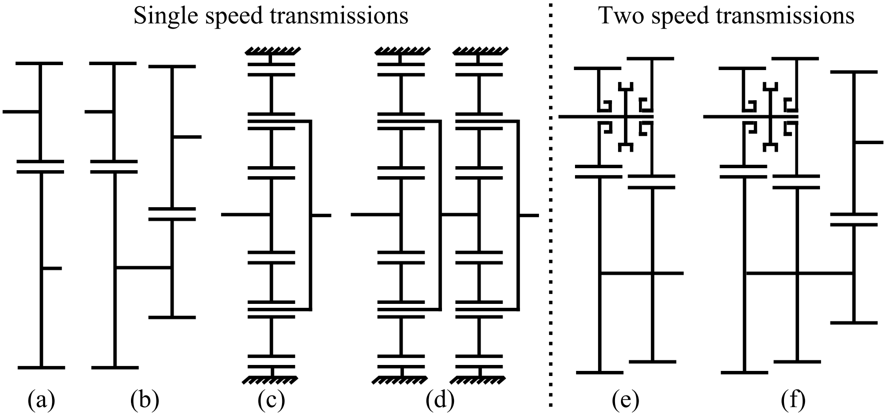

Figure 3.31: PLACE HOLDER Transmission layouts included in the present work: (a) offset gear (b) double stage offset gear (c) planetary gear (d) double stage planetary gear (e) two speed transmission (f) two speed transmission without output reduction gear.

Single stage offset gears

This is the simplest transmission layout, it is composed of a pinion and a mating gear. It serves as the base for many other layouts. The equation for the volume factor is shown in the previous section (3.53). This configuration is recommended for gear ratios below $6 : 1$, for higher ratios the use of a second stage can be beneficial [92].

Double stage offset gears

It consists of two sets of gear meshes and it allows to achieve higher gear ratios than a single stage configuration at the expense of a lower efficiency, additional bearings and shafts. The same total gear ratio could be achieved with countless combinations on the specific gear ratio of each stage. However, it results advantageous to minimize the total weight or volume of the gear set. If the material and manufacturing quality are assumed to be the same for all the gears, the optimal gear ratio of each mesh can be found by minimizing (3.58), where m_g is the total gear ratio of the transmission and m_{g1} is the gear ratio of the first stage. Once the optimal gear ratio for each stage is known the gears are sized using the same procedure as for a single stage offset gear.

Note that the first term in the objective function of (3.58) is the same as (3.53) while the second one is multiplied by the gear ratio of the first mesh (m_{g1}) due to the higher nominal torque in the second mesh with respect to the first one and m_g is replaced by ${}^{m_g}/_{m_{g1}}$ which is the actual ratio of the second stage.

$$\begin{aligned} Minimize : f = & \; (m_{g1}^2 + 1)(1 + {}^1/_{m_{g1}}) + m_{g1}(({}^{m_g}/_{m_{g1}})^2 + 1)(1 + {}^1/_{({}^{m_g}/_{m_{g1}})}) \\ s.t : m_{g1} & > 1 \\ m_g & > 1 \\ {}^{m_g}/_{m_{g1}} & > 1 \end{aligned} \tag{3.58}$$

After this procedure is carried out, the result is compared with a single stage offset gear for the same reduction, and the lightest of both is selected.

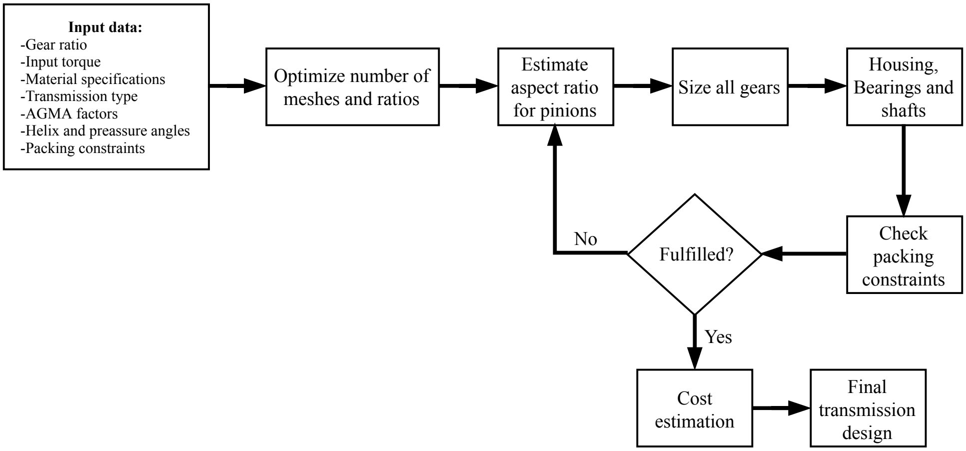

Figure 3.32: Transmission design Procedure.

Single stage planetary gears

Planetary gears are widely used due to their ability to carry high loads in a very compact space and the possibility of having input and output shaft concentrically.

An expression for the volume factor of a planetary gear arrangement can be written in a similar way as it is done for other gear arrangements as the sum of all the volume factors of the gears. Based on the maximum allowable contact load factor, the volume factor of the sun gear is presented in (3.59). Note that the total torque is divided by the constant b that denotes the number of planets, since it is assumed that the load is evenly distributed among all the contact points. This is one of the reasons why the planetary gear arrangements present such a high load carrying capabilities. In this expression m_{ps} is the ratio between the sun and the planet diameter, not the total gear ratio of the transmission. However, they are related according to $m_g = 2(m_{ps} + 1)$.

$$Fd_s^2 = \frac{2T}{K_{ac}b}\frac{m_{ps}+1}{m_{ps}} \tag{3.59}$$

The next step is to calculate the volume factor for the planets and ring gear, which are given by (3.60) and (3.61) respectively. In the last equation an experience-based factor of 0.4 is used in order to account for the fact that the ring gear is not a solid disc [94]. Once all the volume factors are known, it is possible to determine the specific dimension of each gear using the same sizing methodology previously presented.

$$bFd_p^2 = bFd_s^2 m_{ps}^2 = \frac{2T}{K_{ac}}(m_{ps}+1)(m_{ps}) \tag{3.60}$$

$$Fd_r^2 = Fd_s^2 \frac{d_r}{d_s}^2 (0.4) = Fd_s^2(2m_{ps}+1)(0.4) = \frac{2T}{K_{ac}b}\frac{m_{ps}+1}{m_{ps}}(2m_{ps}+1)(0.4) \tag{3.61}$$

$$\Sigma Fd^2 = \frac{2T}{K_{ac}}\left(\frac{1}{b}+\frac{1}{bm_{ps}}+m_{ps}+m_{ps}^2+0.4\frac{(m_g-1)^2}{bm_{os}}+0.4\frac{(m_g-1)^2}{b}\right) \tag{3.62}$$

Finally the dimensions and weight of the carrier are estimated once the number of planets, diameters and face width of all the gears are known. Additionally, a constraint on the viable number of teeth for the sun is implemented in order to ensure a symmetric placement of the planet gears.

Double stage planetary gears

If several planetary gears are meant to be used in series, the gear ratio of each of them needs to be selected so the overall volume factor is minimized for a given gear ratio. The minimization problem for a double stage planetary gear is shown in (3.63). Once the gear ratio of each stage is selected, the process continues by sizing them independently.

$$
\begin{aligned}
Minimize: f = {} & \Sigma F d_1^2(b_1, m_g 1) + m_{g1} \Sigma F d_2^2(b_2, m_g 2) \\
s.t: m_{g1} & > 3 \\
m_{g2} & = \frac{m_g}{m_{g1}} \\
m_g & > 9
\end{aligned}
\tag{3.63}
$$

Two speed gearbox

The selected topology for a two speed gearbox is presented in Fig. 3.31. As in the previous cases the selection of the gear ratio in each stage is done with the aim of minimizing the overall weight of the transmission. Equation (3.64) defines the optimization problem. m_{g0} stands for the gear ratio of the final reduction step, and the sub-indexes 1 and 2 are the total gear ratio of the transmission in first and second gear. Once the gear ratios are defined, each gear mesh is sized in the same way as a single stage offset gear, later the size and cost of the shifting mechanism is estimated based on the torque of the shaft where it is located. It is worth noticing that for low gear ratios, the final reduction gear can be spared, and the volume factor of such configuration would be similar to (3.64) but without the last term and setting m_{g0} equal to 1 in the first two terms.

$$
\begin{aligned}
Minimize: f = {} & (1 + \frac{m_{g0}}{m_{g1}} + \frac{m_{g1}}{m_{g0}} + (\frac{m_{g1}}{m_{g0}})^2) + \\
& (1 + \frac{m_{g0}}{m_{g2}} + \frac{m_{g2}}{m_{g0}} + (\frac{m_{g2}}{m_{g0}})^2) + \\
& \frac{m_{g1}}{m_{g0}}(1 + \frac{1}{m_{g0}} + m_{g0} + m_{g0}^2) \\
& m_{g0} > 1 \\
& m_{g1} > 1 \\
& m_{g2} > 1 \\
& m_{g1} > m_{g2}
\end{aligned}
\tag{3.64}
$$

3.3.4 Cost estimation

The first step in the calculation of the cost of a MT consists of an estimation of the cost of each one of its major components. This includes material, manufacturing, quality assurance (at a component level) and overhead costs directly related to that specific component. The category of components encompasses all the gears, bearings, shafts, shifting mechanisms and housings. The cost figures used in this work are obtained directly from suppliers and volume dependent relationships are included. In this way, the tool is able to estimate the cost of the transmission for different production volumes. Since the used cost figures are of sensitive nature to the companies that aided in the development of this model they cannot be presented in this work. However, in order to illustrate some factors that have a significant impact on the gear's cost, Fig. 3.33 shows the cost per unit of mass for different types of gears. The lowest specific cost is that of a spur gear (shown in black). It can be seen that heavier gears are relatively cheaper although they remain more expensive in absolute value. Moreover, a helical gear is slightly more expensive (somewhere between $4 - 35\%$) than a spur gear of the same weight. Finally, the addition of dog-teeth to a gear results in a significant rise in cost (somewhere between $60 - 120\%$). In both cases, the difference in cost respect to a spur gear is mainly due to an increase in the manufacturing complexity of the gear.

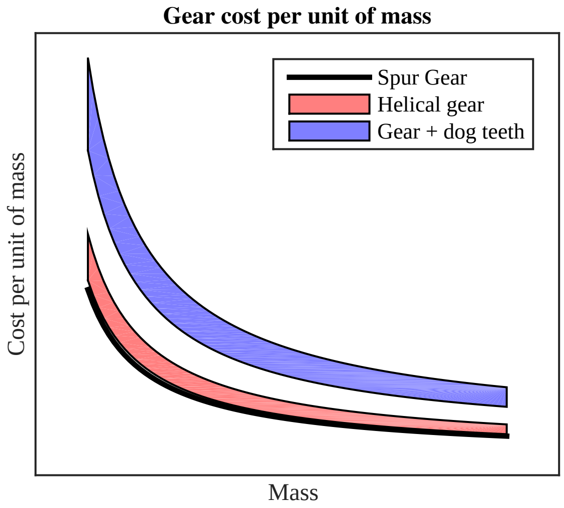

Figure 3.33: Representation of the specific gear cost.

The next step is to include a multiplication factor to account for the cost of assembly and quality assurance of the gearbox as a whole ($1/k_{as}$). The cost of a MT can be described by (3.65), where M is the component mass, \$ is the specific cost of the selected component type, the sub-indexes g, h, s, b and mi correspond to gears, housing, shafts, bearings and miscellaneous costs (such as actuators). The desired number of units is represented by N_{units} while the original number of units at which the cost figures are extracted is No_{units}. The learning ratio is denoted by R_c. The implemented costing methodology allows to understand which components are driving the cost of the gearbox and how they are affected by changes in the design or specifications. This information combined with the cost models developed for the remaining components of the electric powertrain allow to minimize the total cost of the system.

$$\begin{aligned} cost_T = &\Bigg[\left(\sum Mi_g\$_g(Mi_g) + M_h\$_h(M_h) + \sum Mi_s\$_s(Mi_s)\right)\left(\frac{N_{units}}{No_{units}}\right)^{log(Rc)} \\ &+ \sum \$i_b + \sum \$i_{mi}\Bigg]\left(\frac{1}{k_{as}}\right) \end{aligned} \tag{3.65}$$

3.3.5 Model validation and packing studies

In order to verify that the described model can be used to obtain a correct estimation of the required gear dimensions, a number of gear meshes is designed for different input torques and gear ratios, and the resulting dimensions are validated using specialized software for gear design [95]. Figure 3.34 shows the estimated weight of a gear mesh (excluding housings, shafts or bearings) for several combinations of input torque and gear ratio, the blue markers represent the designs that are selected for further analysis.

Table 3.7 presents the obtained safety factors for bending and contact stress both for dynamic and static operation. As expected, the obtained static safety factors are above the dynamic ones as the later represent a worst-case scenario for dimensioning the gears. More important is the fact that for all designs the safety factors for bending and contact stress are above 1.3 and 1.1 respectively. These are considered reasonable values for the application according to experienced gear designers.

The model has been further validated by expert gear designers during the realization of various packaging studies carried out in cooperation with Swedish Powertrain. Due to its fast execution, the previously described model is able to quickly optimize the number of meshes, gears dimensions and the overall layout of the transmission to fulfill certain packing constraints and to achieve the desired gear ratio(s) and output torque/speed profiles.

As an example Fig. 3.35a shows a preliminary powertrain design for a low-floor bus application aiming to provide some additional functionalities other than traction, such as charging, torque vectoring and to be compatible with steering. This study is carried out early in the

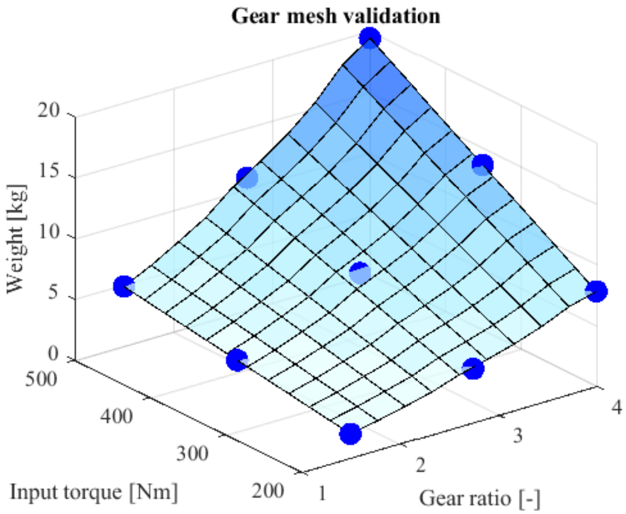

Figure 3.34: Gear mesh weight for several combinations of input torque and gear ratio.

design process, to assess the feasibility of the solution and whether or not it would be worth investigating it further. Therefore, rather than optimizing the EMs, a known design able to fulfill the torque and power demands is used [96]. Due to the low floor requirements, long axial length of the selected machines and steering demands, a long and slender powertrain with the EMs far from the center of the wheels is determined to be a suitable candidate.

After a detailed analysis of this powertrain concept it is observed that the required angle of the universal joints is higher than recommended by the manufacturer, which could reduce their expected life. Since packing constraints make it challenging to design the powertrain so that the output shafts are closer to the center line of the wheel, the model is used to investigate the possibility of adding a hub-reduction gear (as shown in Fig. 3.35b). This allows to lower the connection point to the wheel which reduces the angle of the propshafts. However, it complicates the overall design and increases the number of gear meshes of the powertrain.

Although the focus of these studies is on low-floor buses as they present a very challenging set of packing constraints, the powertrains under study are intended to be suitable for a variety of applications, some of which require them to operate in conjunction with an ICE in a parallel HEV configuration. The model is used to assess the feasibility of adding a differential in between the two branches of the transmission to serve as a connection point for the combustion engine, as shown in Fig. 3.35c. Finally, the same powertrain concept is re-designed to use axial flux machines instead (see Fig. 3.35d), this lowers the axial length and changes the torque/speed profile of the EMs which allows to reduce the required number of gear meshes.

Table 3.7: Validation of the design model

Gear ratio	Input torque	S_f bending		S_f conctact	
		dynamic	static	dynamic	static
1.5	200	1.41	3.83	1.26	2.1
	350	1.33	3.71	1.24	2.47
	500	1.35	3.9	1.27	2.08
2.75	200	1.41	4.21	1.3	2.14
	350	1.52	4.43	1.33	2.17
	500	1.63	4.63	1.36	2.23
4	200	1.47	4.08	1.33	2.18
	350	1.46	4.24	1.34	2.18
	500	1.54	4.63	1.36	2.23

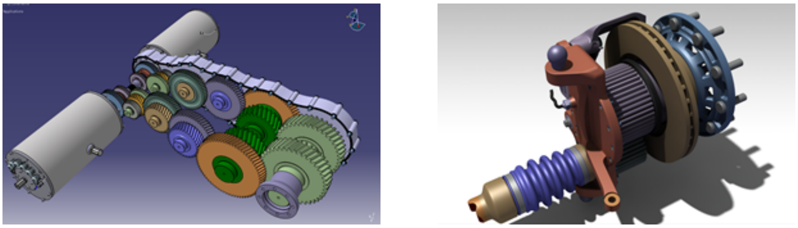

(a) Powertrain for low-floor bus

(b) Hub-reduction gear for low-floor bus

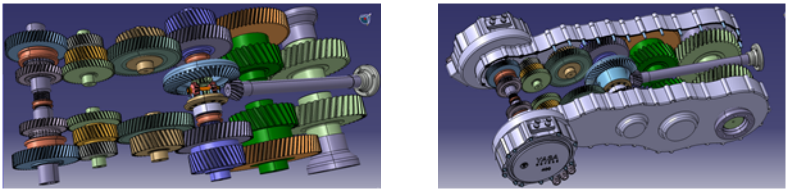

(c) Hybrid powertrain for low-floor bus/truck

(d) Hybrid powertrain for low-floor bus/truck using axial flux machines

Figure 3.35: Packing studies[3].

In all cases, once a final design was obtained it was verified both by means of specialized software for gear design [95] and experts in the field. From those verifications it is concluded that the presented model is sufficiently accurate to be used in the pre-design of electric powertrains as only minor modifications were needed.

---

[3] Illustrations and CAD models courtesy of Anders Göransson, Swedish Powertrain.

Chapter 4

Powertrain optimization

The optimization of an electric powertrain aims to provide a system design that is able to meet all performance and packaging requirements while minimizing e.g., the added cost and/or energy consumption of the vehicle. Moreover, the optimization process itself must have the following characteristics: (i) it must use components and system models with sufficient level of detail to capture all the relevant interactions between the different components; (ii) it has to provide results that can serve as a starting point for a final design; (iii) it should require a short set-up time and be computationally efficient to execute in order to reduce development times and associated costs; (iv) it has to be flexible, allowing the introduction of new technologies, components, topologies or system layouts as they emerge. Finally, (v) if cost minimization is a major objective of the optimization, then accurate cost models for the different components, based on a similar set of assumptions, need to be used in order to ensure that the cost-tradeoffs between the components are being correctly captured.

In the existing literature several efforts have been focused on addressing these challenges, mainly improving the modeling and scalability of the different components in the powertrain and proposing new optimization techniques. For example, a methodology to generate new EM designs by performing dimensional and number of turns scaling of a "base machine" is presented in [97]. Similarly, a set of scaling rules for permanent magnet machines is described in [98] and used in [99] together with a loss model for a PEC to perform a multi-objective optimization, aiming to reduce both the EM volume and the average losses over a driving cycle. This set of rules is also used in [100] to optimize the sizing of in-wheel EMs for traction applications. Another approach is to consider the impact of the dimensional scaling on the parameters of the equivalent circuit of an EM, as presented in [101]. These methodologies allow to quickly adjust the performance and efficiency characteristics of the scaled EM and are therefore valuable tools in powertrain simulations and optimizations.

On the other hand, efficiency maps for PEC are often used in powertrain simulations [102] as they present a good balance between accuracy and required computational time. This approach is easy to apply when the specific properties of the components in the converter are known. However, if the design of the PEC is to be included within the optimization of the powertrain, a rule-based approach [103] or an approach that relates the characteristics of the components to their physical size [58] can be applied.

Moreover, investigations of the impact of the mechanical transmission topology on the overall efficiency of the powertrain are carried out in [104]. Usually, if the transmission is included in the powertrain optimization, the focus is placed on selecting the correct gear ratio(s) and its cost, weight and size are considered by means of simple linear models [105, 106].

Finally, some attempts at integrating performance and cost models for EM, PEC and MT in the optimization of an electric powertrain are presented in [106–108]. However, details on how the different models are constructed are scarce.

This chapter outlines the integration of the sizing, performance and cost models presented in Chapter 3, in the optimization of an electric powertrain. As stated before, the objective is to find a balance between modeling the components with sufficient level of detail in order to capture all the relevant interactions among the different components, and keeping the required computational time at reasonable levels which allows the methodology to be a valuable tool in the early design phases of electric powertrains. An overview of the proposed optimization methodology is presented in Fig. 4.1. In the coming sections, the different steps in the optimization process are described. The material presented in this chapter is an extension of the work previously published in [109].

4.1 Input data

The first step in the optimization procedure is to define all relevant input data. This includes powertrain concepts to be evaluated, performance requirements, packing constraints, available cooling, and components specifications such as battery voltage, switching frequency and semiconductor technology for the PEC, gears' material, etc.

It could be argued that some of these parameters should be optimized rather than being pre-defined, and in principle there is nothing preventing the designer from including them in the optimization. However, increasing the number of variables to optimize significantly increases the computational time and thus reduces the usefulness of the developed optimization tool. Moreover, many of these parameters could be fine tuned once the main

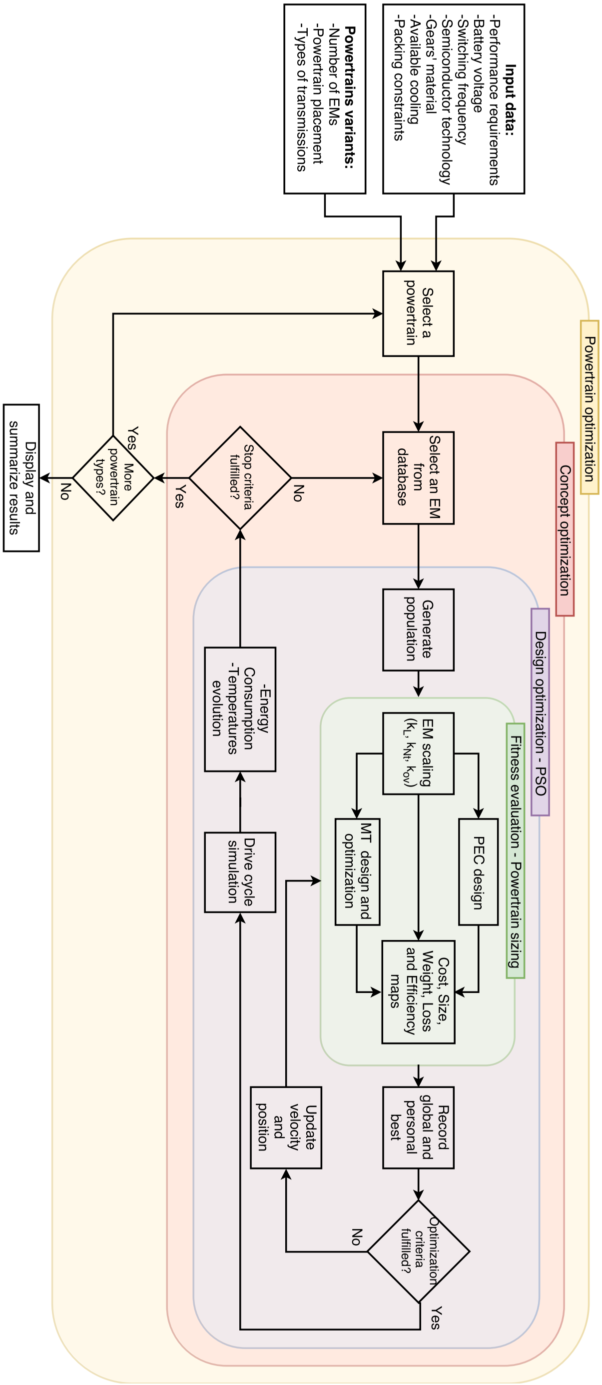

Figure 4.1: Powertrain optimization procedure.

characteristics of the different powertrain components have been found.

4.1.1 Powertrain concepts

As explained in previous chapters, there are a large number of possible powertrain configurations that may result in solutions that fulfill both the packing constraints and performance requirements. During this step, the designer defines those configurations deemed of interest for the application. The design space can be explored more exhaustively by increasing the number of configurations under study. This increases the likelihood of finding an optimal solution at the expense of a higher computational time.

There are several aspects that need to be defined for each powertrain concept under consideration. First, its layout and placement need to be specified. As described in Chapter 2, an electric powertrain can be configured and installed in a variety of ways which are likely to have an effect on the packing constraints that need to be fulfilled. Moreover, depending on which axle(s) is/are being propelled, the maximum allowable starting torque is expected to change as described in [76], which consequently can affect the sizing of the different powertrain components. Additionally, powertrain concepts with more than one EM provide the possibility of reducing the energy consumption by optimizing the split of the loads between the EMs (unless each machine is propelling an individual wheel). However, optimizing the sizing of all the powertrain components and the power split control simultaneously would significantly increase the computational time. Moreover, doing so is only relevant if energy consumption or powertrain efficiency are part of the objective function of the optimization. The use of a pre-defined rule-based power split control can be seen as a compromise that allows the inclusion of powertrain efficiency in the objective function while keeping the required computational time low. Some alternative rule-based power split control strategies that could be used are: an even split of the loads between the different EMs (suitable for example for in-wheel motors or similar concepts), or splitting the loads according to a pre-computed optimal efficiency tables (applicable, for example, to concepts with several propelled axles).

The second aspect that needs to be specified is the transmission type. This has an impact on the achievable gear ratios and packing constraints. For example, whether the input and output shafts of the transmission are concentric or parallel, impacts the way in which the packing constraints are evaluated. Similarly, any restrictions on the relationship between the different gear ratios (if applicable), as well as the minimum and maximum achievable ratios by the considered transmission type need to be defined and handled [82]. Moreover, the selection of gear ratio(s) can be an optimization problem of its own, and similarly to the case of the load split between several EMs previously described, solving it inside the main optimization loop would require a higher computational time. Therefore, it is suggested here that in a first approximation, a rule-based approach is taken for selecting the gear ratio(s).

For single speed transmissions, given an EM design able to meet the required power, the possible values for the gear ratio are constrained, as shown in (4.1), by the maximum torque and speed requirements. If such interval is empty, it is not possible to select a gear ratio that would satisfy the power, torque and speed requirements (as shown in Figs. 4.2c and 4.2d). On the other hand, if the interval described in (4.1) is not empty, there exists a range of values that can potentially satisfy the different requirements. A reasonable rule can be to select the gear ratio as high as possible in order to maximize the starting torque, which might be a desirable feature. Alternatively, the gear ratio can be selected as low as possible, in order to maximize the top speed of the vehicle. These two scenarios are represented in Figs. 4.2e and 4.2f respectively.

$$\frac{T_{max,wheel}}{T_{max,em}} \leq m_g \leq \frac{\omega_{max,em}}{\omega_{max,wheel}} \tag{4.1}$$

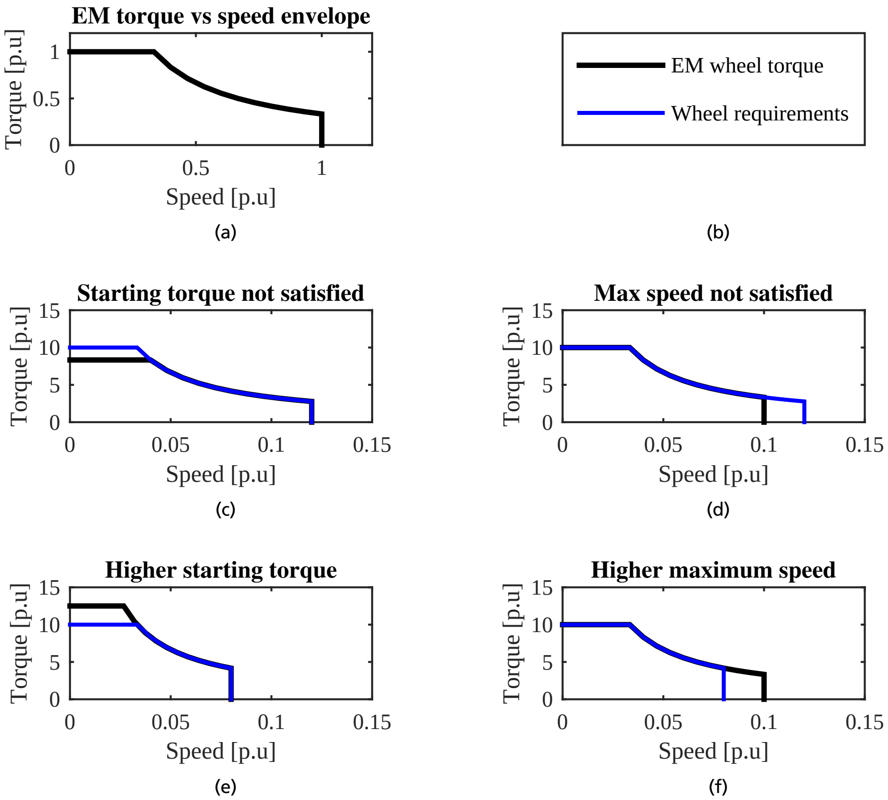

Figure 4.2: Simplified example of feasible and infeasible gear ratio selection for a single speed transmission.

Similarly, the gear ratios in a two speed transmission can be constrained as shown in (4.2, 4.3). On top of that, a condition to ensure sufficient overlapping between the two speeds is presented in (4.4), where k_{over} is a constant directly proportional to the length of the region where both gears overlap. Those equations only apply when the constant power speed range (CPSR) of the EM is lower than that required at the wheels (as shown Figs. 4.3c-e). In this case, if the first gear (highest ratio) is selected to meet the starting torque requirement and the second one (lowest ratio) is selected to meet the maximum speed demand, the overlapping between the two gears is maximized (as shown in Fig. 4.3c). Thus, in a first approximation the gear ratios can be selected according to this rule. Alternatively, it is also possible to select the gears in a way that maximizes the starting torque (see Fig. 4.3e) or top-speed (refer to Fig. 4.3d) of the vehicle. On the other hand, when the CPSR of the machine is higher than the one needed at the wheels, the range of gear ratios that can be selected is larger as shown in Figs. 4.3f-h. This opens up the possibility of increasing the size of the overlapping region, the top speed or starting torque even further. Finally, infeasible solutions can still exist if the CPSR of the EM is significantly lower than that required at the wheels (see Figs. 4.3i-k), as it is not possible to satisfy the overlapping, torque and speed requirements simultaneously.

$$m_{g1} \geq \frac{T_{max,wheel}}{T_{max,em}} \tag{4.2}$$

$$m_{g2} \leq \frac{\omega_{max,em}}{\omega_{max,wheel}} \tag{4.3}$$

$$\frac{\omega_{max,em}}{m_{g1}} \geq k_{over} \frac{\omega_{base,em}}{m_{g2}} \tag{4.4}$$

Additionally, if a two speed transmission is being evaluated, the shifting strategy should be defined at this stage. As the efficiency maps of the different components are available before performing a drive cycle simulation, it is possible to compute which of the gear ratios provides the highest efficiency at each torque and speed operating point. This is not an optimal control strategy as it neglects the effect of shifting gears in the energy consumption but it is not too far from it, as the EM can be used to quickly synchronize the shafts of the transmission during gear shifting, and shifting times below 0.1s can be achieved [110]. However, as in the previous cases, it is a compromise that allows to perform a sufficiently accurate estimation of the energy consumption without a significant increase in the required computational time.

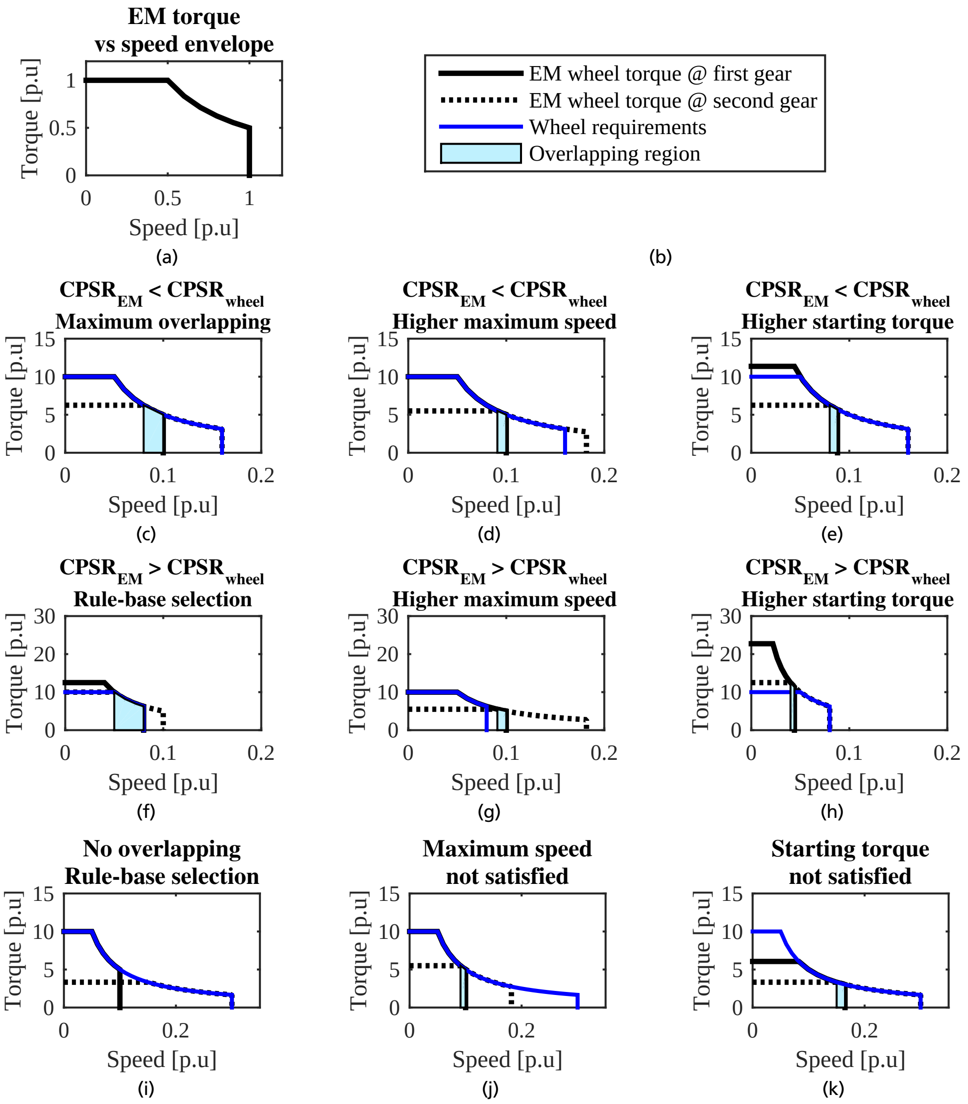

Figure 4.3: Simplified examples of feasible and infeasible selection of gear ratios for a two speed transmission.

4.1.2 Performance requirements

In electric powertrains, usually two types of performance requirements can be identified: those that need to be met continuously and those that can be satisfied by taking advantage of the overloading potential of the powertrain and therefore can only be sustained for a certain period of time. Both types of requirements need to be provided as inputs for the optimization process. They can be expressed directly as wheel torque vs speed points (as it is done for the case study in section 4.3) or given in the form of some performance metrics such as acceleration time, road gradient and speed for hill climbing, maximum time and initial speed of an overtaking maneuver, etc. which are then computed into wheel torque vs speed points to be satisfied by the powertrain, as shown in Fig. 4.4 for a compact passenger vehicle.

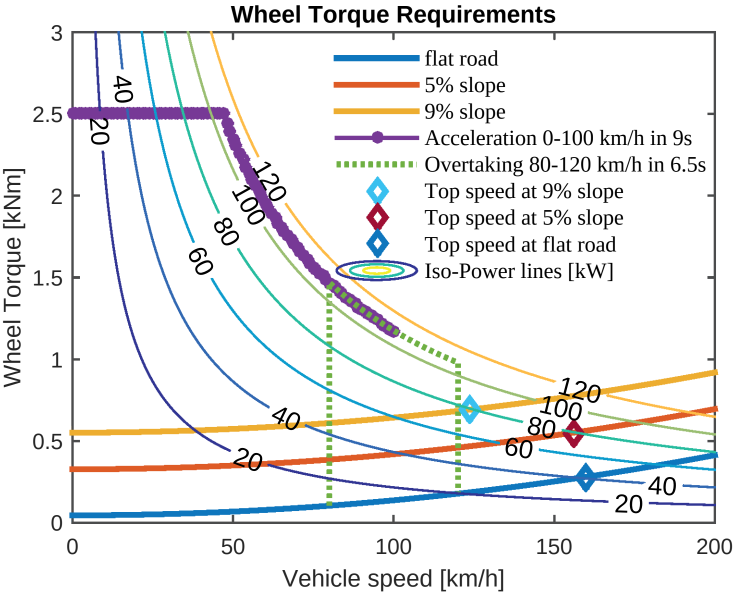

Figure 4.4: Wheel torque vs speed operating points for different performance metrics.

4.1.3 Constraints

Also constraints need to be clearly defined from the beginning and are most commonly expressed in the form of packing, weight and overloading time. The geometry of the powertrain can be intricate, and verifying the different mounting configurations is a complex task to be handled in an automated way. For this reason, in a simplified approach, the packing constraints are defined as the maximum dimensions of a box or cylinder that could enclose the EM and MT as shown in Fig. 4.5. If a possible solution cannot be fitted inside this box it can be disregarded right away without the need for further evaluation. Similarly, a constraint can be set on the maximum allowable weight of the EM and MT in the application. This last type of constraint is of special interest in un-sprung powertrains such as in-wheel motor concepts, as un-sprung masses can affect the passengers' comfort. Finally, the minimum time that the overloading current needs to be sustained can also be included as a constraint in the optimization process. Constraints on the overloading time are important in order to ensure that overtaking and acceleration maneuvers can be completed.

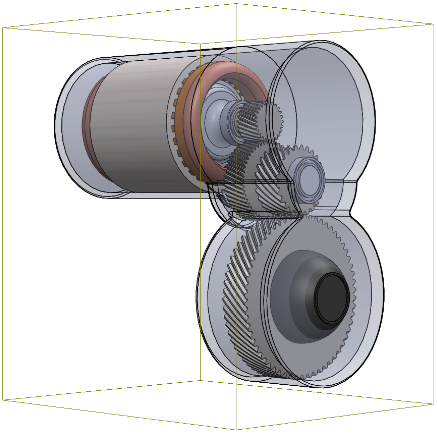

Figure 4.5: Example of how packing constraints are defined and evaluated.

4.1.4 Objective function

The function to optimize can take into consideration different aspects of the powertrain such as up-front cost, efficiency, weight, etc. As multi-objective optimization theory demonstrates, this can be handled in a variety of ways [111]. For simplicity, and given that in most cases sufficient information is available regarding the different optimization objectives and their relative importance, the presented approach consists of adding together the different functions with weight values predefined by the designer [112] as shown in (4.5) where ω_i represents the relative importance of the objective i and sf are the scaling factors used to make the different objectives comparable. By taking this approach, just a single run of the overall optimization needs to be performed in order to obtain usable results.

Alternatively, several optimizations can be performed varying the weight factors in the objective function to obtain the pareto front that describes the relationships between the different objectives. For obvious reasons, this latter approach is significantly more time consuming than the former.

$$\begin{aligned} f(x) &= \sum_{i=1}^{k} \frac{\omega_i f_i(x)}{sf_i} \\ \omega_i &\geq 0 \\ \sum_{i=1}^{k} \omega_i &= 1 \end{aligned} \tag{4.5}$$

4.1.5 Other pre-defined variables

Besides the data required to define the powertrain concepts, performance requirements, constraints and objective function, some additional parameters that have an impact on the performance, size and/or cost of the different components need to be defined in advance. These parameters are: the DC-link voltage, semiconductor technology, switching frequency (as explained in Chapter 3), gear's material and all the application dependent factors (as discussed in section 3.3), available cooling and expected production volumes. As previously mentioned, some of these parameters could be optimized rather than predefined but doing so would increase the required computational time, and in many cases some of them are known beforehand by the designer.

4.2 Powertrain optimization procedure

Once all the information described in section 4.1 has been defined, the optimization procedure can initiate. Three concentric optimization loops are used are used in the overall optimization process in order to cope with the different powertrain concepts, EM designs and characteristics respectively. Each powertrain concept is separately optimized and then the results are compared (see the yellow loop in Fig. 4.1). For each of the selected powertrain concepts, an optimization loop is executed (shown in red in Fig. 4.1). This loop starts with the selection of an EM geometry from the database. Subsequently, the number of turns, axial length and overloading factor that result in an optimal powertrain design for the selected EM geometry are obtained inside the design optimization loop (shown in purple in Fig. 4.1) as shown in (4.6).

$$\begin{aligned} Minimize: f(\mathbf{x}), &\quad \mathbf{x} = (k_A, N_t, k_{ov}) \\ s.t: k_A > 0, &\quad k_A \in \mathbb{R} \\ N_t > 0, &\quad N_t \cdot N_p \in \mathbb{N} \\ k_{ov} > 1, &\quad k_{ov} \in \mathbb{R} \\ G_m(\mathbf{x}) \leq 0, & \end{aligned} \tag{4.6}$$

The existence of both continuous (EM length and overloading factor) and discrete (number of turns) variables requires the use of an optimization algorithm able to handle mixed integer problems. In this work, particle swarm optimization (PSO) [113] is used. In this optimization algorithm the space of search is populated by a predefined number of individuals which move following the rules described in (4.7) and (4.8), where ω_{opt}, C_1 and C_2 are constants used to control the performance of the algorithm, and may be selected according to [114].

$$\begin{aligned} \mathbf{v}_i(t) = \omega_{opt} \cdot \mathbf{v}_i(t-1)+ & \\ & C_1 \cdot rand_1 \cdot (\mathbf{x}_{best,i} - \mathbf{x}_i(t-1))+ \\ & C_2 \cdot rand_2 \cdot (\mathbf{x}_{best} - \mathbf{x}_i(t-1)) \end{aligned} \tag{4.7}$$

$$\mathbf{x}_i(t) = \mathbf{x}_i(t-1) + v_i(t) \tag{4.8}$$

Once the particles have changed their position in the space of search, the cost function is evaluated at that point (see "Fitness evaluation" shown in green in Fig. 4.1), and the process is repeated until all particles converge around one point or the maximum number of iterations ($N_{iter,max}$) is reached. In order to rule out solutions that do not satisfy the requirements of the application, constraints on the total size, weight and/or required overloading time (see section 4.1.3) may be included as represented by G_m in (4.6).

As explained in the previous section, the objective function for the "design optimization loop" consists of a weighted combination of certain features such as cost, weight or size, normalized to the desired ranges. However, given the large number of times that the objective function is evaluated in the optimization of an electric powertrain, it is important that it provides an expedite execution. This is particularly relevant if energy consumption is part of the objective function, in which case it is recommended to estimate it through analytical calculations rather than a drive cycle simulation. Moreover, inside the "Fitness evaluation" loop, the PEC and MT are sized depending on the EM's characteristics. The selection of the gear ratio(s) is done according to the rule-based approach defined prior to the start of the optimization process. With the EM, PEC and MT sized, it is verified that throughout the speed range the continuous and peak wheel torque envelopes are above the required values in order for the solution to be deemed feasible. For reference, the "design optimization loop" executes in about 30s in a desktop computer with an $i7-7820X$ processor operating at 3.6GHz and 64Gb of RAM.

Once the optimal powertrain design for the selected EM geometry is obtained, the previously calculated efficiency maps for the EM, PEC and MT are used in a full vehicle simulation over a drive cycle to determine the actual energy consumption of the vehicle and temperature evolution in the different sections of the EM and PEC. At this point the design optimization loop is completed for the selected EM geometry and the process is repeated for different EM geometries until the stop criterion for the concept optimization loop is met. This criterion can be, for example, when the cost of the powertrain is below certain threshold or when all EM geometries in the database have been evaluated.

After the concept optimization loop is completed for the selected powertrain concept, the process is repeated until all concepts are optimized. This optimization approach allows to evaluate a large number of EM designs in a relatively short period of time, which provides a holistic view of the problem and can help to identify areas of interest to explore further, e.g. suggesting new EM geometries to be added to the database.

4.3 Case study

In this section, the proposed models and methodology are used in the design and optimization of a powertrain for a compact passenger vehicle. The 2018 Nissan Leaf specifications are used in this case study. The goal is twofold: (i) to provide an optimized powertrain concept that serves as the initial step for product development, and (ii) to highlight the tradeoffs and trends between different components in alternative powertrain configurations. To do so, two powertrain configurations are considered, one with a single speed gearbox and one with a two speed gearbox (see Fig. 4.6). The characteristics of the vehicle and performance requirements are summarized in Table 4.1 and Fig 4.7. Moreover, it is worth mentioning that the red diamonds and blue stars in Fig 4.7 represent the performance requirement vectors used as inputs in the optimization process.

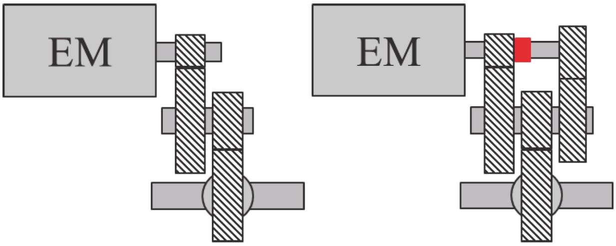

(a) Single speed transmission **(b)** Two speed transmission

Figure 4.6: Considered powertrain concepts.

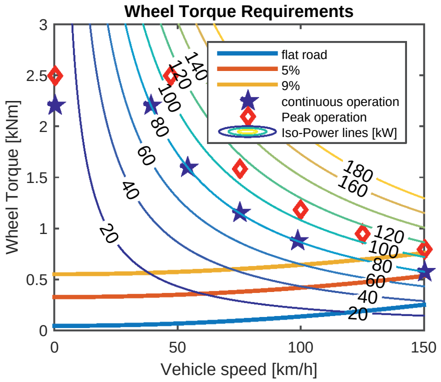

Figure 4.7: Performance requirements.

For the PSO algorithm used in the design optimization loop, the initial population set consists of 75 individuals uniformly distributed through the space of search. The optimization stops when the distance between the best individual and the farthest one is below a threshold level (set to 1% of the space of search size) or when the maximum number of iterations (100 based on preliminary runs) is reached. All the parameters, design variables, objective functions and stop criteria of the different optimization loops used in this case study are summarized in Table 4.2.

Table 4.1: Vehicle specifications

Electric vehicle specifications	
Vehicle weight	1600 kg
Top speed	150 km/h
Battery Capacity	40 kWh
Time 0-100 km/h	~ 9 s
DC-link Voltage	400V
Drag coefficient·Area ($C_d A$)	$0.26 \cdot 2.5$ m^2

The tradeoffs obtained from the optimization between powertrain weight, cost, gear ratio and the nominal power needed to meet all the requirements are presented in Fig. 4.8. Each row in the figure corresponds to an electrical machine topology (corresponding to those shown in Fig. 3.14) while the columns represent alternative powertrain concepts (depicted in Fig. 4.6). Note that for the powertrain concept with a two speed gearbox, the lowest gear ratio (highest gear) is the one plotted in the x axis. Each colored point represents a complete powertrain design where the EM is scaled together with the gear ratio(s) of the transmission until all the demands of the application are fulfilled.

For this study, the EM database consists of around 4000 EM designs with outer diameters varying from $170-340$mm (refer to section 3.2 for further details). It is worth noticing that all machines in the database are evaluated in order to accurately capture as many relevant interactions between the design parameters as possible. Additionally, a pre-selection of representative designs presents a challenging task, as different EM designs have different torque vs speed characteristics, and these vary slightly when the EM is scaled. Moreover, once the database of machines is generated, evaluating all of them is a relatively quick process, and the additional gained insights outweigh the increased computational time.

Since a large number of EM designs are evaluated for each powertrain concept, it is clear that some are not well suited for the specific application. For example, for the powertrains under consideration, machines with low constant power speed range (CPSR) need to be oversized in order to meet both the starting torque and power at maximum speed. This can be clearly seen in Fig. 4.8 at low gear ratios for both powertrain concepts and all EM topologies considered.

Table 4.2: Optimization Problem formulation

Optimizer Parameters	
ω	0.73
C_1	1.5
C_2	1.5
V_{max}	$\pm 0.1 \cdot (\mathbf{x}_{max} - \mathbf{x}_{min})$
$N_{iter,max}$	100
$N_{particles}$	75
Stop Criteria	$N_{iter} = N_{iter,max}$
	$max(\lvert\lvert x_{best} - x_i \rvert\rvert) \leq 0.01 \cdot \lvert\lvert \mathbf{x}_{max} - \mathbf{x}_{min} \rvert\rvert$
Design Optimization Loop	
Objective function	Powertrain Cost
Design Variables	k_A, N_t, k_{ov}
Bounds	$0.25 \cdot r_{so} < k_A < 4 \cdot r_{so}$
	$0 < N_t < \frac{(V_{dc}/\sqrt{6}) m_{max} I_{rms,st}}{P_{cont}}$
	$1 < k_{ov} \leq 2$
Constraints	$T_{em,wheel} \geq T_{req,wheel}$
	$t_{ov} \geq 60\,\mathrm{s}$
Concept Optimization Loop	
Stop Criterion	All EMs evaluated
Concept Optimization Loop	
Stop Criterion	All Powertrains evaluated

Note that in all cases, a slightly lower system cost can be obtained by the addition of a second speed to the transmission. This is due to the fact that the second speed helps to avoid oversizing the EM, which in turn lowers the current demands from the PEC and thus its cost.

Moreover, it can be observed that for all cases the overall cost and weight tend to decrease together with the gear ratio. Nevertheless, the benefits of increasing the gear ratio become less significant above a certain level. For the designs with a single speed gearbox, this occurs between 12-13 (see Fig. 4.9). There are several reasons for this behavior. First, both the cost and weight of the mechanical transmission increase with the gear ratio. Additionally the power density of the EMs does not increase significantly at higher speed, as no special high speed machines are included in the database. On the other hand, for those powertrains with two speeds the cost and weight flatten for ratios in the range of 10-11, where the combination of machines with slightly lower maximum speed and smaller transmissions yields to a reduction of the overall system cost.

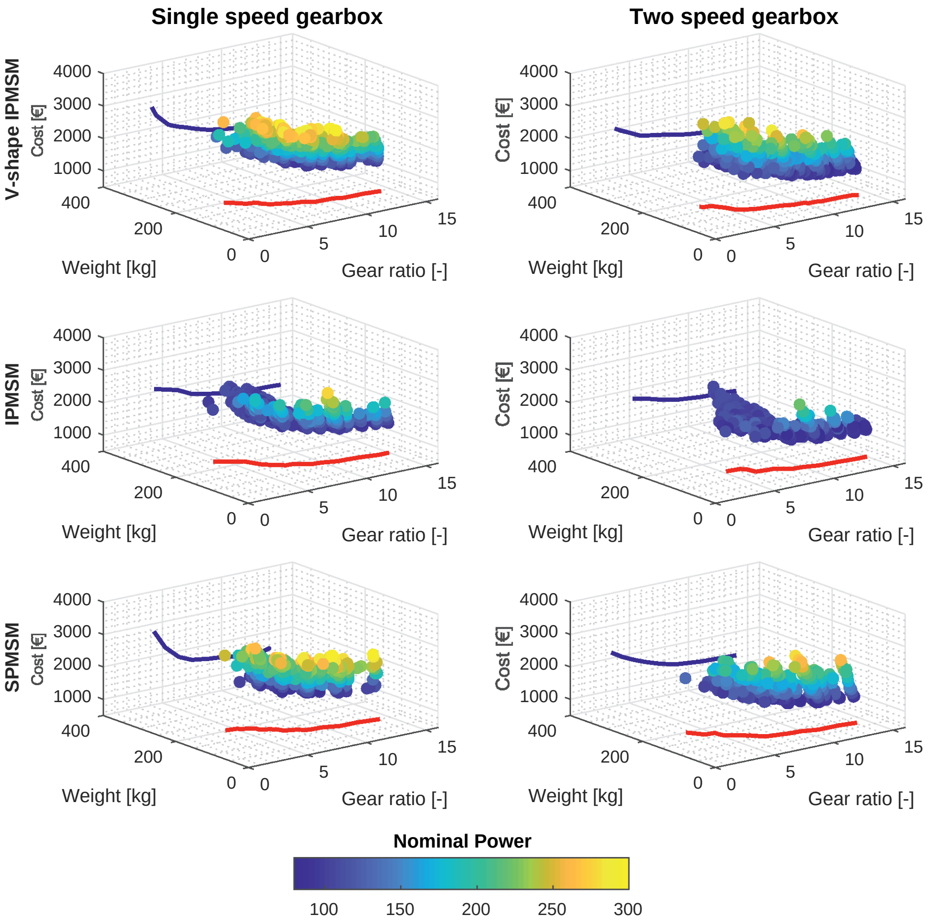

Figure 4.8: Comparison between cost, weight, gear ratio and EM rated power for different powertrain concepts using three EM topologies. The blue curve is the projection of the tradeoff front on the Cost/Gear ratio plane. The red curve is the projection of the tradeoff front on the Weight/Gear ration plane.

Another interesting tradeoff that is worth mentioning is the selection of EM topology. Although in this study the V-shape IPMSM presents the highest power density of the three considered topologies, this does not translate directly into a lower system cost as it can be appreciated in Fig. 4.9a, as the cost of the EM does not relate only to the power density. Material content and manufacturability determine to a great extent the cost effectiveness of a solution. Moreover, Fig. 4.9a indicates that good system designs, which can be competitive both in terms of cost and weight, can be achieved with the three different EM topologies.

An additional factor to ponder when designing a powertrain is the optimal CPSR of the EM, as usually an increase in CPSR comes at the expense of a decrease in power density.

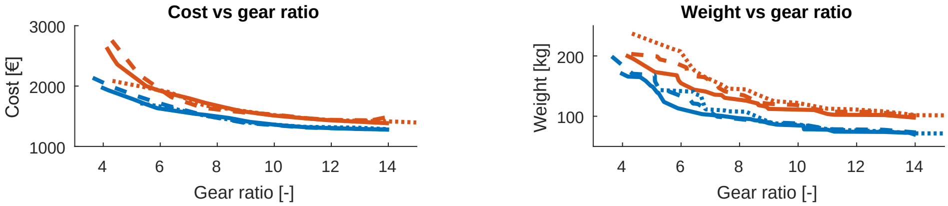

(a) (b)

Figure 4.9: (a) Cost vs Gear ratio and (b) Weight vs Gear ratio tradeoffs for cost optimized designs. Two speed gearbox concepts are shown in blue while single speed transmissions are shown in red. v-shape IPMSM, IPMSM and SMPMSM are represented by solid, dashed and dotted lines respectively.

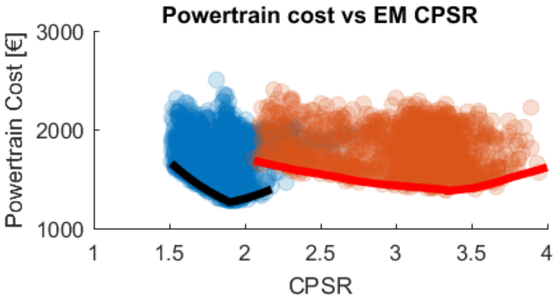

(a)

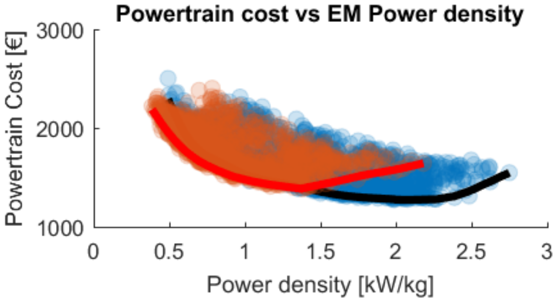

(b)

Figure 4.10: (a) Cost vs CPSR and (b) Cost vs Power density tradeoffs for all EM designs in the database when optimizing for cost. Two speed gearbox concepts are shown in blue while single speed transmissions are shown in red.

Fig. 4.10a shows how the total cost of the powertrain varies as a function of the CPSR of the EM for both powertrain types. It can clearly be observed that for a single speed gearbox transmission, the optimal powertrain cost is achieved for an EM with a CPSR between 3 and 3.5; this is the interval where the EM has sufficient CPSR to achieve all performance requirements with minimum oversizing and without sacrificing too much power density. For a two speed gearbox transmission, the optimal CPSR is significantly lower (around 1.7-2). This is due to the fact that now the EM does not need a wide CPSR to meet all the performance requirements, as it can take advantage of the second speed in the transmission. Therefore, machines with higher power density and lower CPSR are a better fit for this powertrain concept, as it is shown in Fig. 4.10b.

Table 4.3: Optimal powertrain Design

Powertrain Parameters	
EM topology	v-shape IPMSM
Axial length	0.207m
N_t	2
N_{par}	1
k_{ov}	1.12
EM N_p	6
EM number of slots per pole and phase	2
EM nominal power	97kW
EM peak power	116kW
Nominal torque	94Nm
Peak torque	103Nm
EM w_{max}	18.7krpm
First gear ratio	24.1
Second gear ratio	14

The powertrain design that provides the lowest cost is presented in Table 4.3 and the corresponding EM geometry is shown in Fig. 4.11a. It is worth noticing that the selected design is by no means a clear winner, existing several alternatives that provide a very similar overall system cost. Therefore, slight variations of the initial assumptions such as the cost of raw materials would likely change the optimal solution. A common characteristic of all these competing designs is that they feature EMs that operate at high speeds, for example, the EM in the optimal powertrain has a top speed slightly below 19 krpm and a base speed of around 10 krpm (refer to Fig. 4.11b). As it is known, increasing the EM base speed allows to achieve higher power densities and thus lower the EM material and manufacturing cost.

In Fig. 4.11c the overall powertrain efficiency (including EM, PEC and MT) at each torque and speed operating point is depicted following the shifting strategy presented in Fig. 4.11d. In both figures, solid and dotted lines are used to represent the torque vs speed envelopes in first and second gear respectively, peak operation is shown in red and continuous in blue. As mentioned in subsection 4.1.1, the selected gear shifting strategy is based on optimal powertrain efficiency and it is smoothed in order to avoid unnecessary shifting. This strategy results in a wide high efficiency region as it could be expected, which translates into a reduction in the energy consumption. However, as previously discussed, it is possible to further reduce the energy consumption of the vehicle by adjusting the values of the gear ratios but such refinement of the selected powertrain design is not included in this work.

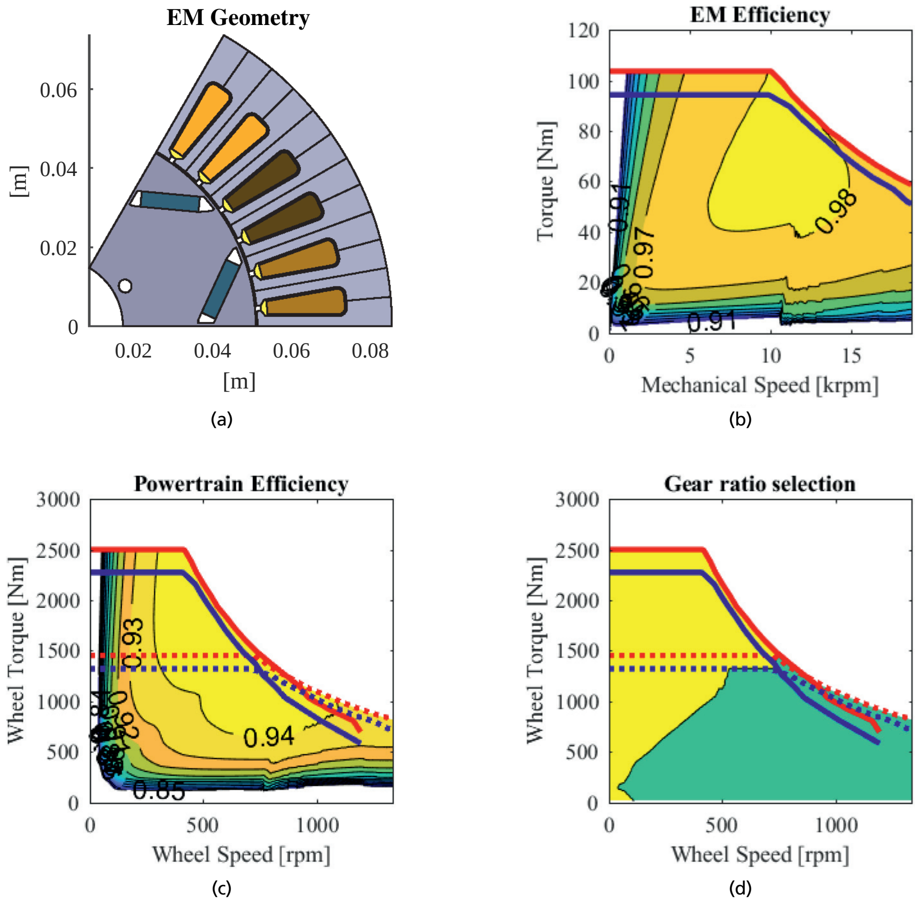

Figure 4.11: Characteristics of the optimal powertrain. (a) EM geometry, (b) EM efficiency, (c) powertrain efficiency, (d) selected gear ratio (first gear - yellow, second gear - green). Blue and red lines represent the torque envelopes at nominal and peak loading. In (c) and (d) solid and dotted lines are used to indicate the torque envelopes at first and second speed respectively

Another aspect worth of interest is the thermal performance of the selected concept. Figure 4.12b shows the temperature evolution of the different nodes of the electrical machines over one drive cycle simulation (depicted in Fig. 4.12a). In this figure, it can be observed that the different temperatures in the EM are kept at relatively low values, showing that the EM performance is not thermally limited throughout the studied drive cycle. However, it should be noted that higher maximum temperatures would be reached if the simulation is performed assuming higher starting temperatures in the EM. For example, this could be the case if a sequence of drive cycle simulations are performed after each other, assuming that the starting temperatures for one are the final temperatures of the previous simulation.

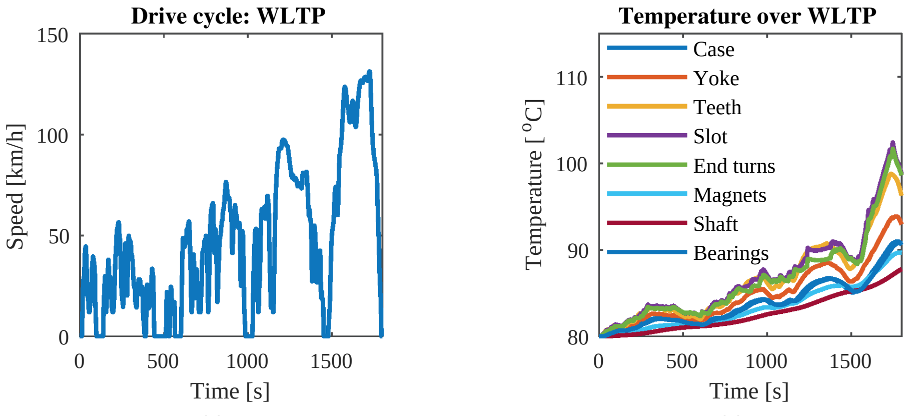

(a)

(b)

Figure 4.12: Thermal performance of the optimal powertrain over WLTP, (a) Drive cycle. (b) EM temperatures.

Chapter 5

Cost analysis of alternative charging solutions

As explained in Chapter 2, electric road systems (ERS) are technologies that enable vehicles to charge while they are in motion. These technologies allow to reduce the size of the on-board battery without sacrificing the driving range, but require a significant investment in infrastructure. In this context, it is necessary to assess whether the societal benefits of a large scale implementation of ERS outweigh the drawbacks, represented mainly in the form of investment and maintenance cost.

Since ERS are relatively new and young technologies (excluding trolley buses) the available research on the topic is rather scarce and mostly focused on the design, performance and feasibility of the technologies themselves and not on the societal impact of their future implementation. This chapter aims to shed some light on this topic in two alternative but complementary ways. First, the societal cost of electrifying a nation wide automotive fleet by several means is analyzed, with special focus on using different ERS technologies. It is worth to mentioning that this analysis is focused on BEV and ERS, thus alternative forms of electrifying road transport such as FCEV are not considered. Second, the suitability of a road to be electrified under different scenarios is assessed based on its traffic density, described by the annual average daily traffic (AADT).

The material presented in this chapter is an extension of the work previously published in [115–117] and builds upon the work initiated in [118]. The analyzes presented here take advantage of the models and tools described in Chapters 3 and 4.

5.1 Cost modeling and assumptions

All the analyzes presented in the upcoming sections are based on the quantification of the different costs required for electrifying road transport and the potential savings derived from it. In order to provide a fair assessment of the implications of alternative electrification scenarios, it is necessary to model the cost of all relevant components based on a similar set of assumptions. However, due to the wide nature of the task at hand, and considering that some of the technologies under study are relatively new, in some cases it is not possible to provide the same level of detail in the cost estimation. In such cases, best available estimations or reported figures are used instead.

When performing a cost analysis of alternative forms of electrifying road transport three major cost groups can be identified: (i) on-board components, (ii) infrastructure and (iii) energy. It is worth noticing that the cost of the components that are common between the current solution for road transport (vehicles based on ICE) and one based on BEV, is not considered. This section describes the first two cost groups. The third one on the other hand, is explained in the section 5.2 as energy costs vary widely among countries.

5.1.1 On-board components

Besides an electric powertrain (composed of a PEC, EM and MT) and a battery pack, a BEV requires other components in order to fulfill functions that in conventional vehicles are dependent of the ICE. For example, usually an isolated DC/DC converter is used in order to transfer energy from the traction battery to the service battery, replacing in this way the function of the alternator in conventional vehicles. Additionally, one or more converters might be needed in order to enable different forms of charging, whether it is low power static charging (modes 1 or 2), high power static AC charging (mode 3) or dynamic charging (conductive or inductive). Moreover, for the former form of charging, a device (often referred to as a pick-up) is needed in order for the vehicle to establish a connection with the dynamic charging infrastructure. All these components, which can be seen in Fig. 5.1, contribute to the overall added cost of the vehicle.

In this context, one of the most sensitive parameters in the upcoming analyzes is the cost of batteries. In order to narrow down the scope and given that they are the dominating chemistry in BEV today, this work only considers Li-ion batteries. As described in Chapter 1 there is a wide range of reported cost figures for Li-ion batteries, varying from 227 to 190 \$/kWh [3, 14, 15] and more recent estimates based on [119] project a cost in the range of $122 - 100$ \$/kWh for high capacity packs ($70 - 80$ kWh) [120]. Taking all this into consideration, in the upcoming sections a figure of 90 €/kWh is used.

On the other hand, the cost of all PECs (including traction inverter, the different isolated

DC/DC converters and on-board charger) are estimated using the model presented in section 3.1. For each one of the aforementioned converters, a large variety of topologies could be used. But as the purpose of this chapter is not to find the optimal design of each converter in the vehicle, the topology of each converter, switching frequency, available cooling, winding type and core material for magnetic components, input and output voltages, and operating conditions are predefined. It is evident that this yields to sub-optimal solutions. However, as the converters are sized and their cost is estimated using the same procedure and assumptions, the resulting comparison is expected to be fairer than one based on reported values from suppliers or academic publications. Additionally, in most cases there is no clear consensus on which is the optimal topology for a given application. Thus the use of reported values does not ensure the use of an optimal topology and/or design either.

Similarly, the EM for each vehicle type is selected from an initial database of around 4000 designs (refer back to section 3.2.2) and scaled to meet the demands of the application and its cost is determined as explained in section 3.2.5. The MT is designed to provide the gear ratio required by the selected EM design and to withstand the input torque. The cost of the MT is estimated as explained in section 3.3.4.

Finally, the cost of the connection devices towards the charging infrastructure, both dynamic and static, are estimated based on reported figures from active test sites [29, 32] and commercially available solutions.

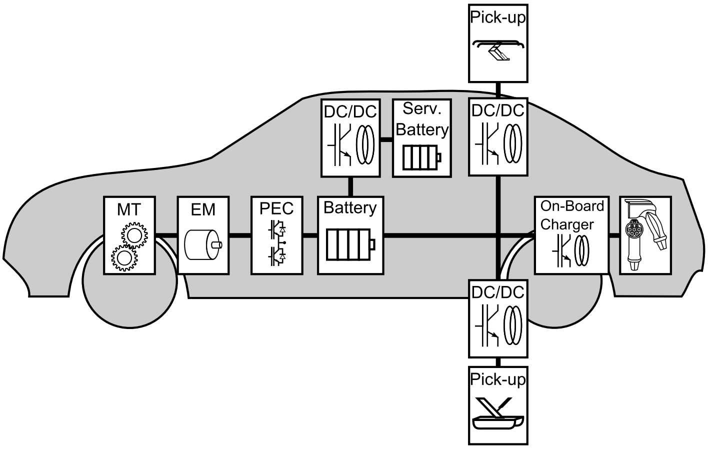

Figure 5.1: Components required for electrification.

5.1.2 Charging infrastructure

In the presented studies different forms of charging infrastructure (all of them described in detail in section 2.3) are considered depending on the scenario under analysis and the vehicle type. For this reason it is necessary to model their cost and understand the main factors affecting it.

The specific cost of a static charger can vary widely depending on the type of charger, the required power, the desired additional features and functionalities, and the amount of electrical or construction work needed at the installation site, among other factors [121]. For these reasons it is challenging to find a single specific cost figure that would be correct in all cases. However, as a first approximation, specific cost figures derived from preliminary designs of the required hardware (based on the models presented in section 3.1 considering high production volumes) and assumptions on the average amount of electrical and construction work required to install the charger at the desired location are used. This results in the specific cost of a low power static AC charging stations (mode 1) being assumed to be 100 €/kW, while for higher power static AC charging stations (modes 2 and 3) this figure rises to 140 €/kW. Similarly, the specific cost for DC fast chargers is estimated in 315 €/kW. It is worth mentioning that these figures have been compared and validated against prices for commercial solutions [121, 122].

Even more challenging is to find reliable cost estimations for ERS in the literature, since they are relatively new technologies that have not been implemented commercially but rather limited to test sites. Moreover, although ERS share commonalities with mature technologies such as trolley buses, trams and railways, the higher speeds of the vehicles, their constant change in lateral position relative to the infrastructure and their wide range of sizes and types introduces new challenges. Therefore, a cost model that considers the major components in the system has been developed [123]. The cost model is based on information and figures from the different pilot sites in Sweden [29, 30, 32] and is described in (5.1) for a road of a given length (L_{ERS}) and able to deliver a specific peak power (P_{ERS}).

$$C_{ERS} = k_0\, P_{ERS} + k_1\, L_{ERS} + k_2\, k_{ERS}\, L_{ERS}\, N_{lanes} \tag{5.1}$$

Equation (5.1) is composed of three terms that refer to specific components of the system:

1. Power term: this term accounts for the cost of those components that scale with power. They are mainly transformers and rectifying stations that provide power to the road. This term is proportional to the peak power that the road segment is expected to deliver. Peak power is assumed to be 2.5 times higher than the average power in order to compensate for changes in traffic volumes and composition (and therefore power demands) throughout the day. The constant is set to $k_0 = 300$ k€/MW.

2. Distribution term: this term accounts for the cabling placed along the road that connects the rectifying station to the feeding infrastructure on the road. Thus it is

proportional to the length of the road section. The constant is set to $k_1 = 150$ k€/km.

3. Road bound hardware term: this final term accounts for the cost of the infrastructure placed on the road and in direct contact with the vehicles. This includes the electric road segments, switches, breakers and all protection and safety systems required. Therefore, it is proportional to the length of the road that is actually equipped with electric road segments (which can be different from the total road length) represented by $k_{ERS} L_{ERS}$ and the number of lanes that are electrified (N_{lanes}) The constant is set to $k_2 = 500$ k€/km.

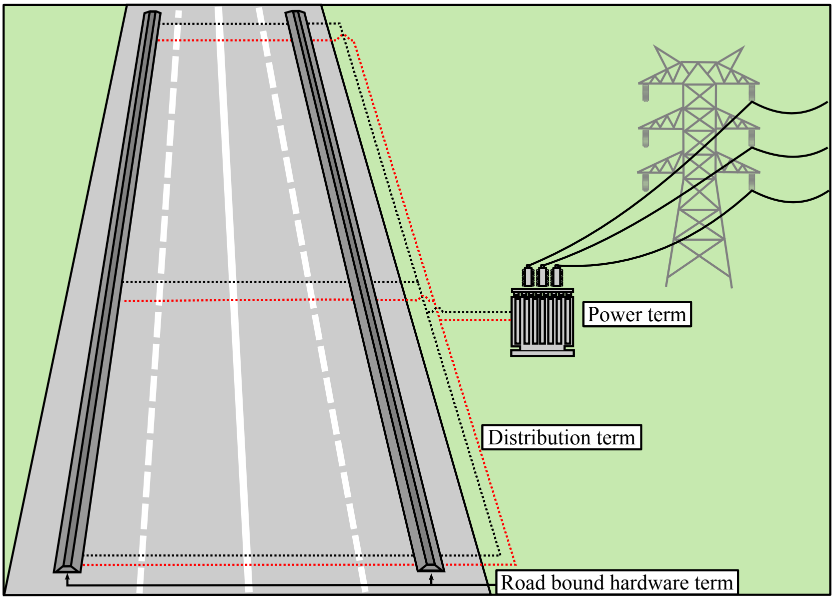

Figure 5.2: ERS cost model description.

The different terms in the aforementioned cost model are graphically represented in Fig. 5.2. It is worth mentioning that the presented cost model is developed for conductive ERS and makes no distinction between road bound or overhead solutions. Although the main difference between an inductive and a conductive ERS is on the "road bound hardware term" in this work it is assumed that the overall cost of an inductive ERS in roughly 3 times higher than its conductive counterpart, due to the lack of access to cost figures for inductive ERS solutions.

5.1.3 Other considerations

Amortization times are assumed to be 15 years for dynamic charging infrastructure, 10 years for static charging infrastructure and 5 years for the components on-board the vehicles. The exchange rate from Dollar to Euro is kept at 0.9, which was the approximate rate at the time these studies were carried out. Additionally, interest rate is assumed to be 3% and the yearly cost of maintenance for ERS infrastructure is also estimated at 3%.

5.2 Societal cost of electrification

In this section the societal cost of electrifying a nation-wide fleet is analyzed under five alternative scenarios and for different countries (Sweden and Denmark). As previously mentioned, BEV are the only electrification alternative included in the analysis, leaving out of the scope other options such as FCEV. The analysis is carried out from the perspective that the whole fleet is already electrified, thus the transition period from the current state of the fleet to the one described in the different scenarios is not considered. Moreover, as the objective of this study is not to predict how the fleet composition and use are expected to change with electrification, it is assumed that the functionality of the system, the fleet composition and the existing road network remain unaltered in the different scenarios with respect to their current state.

The proposed scenarios differ from each other on the type of charging infrastructure available for the different vehicle types and are further explained in the next section. The objective of this study is to assess and compare the cost effectiveness of alternative charging solutions when implemented at large scale in different countries. In order to simplify the analysis, the vehicles in the national fleets (both for the Swedish and Danish case) are classified based on their gross combination weight rating (GCWR) and driving patterns in four groups: (i) *Light duty*, which is dominated by privately owned passenger cars, and includes all four wheel vehicles with a GCWR below 3.5 tons. In this group, vehicles tend to have a relatively low utilization and in average to drive shorter distances. (ii) *City buses*, which includes all buses driving intra-city routes. Vehicles in this segment are characterized for having a high utilization but a low average driving speed. No limits are imposed on the CGWR of the vehicles in this group. Therefore, single-decker, double-decker and multi-articulated buses are all part of this segment. (iii) *Distribution trucks*, consists of vehicles with a CGWR between 3.6 and 16 tons. Vehicles in this group are extensively used, driving both inter and intra-city routes. (iv) *Long haul*, which is composed of long haul trucks and coach buses. The vehicles in this group are characterized for having a high utilization and driving long distances at relatively high speeds. This classification is by no means perfect, and neglects the fact that some vehicles in one group would fit better in a different one. However, it is expected that the average vehicle in a group would be a good representation the majority of the vehicles in the group in terms of performance requirement and usage patterns.

5.2.1 The Swedish case

The Swedish automotive fleet consists of about 5.2 million registered vehicles. The first category is the most numerous one, accounting for about 5.01 million vehicles including both passenger cars and vans. The fleet of city buses consists of 14 thousand units, while there are around 20 thousand distribution trucks. Finally, there are 65 thousand long haul trucks and coach buses registered in the country. Note that long haul trucks that regularly operate in the country but are registered elsewhere are not accounted for or included in the analysis. The aforementioned vehicle types account for 96% of the energy used in road transport in Sweden. The remaining 4% is consumed by two wheelers, construction equipment, recreational and specialized vehicles which are not included in the upcoming analysis as their electrification is more challenging and might require more specifically tailored solutions.

Combined, all the vehicles of the fleet (including those not considered in this study) use about 80 TWh yearly, which represents 21.6% of the total energy consumed in the country [124]. Most of this energy is converted in the country's road network, which includes 15600 km of national and European roads.

Although prices of fuel and electricity constantly fluctuate, for this study they are assumed to be fixed at 1.4 €/liter and 0.09 €/kWh respectively, which correspond to the actual figures at the time that this study was carried out. Additionally, the value added tax (VAT) is deduced from the cost of both fuel and electricity, as only societal cost is being considered.

5.2.2 The Danish Case

In contrast to Sweden, Denmark has a lower total and per capita number of road vehicles. There are 3.3 million road vehicles currently registered in Denmark. Following the classification previously described, light duty vehicles account for 2.8 millions, out of which the majority are privately owned passenger cars (2.4 millions) and the remaining are vans (400 thousand). There are 7 thousand intra-city buses, 16 thousand distribution trucks and 32 thousand long haul vehicles. Surprisingly enough there is a relatively large number of two wheelers (200 thousand) and agricultural, recreational and specialized vehicles (227 thousand). However, as in the case of Sweden and for the same reasons, these vehicles are not included in the upcoming analysis.

Although Denmark is a relatively small country (43000 km^2 neglecting Greenland and Faroe Islands) it counts with a dense road network with a total length of 73500 km, out of which 4509 km are highways and dual carriageways [125]. In total, 43.4 TWh are consumed every year by road transport in Denmark which accounts for 34% of the total energy consumed in the country [126].

The fuel and electricity cost are assumed to be 1.34 €/liter and 0.135 €/kWh based on current figures in Denmark. Moreover, as it is done the Swedish case, 20% VAT is subtracted from both fuel and electricity.

5.2.3 Scenarios

For this study, five different scenarios are proposed, the charging modes considered for each scenario are illustrated in Fig. 5.3 and the specifications for both the on-board components and infrastructure are described in this section.

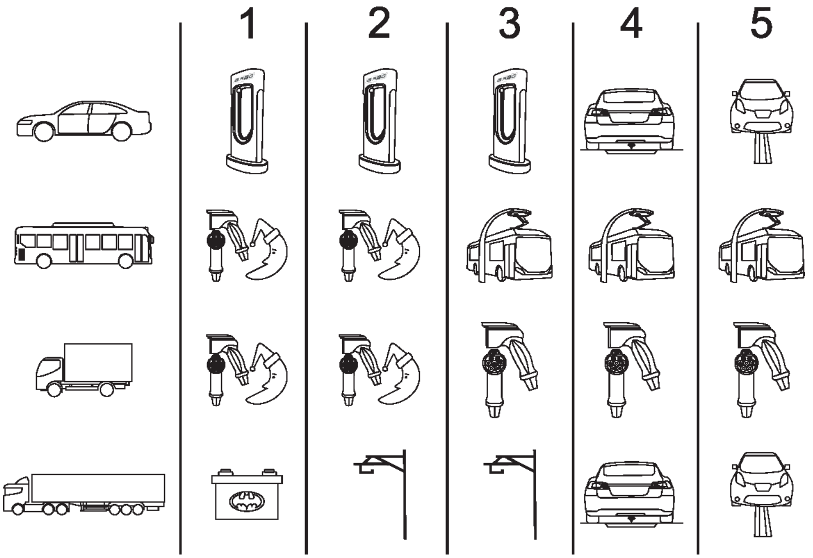

Figure 5.3: Summary of the charging modes for the different scenarios.

Scenario 1: Large batteries

In this scenario the electrification of all road transport is achieved by the sole use of batteries and high power static charging. Light duty vehicles (LDVs) are assumed to have enough battery capacity to cover a distance of 300 km and a network of fast chargers is spread through the country allowing them to charge at 120 kW. The number of fast charging stations is estimated based on a density of 48 vehicles per station. Additionally a 6 kW on-board charger is included in each vehicle in order to charge over night. City buses and distribution trucks have enough battery range to cover a full day of operation (500 kWh and 340 kWh respectively), and charging is performed over night at 70 kW and 30kW respectively. Finally, long haul trucks are equipped with enough battery capacity (480 kWh) to drive for about two hours (200 km) before needing to stop at a fast charging station to replace the tractor for a fully charged one, since it is not realistic to assume a thirty minutes break every two hours for charging. This tractor swapping requires increasing the number of tractors in the fleet in order to keep the same flow of goods as well as a high number of high power (400 kW) charging stations.

Scenario 2: Overhead electric road

This scenario introduces overhead ERS in all major roads in the country for the exclusive benefit of long haul trucks and coach buses. This reduces the required battery capacity for the aforementioned vehicles down to 120 kWh (equivalent to 60 km of range). This technology however, does not affect the other vehicles of the fleet as LDV cannot benefit from it and distribution trucks and city buses operate mainly in urban areas, so they remain unchanged with respect to scenario 1.

Scenario 3: Overhead & opportunity fast-charging

With respect to the previous case, opportunity charging is made available for city buses and distribution trucks in this scenario. It is assumed that DC fast charging stations (180 kW) are installed along the route of all city buses which allows to reduce their battery capacity from 500 to 90 kWh. For distribution trucks, high power AC chargers (43 kW) are installed in major loading/unloading docks and an on-board charger is installed in all trucks. This enables the reduction of their battery size to almost one third (120 kWh) compared to scenario 2. Long-haul vehicles and LDV are kept as described in scenario 2.

Scenario 4: Road bound inductive

The overhead ERS from scenarios 2 and 3 is replaced by an inductive road bound solution. This means that LDVs can also take advantage of the dynamic charging infrastructure. As LDVs can now charge while they drive on all major roads, their battery capacity can be reduced to provide about 60 km of driving range (15 kWh). The change on ERS does not affect the battery capacity of long haul vehicles compared to scenario 2 but it slightly changes the required equipment on-board. On the other hand, city buses and distribution trucks remain unchanged with respect to the previous scenario.

Scenario 5: Road bound conductive

The inductive ERS from scenario 4 is replaced by a conductive solution, which is expected to be cheaper in terms of infrastructure but requires additional components on-board the vehicle in order to provide galvanic isolation between the electricity supply from the road and the high voltage system on-board the vehicle, as no protective earth connection can be ensured during dynamic charging. The rest of the fleet and infrastructure remains unaltered with respect to scenario 4.

A summary of the vehicle and infrastructure configurations for the different scenarios is presented in Table 5.1.

Table 5.1: Vehicle configurations

Vehicle	Scenario	Battery energy	Energy consumption	Traction Power	Slow charge	Fast charge	E-road
Units	-	kWh	kWh/km	kW	kW	kW	kW
Light duty	1	72	0.2	100	6.0	120	0
	2	72	0.2	100	6.0	120	0
	3	72	0.2	100	6.0	120	0
	4	15	0.2	100	3.3	0	25
	5	15	0.2	100	3.3	0	25
City bus	1	500	1.2	150	70	0	0
	2	500	1.2	150	70	0	0
	3	90	1.2	150	6	180	0
	4	90	1.2	150	6	180	0
	5	90	1.2	150	6	180	0
Distribution truck	1	340	1.5	150	30	0	0
	2	340	1.5	150	30	0	0
	3	110	1.5	150	10	43	0
	4	110	1.5	150	10	43	0
	5	110	1.5	150	10	43	0
Long haul	1	480	1.6	300	40	400	0
	2	120	1.6	300	10	110	200
	3	120	1.6	300	10	110	200
	4	120	1.6	300	10	110	200
	5	120	1.6	300	10	110	200

5.2.4 Results and discussion

Using the assumptions presented in previous sections, it is possible to calculate the yearly societal cost of electrifying all road transport in Sweden and Denmark for all the described scenarios, as shown in Figs. 5.4 and 5.5. In this figures, the positive segments represent the yearly investments in infrastructure and on-board components needed in order to fully electrify the nation's fleet. On the other hand, the negative segments represent the potential savings that can be obtained yearly due to the removal of the conventional powertrain, increase in energy efficiency of the vehicle and lower cost of electricity compared to fossil fuels.

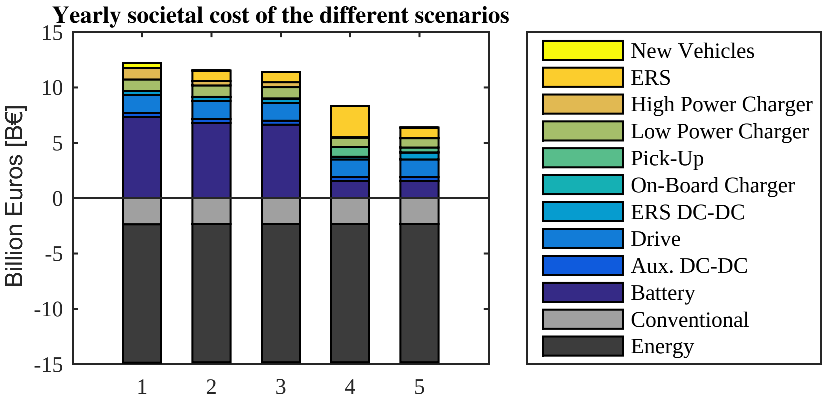

Figure 5.4: Societal cost of electrifying all Swedish road transport under five different scenarios.

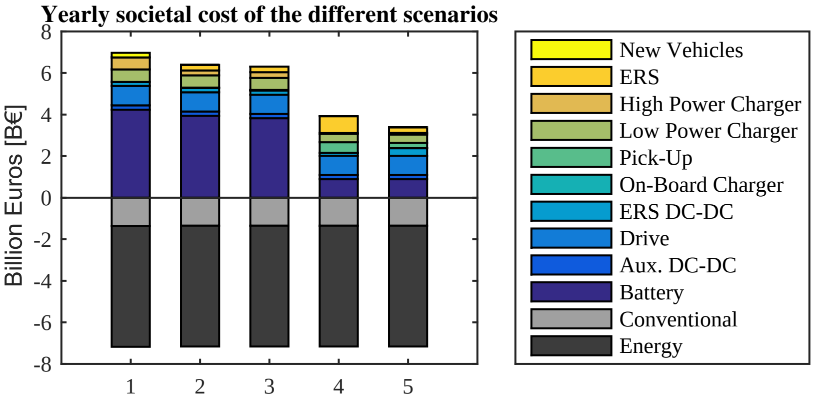

Figure 5.5: Societal cost of electrifying all Danish road transport under five different scenarios.

There are several aspects that can be concluded from comparing Figs. 5.4 and 5.5. The first, and most obvious one, is that the overall cost of electrifying the Swedish automotive fleet in all scenarios is higher than its Danish counterpart. This is due to the fact that Sweden has a higher total number of vehicles in its fleet and a longer road network to be electrified in scenarios 2 – 5. The second aspect that is interesting to notice is that, roughly speaking, both countries follow the same trend regarding the cost effectiveness of electrification in the different scenarios; with the first scenario presenting the highest societal cost and the last one the lowest. Moreover, the most significant cost reduction is achieved when the electric road infrastructure is made available to all vehicle kinds (transition from scenario 3 to 4).

It is also important to highlight that for both countries the overall cost of electrification is lower than the potential savings in all scenarios. When analyzing this, it has to be kept in mind that the initial assumption for the battery cost of 90 €/kWh was considered significantly low at the time this study was conducted, which makes an easier case for electrification. Nevertheless, the most recent estimations for battery cost from one of the most popular EV manufacturers suggest that this figure could be reached in the near future. Figure 5.6 presents a sensitivity analysis showing the net societal cost minus savings when varying the assumed cost of batteries. It can be seen in Fig. 5.6a that electrification remains cost effective with battery costs up to 120 €/kWh for scenario 1, and 135 €/kWh for scenarios 2 and 3. On the other hand, as Denmark has a higher cost of electricity and cheaper fuels than Sweden (i.e. lower savings per vehicle), electrification barely remains cost effective in scenario 1 under the initial assumptions in battery cost, and 110 €/kWh for scenarios 2 and 3 (refer to Fig. 5.6b). Moreover, scenarios 4 and 5 remain cost effective even after doubling the initial assumption on battery cost, as shown in Fig. 5.6. This is due to the fact that most vehicles in this scenarios have significantly smaller battery packs but provide the same cost savings as in scenarios $1 - 3$.

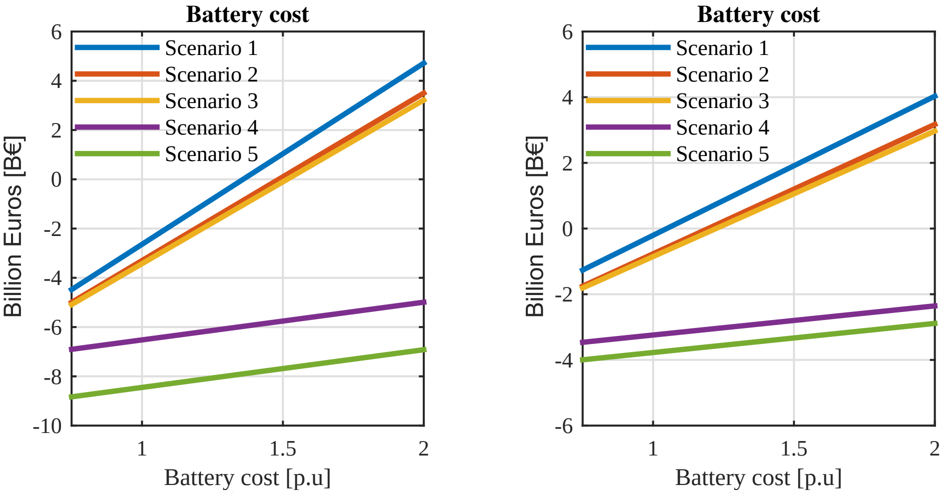

(a)

(b)

Figure 5.6: Sensitivity analysis on the cost of Li-ion battery pack for (a) Sweden and (b) Denmark.

The number and cost of DC fast charging stations are assumptions that can easily be challenged. In order to analyze the impact of these assumptions in the overall societal cost of electrification, a sensitivity analysis is performed on the cost of charging stations as presented in Fig. 5.7. From this figure it can be seen that for both countries scenario 1 is the most affected by changes in the cost of charging stations. This is due to the high number and power of the charging stations needed in order to keep the tractor-swapping system working without delays. On the other hand, when DC fast charging stations are used only for passenger vehicles (scenarios 2 and 3), it can be observed that the system is less sensitive to variations in the cost of the stations. Scenarios 4 and 5 are not affected in any significant way by the cost of fast charging stations as they are only used by city buses and distribution trucks and their total number is quite low.

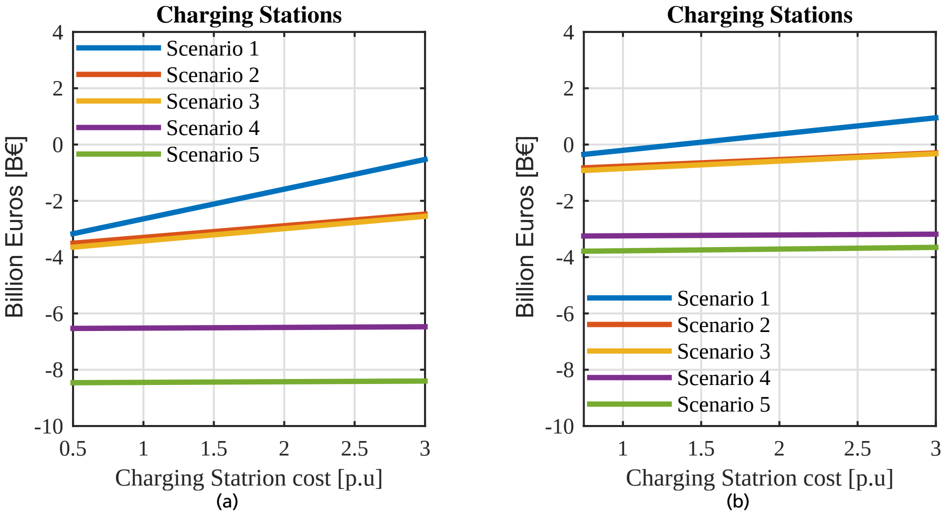

Figure 5.7: Sensitivity analysis on the cost of charging stations for (a) Sweden and (b) Denmark.

Although a detailed cost model for ERS is presented in section 5.1.2, this is one of the figures that presents the most uncertainty because all ERS concepts included are relatively young technologies which are currently not being commercially produced at any significant volume and there is also a lack of experience regarding durability and require maintenance. For this reason, a sensitivity analysis is presented in Fig. 5.8 for overhead solutions and Fig. 5.9 for road bound ones. It is interesting to notice that in the case of Sweden, scenarios 2 and 3 remain more cost effective than scenario 1 even with increases in the cost of overhead ERS of 70% (as shown in Fig. 5.8a). For Denmark on the other hand, the cost of overhead ERS can increase by a factor of three and scenarios 2 and 3 would still remain more cost effective than scenario 1 (refer to Fig. 5.8b). This difference between Sweden and Denmark is due to the higher density of vehicles in the Danish roads. When looking at the impact of the cost of road bound conductive solutions, it is possible to appreciate that even with a three fold increase in the cost of this type of ERS, scenario 5 remains more cost effective than 1-3 and barely approaches scenario 4 in the most extreme case.

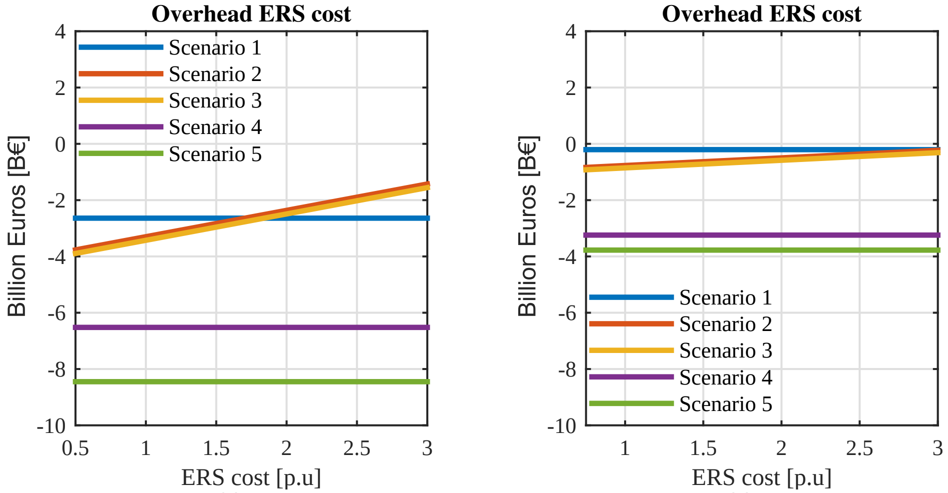

(a) (b)

Figure 5.8: Sensitivity analysis on the cost of overhead conductive ERS for (a) Sweden and (b) Denmark.

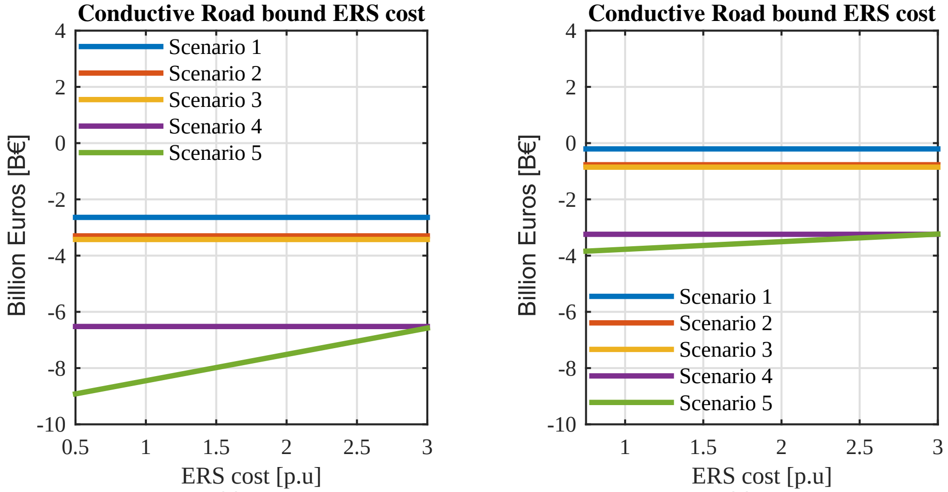

(a) (b)

Figure 5.9: Sensitivity analysis on the cost of road bound conductive ERS for (a) Sweden and (b) Denmark.

Another interesting comparison between the societal cost of electrifying Sweden and Denmark can be made based on how much the potential cost savings are with respect to the required investment in each scenario as shown in Fig. 5.10. It can be observed that for the first three scenarios the differences between the relative savings in both countries are significant. The main reasons for this is that Sweden consumes a higher amount of energy per vehicle and has a remarkably low electricity cost. These factors increase the relative savings gap between the two countries. Interestingly, when a road bound inductive ERS is introduced, Denmark has a higher potential benefit than Sweden. This has to do with the fact that the number of vehicles per *km* of major road in Denmark is around 650 while in Sweden is half of that, meaning that the infrastructure investment is spread among the savings from a higher number of vehicles in the Danish case. However, when the cost of the ERS infrastructure is reduced (moving from scenario 4 to 5) the difference in energy consumption and energy cost becomes the most significant factor again and the potential benefit becomes larger for Sweden.

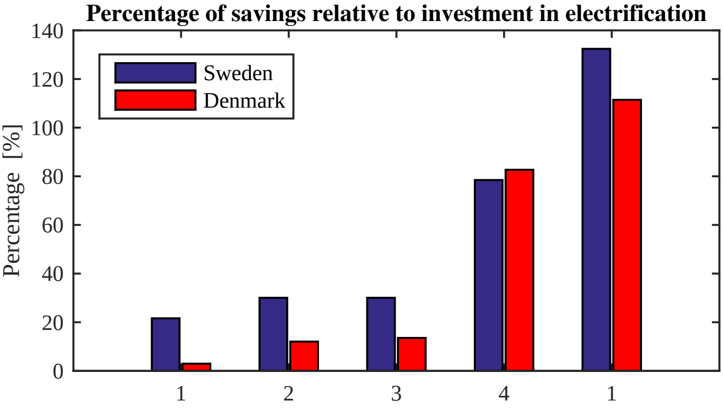

Figure 5.10: Savings comparison between Sweden and Denmark.

5.2.5 Conclusions

From the results and sensitivity analysis presented in this section, it is clear that ERS offers a potential to dramatically reduce the electrification cost of a nation-wide automotive fleet. However, in order to achieve this the selected technology needs to be accessible to both heavy and light vehicles, and needs to be deployed in a sufficiently large scale to affect the sizing of the components on-board the majority of the vehicles in the fleet. The marginal savings in the societal cost from scenario 1 to 2 and 3 compared to the significant savings provided in scenarios 4 and 5 motivate why ERS should be available to all vehicle categories.

Moreover, this study shows that although it is important to account for the particular conditions of different countries when assessing the societal cost of alternative forms of electrification, for the scenarios under consideration, similar conclusions can be made when analyzing the Swedish and Danish cases.

5.3 Equivalent energy cost of operating the automotive fleet

In the previous section it is shown that ERS are promising solutions that have the potential to significantly reduce the overall cost of electrifying a nation-wide fleet. In that analysis the transition phase is neglected and emphasis is made on the societal cost effectiveness of the final system solution once the full fleet is electrified. However, it is evident that if ERS are to be implemented at large scale, the roll out of the infrastructure as well as its adoption would happen in progressive steps. In this context, this section analyzes the societal cost of electrifying the traffic on a specific road using different technologies, and compares it with the corresponding cost if all these vehicles featured a more conventional combustion engine powertrain. The objective is to identify which roads are more beneficial to electrify from a societal perspective, as they would be good candidates to be electrified first. The analysis presented in this section is based solely on the traffic density and composition of the roads, meaning that other aspects such as their geographical location, connection to other roads or urban and industrial centers are not taken into consideration when assessing the suitability of the road to be electrified.

An electromobility equivalent energy cost (C_{emob}) is introduced in order to facilitate this analysis. C_{emob} represents the cost of using 1 kWh of electricity in transportation including the cost of energy, depreciation of components and infrastructure, and is calculated as shown in (5.2).

$$C_{emob} = C_e + C_{comp} + C_{inf} \tag{5.2}$$

The first term in this equation (C_e) represents the cost of 1 kWh of electric energy, excluding VAT. The second term (C_{comp}) accounts for the depreciation of the electromobility related components. It is worth noticing that the cost of all the component needed in order to electrify the vehicle ($C_{on-board}$) is depreciated based on the energy they are expected to convert over the life time of the vehicle, as described in (5.3), where e_x is the average energy consumption of the vehicle type "x" (given in kWh/km), $d_{x,year}$ is its average yearly driven distance, k_i is the interest rate and t_a is the amortization time.

$$c_x = \frac{C_{on-board}}{e_x \, d_{x,year}} \frac{k_i}{1 - (1 + k_i)^{-t_a}} \tag{5.3}$$

As it could be expected, both the cost of on-board components ($C_{on-board}$) and the average yearly energy consumption ($e_x \, d_{x,year}$) vary significantly between passenger vehicles and trucks. Therefore, C_{comp} needs to be calculated as the weighted average of the c_{Cars} and

c_{Trucks} for the specific traffic composition of the road under study, as shown in (5.4).

$$C_{comp} = \frac{c_{Truck} AADT_{Trucks}\, e_{Truck} + c_{Car} AADT_{Cars}\, e_{Car}}{AADT_{Trucks}\, e_{Truck} + AADT_{Cars}\, e_{Car}} \tag{5.4}$$

The last term in (5.2) refers to the cost of the charging infrastructure (C_{inf}), both ERS and DC fast charging (if applicable), depreciated by the total energy supplied by the system over its amortization time. The cost of the ERS is estimated as described in section 5.1.2. It can be observed that (5.1) requires the degree of electrification (k_{ERS}) to be defined beforehand. The selection of the optimal k_{ERS} depends on a variety factors such as geographical location, existence of exit/entrance ramps, road gradient, fleet composition, connections to other roads, ease of installation, etc. Therefore, in a practical application k_{ERS} is likely to differ between roads. Moreover, if vehicles are expected to perform charge sustained trips while driving on an ERS, the required charging power is inversely proportional to the selection of k_{ERS}. Assuming a minimum required battery capacity equivalent to 60 km of driving range (d_{range}), that only a fraction of the installed battery capacity (k_{batt}) can be used for traction and a maximum charging rate (C_{rate}) of 2C (in order to preserve the lifetime of Li-ion batteries), a rough optimization aiming to minimize the combined cost of the ERS infrastructure (C_{ERS}) and on-board batteries (C_{batt}) of the fleet can be performed. This optimization, requires the definition of the vehicle fleet size and composition (N_{car} and N_{truck}) as well as the length of the road network (L_{road}) and number of lanes (N_{lanes}) to be electrified. Equations (5.5)-(5.7) show how the cost of the infrastructure and on-board batteries is calculated using the assumptions previously described.

$$\begin{aligned} C_{ERS} = &\left(\frac{k_0 (e_{car}\, d_{car,year} + e_{truck}\, d_{truck,year}) 2.5}{24 \times 365} + k_1 L_{road} + \right. \\ &\left. k_2 L_{road} N_{lanes} k_{ERS} \right) \frac{k_i}{1-(1+k_i)^{-t_{a,inf}}} \end{aligned} \tag{5.5}$$

$$C_{batt} = C_{batt,kWh} (B_{cap,car} N_{car} + B_{cap,truck} N_{truck}) \frac{k_i}{1-(1+k_i)^{-t_{a,veh}}} \tag{5.6}$$

$$B_{cap,x} = max \left(\frac{d_{range,x} e_x}{k_{batt}}, \frac{e_x v_{ave,x}}{C_{rate} k_{ers}} \right) \tag{5.7}$$

Figure 5.11 shows the aforementioned optimization of the k_{ERS} value for the Swedish road network and fleet as described in section 5.2.1, considering only light duty and long haul vehicles. It can be observed that for k_{ERS} values lower than 0.5, it is necessary to increase the battery capacity of the vehicles in the fleet (and therefore its associated cost) in order to keep the charging rate at a maximum of 2C. On the other hand, for k_{ERS} higher than 0.5 the battery capacity remains constant in order to provide the minimum required driving range of 60 km. From Fig. 5.11 it can be concluded that a k_{ERS} value of approximately 0.5 minimizes the overall ERS and battery cost for the selected fleet and road network, and thus it is the value used in the upcoming sections.

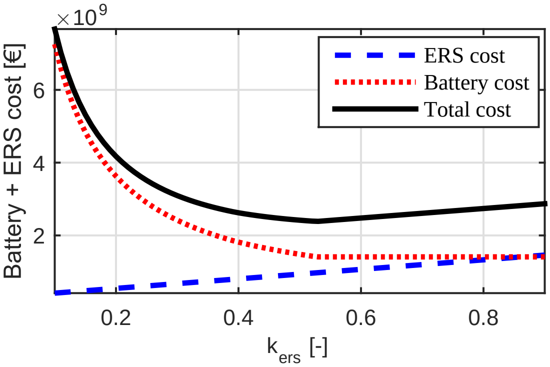

Figure 5.11: Selection of the degree of electrification k_{ers} for Swedish national and European roads.

Finally, in order to compare the cost of operating an electrified fleet with a conventional one, the cost of the amount of fossil fuels (C_{fuel}) needed in order to provide the same amount of tractive energy as 1 kWh of electricity used by an electric powertrain in transportation needs to be estimated. This requires several assumptions: first it is assumed that an electric vehicle has an overall average efficiency (including charging) of 78%, while an ICE vehicle has an average efficiency of 25%. Additionally it is assumed that a liter of fossil fuel contains 10 kWh of energy. Considering all this, the resulting C_{fuel} is roughly 0.35 €/kWh. It is worth noticing that the average efficiencies of both conventional and electric vehicles depend on a variety of factors, from the specifics of their powertrain design to the drive cycle, road gradient, weather conditions, etc. Therefore, it is important to keep in mind that C_{fuel} is used as an indication on how the electrified and the conventional fleet compare under different scenarios and traffic conditions.

5.3.1 Calculation scenarios

Three different scenarios are proposed here in order to analyze the impact of different electrification technologies in the equivalent energy cost of operating the vehicle fleet passing through an specific road. In all scenarios, it is assumed that all vehicles are either PHEVs or EREVs, thus savings due to the removal of the conventional powertrain are not accounted for. The reason for this is that during early stages of ERS deployment, vehicles should be capable of driving significant distances in roads that are not yet equipped with dynamic charging infrastructure in order to fulfill the transport demands of the society.

Scenario 1: ERS based on overhead lines only for trucks, cars remain on fossil fuels

The electrification of long haul vehicles presents several challenges and opportunities simultaneously. On one hand, their high weight and energy consumption, long driving distances and profit oriented operation makes them hard to electrify using large battery packs and static charging infrastructure, as it is currently being done with passenger cars, since the loss of payload and long charging times would negatively affect their use. On the other hand, as they operate mostly on predefined routes following predictable driving patterns they are in a unique position to lead the deployment of ERS. In this context, the first scenario analyzes the implications of only electrifying long haul vehicles by using ERS based on overhead lines. As previously mentioned, in addition to an electric powertrain and all the components required to take energy from the ERS the trucks are assumed to be equipped with sufficient battery capacity for 60 km of driving range. On the other hand, cars remain using ICE, and therefore do not influence the cost calculation.

The electromobility equivalent energy cost for this scenario is presented in Fig. 5.12a. As previously explained, since cars are not electrified they do not affect the resulting C_{emob}. However, in order to fairly compare the cost of using energy in transportation from this scenario with the upcoming ones, it is necessary to account for the cost of operating the fleet of passenger vehicles, as shown in Fig. 5.12b. From both figures it is possible to deduce that for a road with a AADT_{Truck} higher than 900, the resulting C_{emob} is below the equivalent cost of operating a conventional fleet (C_{fuel}), meaning that societal gains can be obtained from the installation of ERS in such road. However, it is important to keep in mind that this scenario does not reduce the emissions derived from light duty vehicles (which currently account for 55-60% of the total road transport emissions in Europe [127]), regardless of how the C_{emob} from this scenario compares with the upcoming ones.

Scenario 2: ERS based on overhead lines only for trucks, cars become battery electric vehicles

In the second scenario, all passenger vehicles are electrified by means of high capacity battery packs (72 kWh) and fast charging stations (with the same density as explained in section 5.2.3). On the other hand, long haul vehicles remain as in the previous scenario, having sufficient battery range for 60 km of driving and taking advantage of the overhead ERS installed along the roads.

The resulting electromobility equivalent energy cost for this scenario is presented in Fig.

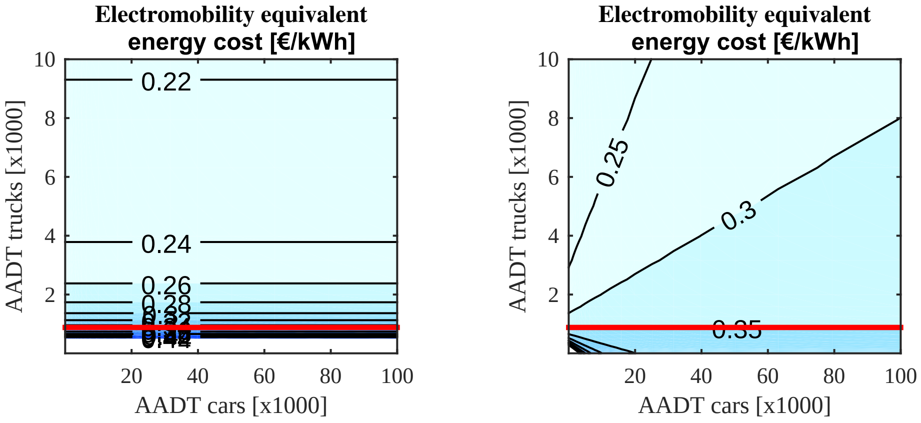

(a)

(b)

Figure 5.12: Electromobility equivalent energy cost C_{emob} for overhead lines ERS only for trucks; cars remain on fossil fuels.

5.13a. Several conclusions can be drawn from this figure; the first and most evident one is that for any AADT$_{Cars}$, increasing the AADT$_{Trucks}$ lowers the C_{emob}. The main reason for this is that the cost of on-board components depreciated in energy for the trucks is significantly lower than that of the cars, as it can be observed in Fig. 5.13b. On the other hand, the average power delivered by the ERS per km is presented in Fig. 5.13c and it is used to calculate the corresponding ERS cost according to (5.1), and consequently the depreciated cost of the charging infrastructure as shown in Fig. 5.13d. From this last figure it can be observed that any increase in the traffic volume, whether it is trucks or cars, lowers the depreciated cost of the infrastructure, as more energy is being converted through the system.

Scenario 3: Road-bound ERS for both trucks and cars

The final scenario illustrates the impact of making ERS technology accessible to both vehicle types. Therefore, road bound ERS replaces the overhead lines used in the previous scenarios. This has a major effect on the on-board components of passenger vehicles as now their battery pack can be reduced from 72 kWh to only 15 kWh (providing a driving range of about 60 km). Trucks, on the other hand, remain the same with the exception of being equipped with a different kind of pick-up to connect to the ERS.

In this scenario, the obtained C_{emob} (shown in Fig. 5.14a) is in general lower than the one obtained in the previous one (compare with Fig. 5.13a) for most combinations of AADT$_{Cars}$ and AADT$_{Trucks}$. However, although the cost of the on-board components for cars is significantly reduced due to the lower battery capacity installed, the cost of the on-

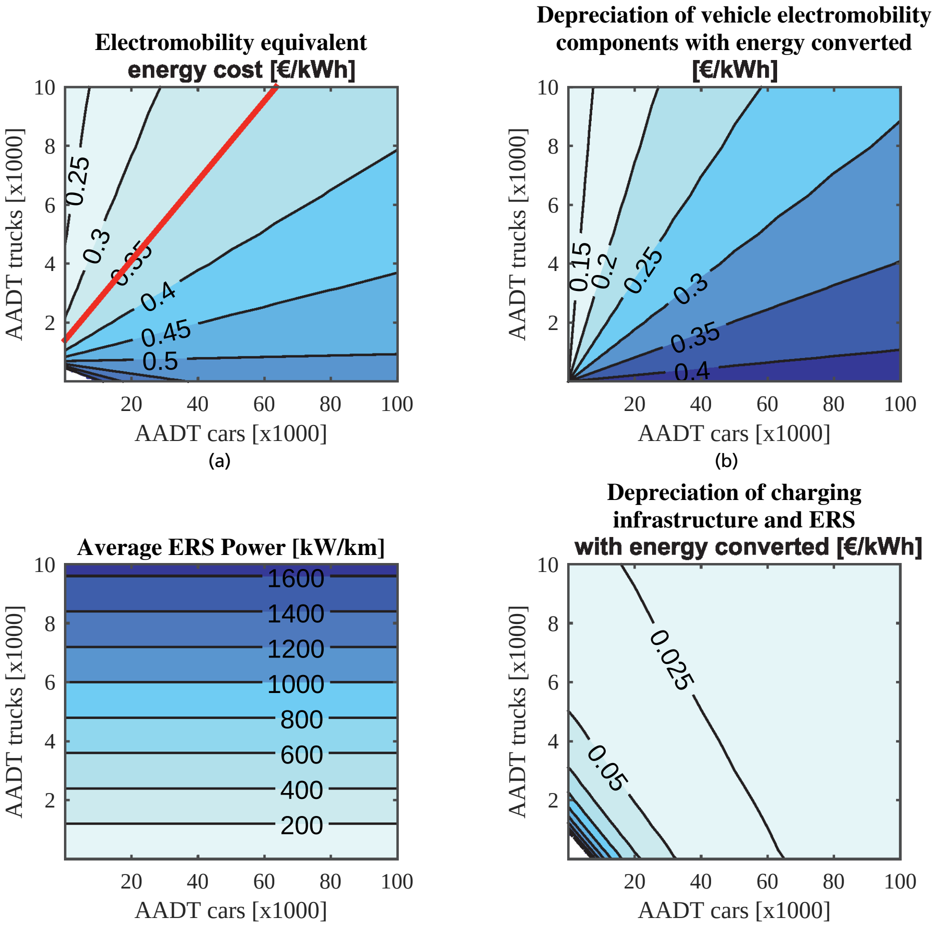

(a) (b) (c) (d)

Figure 5.13: Cost analysis for ERS based on overhead lines only for trucks; cars electrified with batteries.

board components depreciated over the total energy converted, remains higher than that of trucks, due to the lower energy converted by cars throughout their life. This causes that once a minimum number of trucks is reached, $\text{AADT}_{Trucks} > 1300$, increasing the volume of cars results in an increase in the C_{emob}.

On the other hand, it can be seen that since the ERS infrastructure is being shared by both vehicle types, the average delivered power per km also increases as shown in Fig. 5.14c, which consequently lowers the depreciated cost of the charging infrastructure (see Fig. 5.14d) as more vehicles use it and static charging stations can be spared.

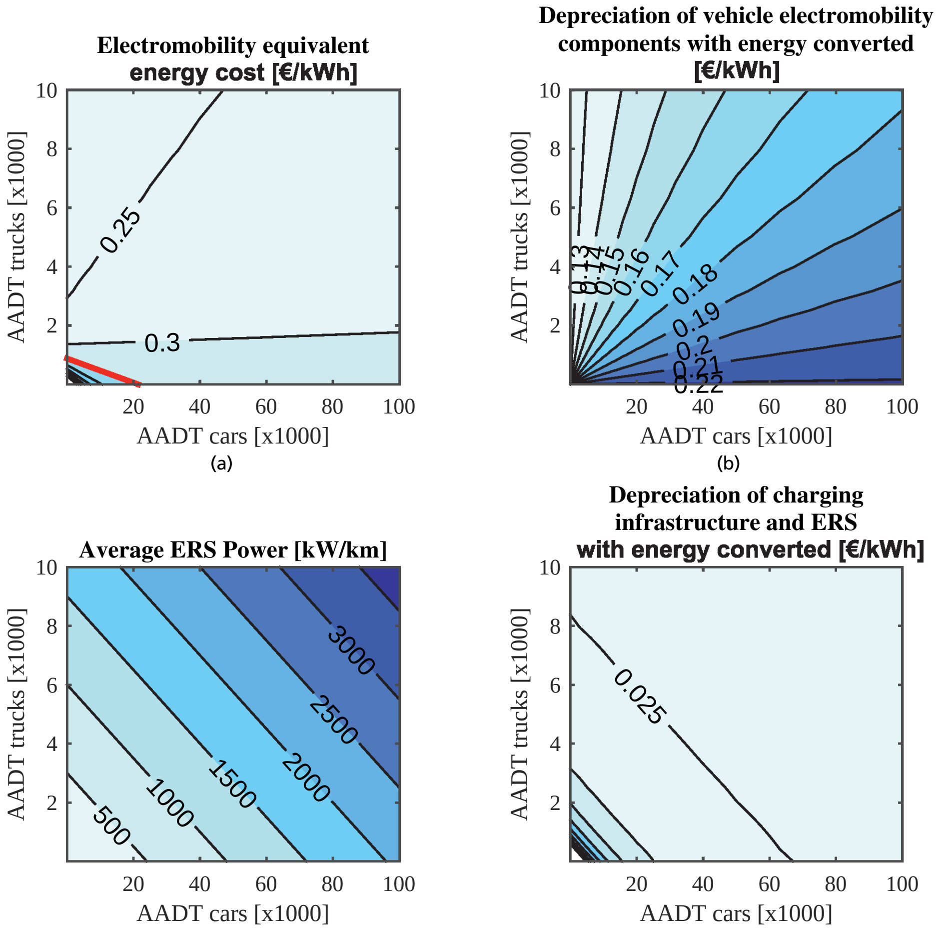

(a) (b) (c) (d)

Figure 5.14: Cost analysis for road-bound ERS for trucks and cars.

5.3.2 Case example

In order to demonstrate how the developed metric can be used to assess the suitability of a road to be electrified under different scenarios, two relevant roads in southern Sweden are analyzed under scenarios 2 and 3. The selected roads are European road E6 and E22. In Sweden, they both start in Trellebog and overlap until Malmo where they split. The E6 continues along the west coast of Sweden before reaching Norway while the E22 crosses Scania transversally before entering in Blekinge.

The traffic data for this study is obtained from the Swedish Traffic Agency, which provides the total and heavy vehicle AADT for both driving directions and in numerous points along the road [128]. Since the AADT for passenger vehicles is not directly available, it is

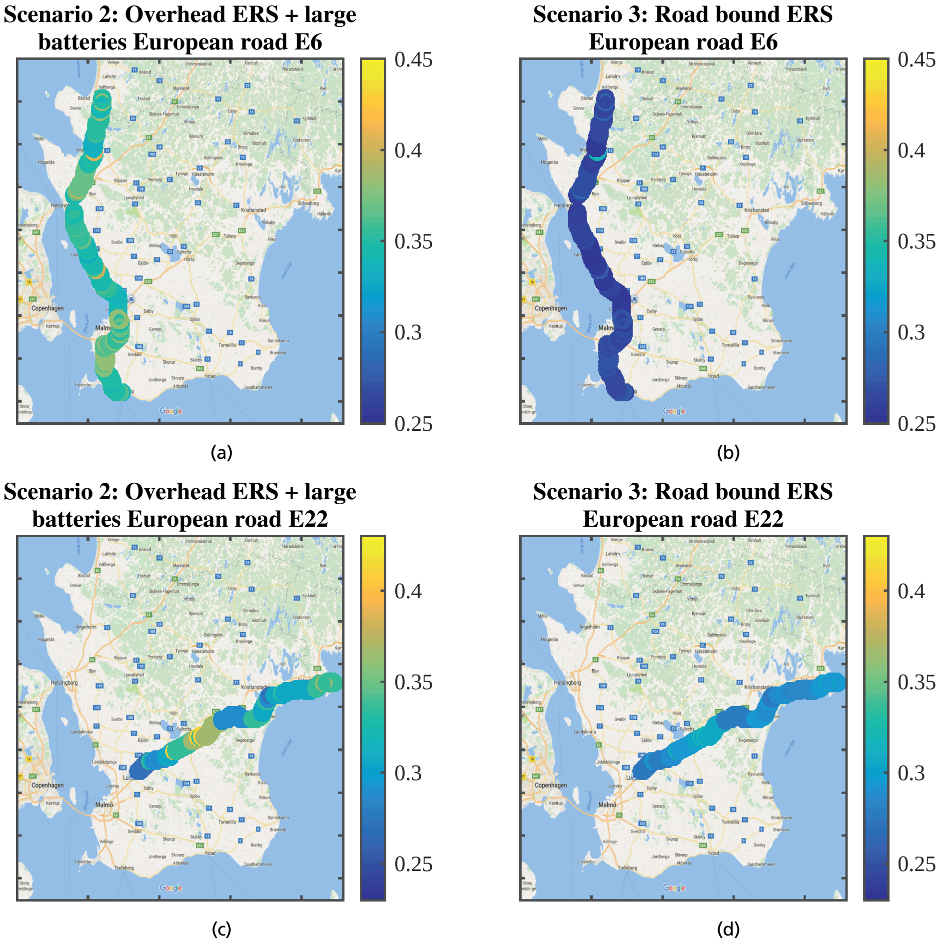

(a) (b) (c) (d)

Figure 5.15: Electromobility equivalent energy cost (C_{emob}) for electrification scenarios 2 and 3 applied to European roads E6 and E22.

estimated as AADT$_{Total}$-AADT$_{Trucks}$.

Figure 5.15 shows the calculated C_{emob} for both scenarios and roads at each point where traffic measurements are available. As it could be expected, for both roads, scenario 2 provides a higher C_{emob} than scenario 3. Slightly more counter-intuitive is the fact that for scenario 2 the E6 (refer to Fig. 5.15a) presents in general a slightly higher C_{emob} than the E22 (see Fig. 5.15c), although it has higher volumes of trucks and cars. However, as previously explained, the higher traffic volumes of cars on the E6 increases the C_{emob} due to the additional depreciation of their on-board components.

On the other hand, when both vehicle types can take advantage of the ERS infrastructure (scenario 3), the higher traffic on the E6 translates into a lower C_{emob} than that of the E22 as shown in Figs. 5.15b and d. Moreover, in general it can be concluded that scenario 3 offers a C_{emob} that is well below C_{fuel}, while scenario 2 in both roads provides a C_{emob} that is around C_{fuel}. This clearly highlights the importance of sharing the dynamic charging infrastructure among as many vehicle types as possible.

5.3.3 Conclusions

From the analysis presented in this section, it is possible to draw several conclusions. The first one is that for roads with traffic volumes above 900 trucks a day, the electrification of only heavy traffic by means of an overhead ERS would result in an electromobility equivalent energy cost that is competitive to that of fossil fuels, under the assumptions made in this study. However, this option does not affect in any way the emissions derived from light duty vehicles. The second conclusion that can be extracted is that if all traffic is to be electrified, the implementation of an ERS that can be used by all vehicle types results into higher societal gains as it decreases the cost of on-board components for cars which are the most numerous vehicle type in most national fleets. Moreover, if the ERS infrastructure is shared among light and heavy vehicles, the amount of roads that would be cost effective to electrify significantly increases, making the technology, and consequently its benefits, accessible to even more vehicles. This last point as well as the conclusions presented in section 5.2.5 highlight the importance of making the dynamic charging infrastructure accessible to light duty vehicles as well.

Chapter 6

Conclusions and future work

6.1 Conclusions

This thesis compiles knowledge from different fields (electrical, mechanical and manufacturing engineering) and applies it to the modeling, optimization and analysis of electromobility systems. In this context, sizing, performance and cost models for PECs, EMs and MTs are presented in Chapter 3. These models are then used in Chapter 4 to optimize the design of an electric powertrain for a passenger vehicle application. Finally, in Chapter 5, the developed cost models are used to analyze the societal cost implications of using different technologies for the electrification of road transport. The objective of this thesis is to develop an understanding, from the component to the system level, of the factors and interactions that affect the performance and cost of electromobility systems.

Due to the wide nature of the studied systems, it is essential to take a cross-disciplinary approach when modeling, optimizing or analyzing them. Suboptimal solutions or misleading conclusions may result from approaching a problem using a single discipline's perspective, as existing deep interactions with other disciplines may be ignored. Thus, a decision taken on a certain component feature from one discipline's point of view may have a severe impact on other aspects of such component. For example, decisions made based on the electromagnetic performance of an EM may affect the selection of manufacturing processes and vice-versa; characteristics and limitations of available manufacturing processes affect the geometrical design of the EM, and thus its electromagnetic performance. An example of this can be seen in section 3.2.6.

Similarly, decisions based on improving the characteristics of a single component can translate into a degradation of performance or an increase in cost of another component and possibly the overall system. For example, operating the EM at high magnetic saturation levels can potentially increase its torque density, but this implies the need of a higher current PEC which drives the cost of the system up. The opposite scenario can also be true, increasing the cost or degrading the performance of a component can result in a better system solution, as shown in Chapter 4, where the addition of a second speed in the transmission (which increases its cost and size) translates into a lower total system cost for the studied case.

In order to provide a fair comparison and to be useful within a complex system optimization scheme, cost models that are computationally efficient and are able to provide a reasonable estimation based on the information available during the pre-design stage are needed. Although traditional cost estimation techniques are able to provide a quite accurate assessment of the cost of a component or a system given an existing design, they tend to be time consuming and not practical to be included inside optimization routines. In this context, one of the main contributions of this work is the development of cost models for a variety of components based on a similar set of assumptions. These models are computationally fast and do not require a final component design. Cross-disciplinary work and cooperation have been essential to the development of such models. The present work benefits from a long standing cooperation between the LTH divisions of Industrial Electrical Engineering and Automation (IEA) and Production and Materials (iProd), as well as with several industrial partners.

It is important to adjust the type and depth of the modeling to the task and resources at hand, so no relevant information or interactions between components is missed but the required computational time remains within reasonable levels. The reliability of the obtained results depends highly on the level of accuracy of the models used. Simultaneously, high fidelity models usually require higher computational times. Finding a good balance between the accuracy and level of detail of the models used and their execution time is specially important if the objective of the study is the optimization of a system, in which case it can be expected that the component models will be evaluated a large number of times, as exemplified in Chapter 4.

A holistic approach that considers the selection and optimization of the different components of the system simultaneously has a better chance of finding solutions closer to a theoretical optimum. The requirements of the optimization should be defined at the system level, in order not to set artificial constraints to the system that can result in sub-optimal solutions. However, this requires good knowledge of the studied system and its intended operation. A clear example of this is presented in Chapter 4, where wheel requirements are set for the optimization of an electric powertrain instead of, for example, requirements on the EM torque or speed.

Taking all these lessons into consideration, another significant contribution of this thesis is the development of an optimization tool for electric powertrains that, given a set of wheel requirements, is able to explore a large space of search, including different EM geometries and powertrain configurations in a time effective manner. This tool does not aim to produce final designs but rather identify areas of interest that are worth to be explored further. In general, conclusions derived from particular case studies optimized by the aforementioned tool cannot be extrapolated to other vehicles, set of requirements and/or initial assumptions as results are highly sensitive to these parameters. Instead, learned lessons should focus on the methodology and approach.

Although electric powertrains are important components in vehicles, influencing in a significant way their performance and cost, they are probably not the factor currently hindering the wide adoption of electrified vehicles. In order to truly enable and accelerate the pace of automotive electrification, a more comprehensive analysis of the road transport system needs to be carried out. A significant portion of this thesis is devoted to perform such analysis with the help of the developed models for different electromobility components as well as best available figures from the literature. From this study, it is possible to conclude that batteries, in particular those needed for LDVs are the main cost driver for the electromobility system. An obvious path, and the current trend, is to make electrified vehicles cost competitive is to lower the cost of battery packs. This can be achieved in a combination of ways, from changes in the battery chemistry to advances in manufacturing methods and economies of scale. However, an alternative path is the large scale deployment of dynamic charging infrastructure. It is shown in Chapter 5 that **if LDV can take advantage of the ERS the societal cost of an electrified road transport system is lower than the current one (based on ICEs) even at higher battery costs than the currently reported values.**

6.2 Future work

The inclusion of wide-bandgap semiconductor devices, such as SiC and GaN, in the semiconductor model presented in section 3.1.1 which currently only includes silicon IGBTs and diodes would be a valuable improvement. In recent years SiC and GaN components have appeared in the market at volumes and prices that make them interesting alternatives to conventional Si devices, especially in applications such as DC-DC converters where the possibility of increasing the switching frequency allows to reduce the size of the passive components.

Another interesting direction for further improvements is the addition of new PEC topologies, such as multilevel converters for driving electrical machines or resonant converters that could be used for DC-DC conversion. Additionally, the inclusion of alternative onboard chargers and new isolated DC-DC converters is of interest when studying the cost effectiveness of the integration of these functions in the powertrain.

The addition of new EM topologies to the database presented in section 3.2, such as induction, reluctance and electrically excited machines would allow studying the impact, both in terms of cost and performance, of machine designs that have different cost sensitivity to commodities and raw materials. Additionally, the inclusion of EM designs involving different manufacturing processes than those currently modeled (e.g. hairpin and fractional slots windings) is an interesting alternative to complement the existing EM models. In a similar fashion, alternative MT topologies and powertrain configurations can widen the space of search and thus the possibilities of finding optimal solutions.

It is also compelling to incorporate alternative cooling concepts that could be used both in EMs and power electronic components, such as inductors and transformers. Improved cooling has the potential to reduce the overall size and cost of these components, resulting in more cost effective and compact solutions. In later years, technologies for direct winding cooling have been developed. These technologies significantly increase the performance of targeted applications, but in order to assess their effectiveness at system level, they need to be considered in the design stage and thus they need to be included in a design and optimization tool like the one presented in this thesis.

A welcome improvement would be the inclusion of components rated for both higher and lower voltages. Recent trends point towards DC-link voltages above 800V, which is about the maximum value that can be achieved with the semiconductor components currently included in the models. In order to accurately model the impact of this increase in voltage, it is necessary to account for the required change in insulation class of the EM's windings as well. Additionally, the inclusion of lower voltage components targeting 48V applications would allow using the existing models in the optimization of mild-hybrids as well.

As there exists significant uncertainty regarding the cost of high power static charging stations as well as inductive dynamic charging infrastructure, the analysis presented in Chapter 5, would be strengthened if more detailed cost models for these components are developed following the methodology outlined in Chapter 3.

Moreover, so far the analysis of the road transport has been focused solely on BEVs. However, the final goal should not be to achieve a fully electrified road transport system but rather a decarbonized and sustainable one. In this context, it would be interesting to include FCEVs as well as bio-fuels in the analysis presented in Chapter 5. Additionally, that analysis can be complemented with a study on how driving patterns and fleet size would be affected in the alternative scenarios by the different vehicle technologies and infrastructures. Furthermore it would be quite interesting, although challenging, to attempt to analyze the transition period from the current state to the one in the proposed scenarios.

Appendix: Fleet assumptions

The results presented in Chapter 5 are somewhat sensitive to the assumptions made regarding the specifications of the different vehicles in the studied scenarios. For this reason, this appendix describes in detail the foundations for such assumptions.

Light duty vehicles represent the largest portion of most nation-wide fleets. In order to find a set of specifications that could be considered a representative average of a LDV in a future electrified fleet, the top-sold 100 vehicle models in Sweden during 2016 are used. The different vehicle classes defined by the European Commission are assigned to one of three groups of battery capacity and traction power specification, as shown in Table 1. It is worth noticing that although the European commission does not subdivide the Multi-purpose and Sport-Utility segments in large and small [129], this is done in this work in order to capture the changes in specifications between vehicles of the same segment but with significant differences in performance. Moreover, premium or luxury vehicles of one class are moved to the group level above. Tables 2 and 3 show the assigned battery capacity and traction power for the most sold vehicles in Sweden during 2016.

Table 1: Assigned specifications for different vehicle classes

Description	Class	Battery Capacity [kWh]	Powertrain Power [kW]
Mini cars	A	40	80
Small cars	B	40	80
Medium cars	C	60	100
Large cars	D	100	120
Multi purpose small car	M-S	60	100
Multi purpose large car	M-L	100	120
Sport utility small cars	J-S	60	100
Sport utility large cars	J-L	100	120

Table 2: Top LDVs sold in Sweden during 2016

	Model	Sales (2016)	Class	Battery Capacity [kWh]	Powertrain Power [kW]
1	VW GOLF	22084	C	60	100
2	VOLVO V70II, S/V90N	21321	E	100	120
3	VOLVO S/V60	16755	D	100	120
4	VOLVO XC60	16266	D	100	120
5	VW PASSAT	15716	D	100	120
6	VOLVO V40N	12691	C	60	100
7	TOYOTA AURIS	7423	C	60	100
8	VW POLO	7091	B	40	80
9	KIA CEE'D	6778	C	60	100
10	SKODA OCTAVIA	5889	D	100	120
11	AUDI A4	5684	D	60	100
12	AUDI A6	5580	E	100	120
13	SKODA FABIA	5482	B	40	80
14	BMW 5-SERIE	5435	E	100	120
15	NISSAN QASHQAI	5145	D	60	100
16	TOYOTA YARIS	5129	B	40	80
17	BMW 3-SERIE	4977	D	60	100
18	KIA SPORTAGE	4625	J-S	60	100
19	VW TIGUAN	4492	J-S	60	100
20	FIAT DUCATO	4174	M-L	100	120
21	MERCEDES E-KLASS	4146	E	100	120
22	VOLVO XC90N	4058	J-L	100	120
23	RENAULT CLIO	4033	B	40	80
24	AUDI A3	3972	C	60	100
25	OPEL ASTRA	3694	C	60	100
26	FORD FOCUS	3612	C	60	100
27	RENAULT CAPTUR	3576	B	40	80
28	TOYOTA RAV 4	3465	C	60	100
29	PEUGEOT 308	3266	C	60	100
30	MERCEDES C-KLASS	3258	D	100	120
31	SEAT LEON	3138	C	60	100
32	TOYOTA AVENSIS	3103	D	100	120
33	KIA RIO	3100	B	60	100
34	HYUNDAI I30	2885	C	60	100
35	PEUGEOT 208	2823	B	40	80
36	SKODA SUPERB	2755	D	100	120
37	DACIA DUSTER	2729	J-S	60	100
38	MITSUBISHI OUTLANDER	2660	J-S	60	100
39	BMW 1-SERIE	2467	C	60	100
40	FORD MONDEO	2279	D	100	120
41	PEUGEOT 2008	2274	B	40	80
42	RENAULT KADJAR	2252	J-S	60	100
43	RENAULT MEGANE	2129	C	60	100
44	MERCEDES CLA	2111	C	60	100
45	MAZDA CX-3	2006	B	40	80
46	BMW X1	1995	J-S	60	100
47	HYUNDAI I20	1993	A	40	80
48	KIA PICANTO	1930	A	40	80
49	MINI HATCH	1874	A	40	80
50	BMW 2-SERIE	1854	C	60	100

Table 3: Top LDVs sold in Sweden during 2016

	Model	Sales (2016)	Class	Battery Capacity [kWh]	Powertrain Power [kW]
51	OPEL CORSA	1846	B	40	80
52	HYUNDAI TUCSON	1823	J-S	60	100
53	FORD FIESTA	1796	B	40	80
54	MERCEDES A-KLASS	1788	B	40	80
55	AUDI A1	1774	B	40	80
56	VW UP!	1765	A	40	80
57	SUBARU OUTBACK	1758	C	60	100
58	AUDI Q5	1757	J-L	100	120
59	SEAT IBIZA	1749	B	40	80
60	MERCEDES GLC	1709	J-S	100	120
61	VW SHARAN	1694	M-L	100	120
62	BMW X3	1609	J-S	60	100
63	DACIA SANDERO	1606	B	40	80
64	AUDI Q3	1485	J-S	60	100
65	MAZDA CX-5	1433	J-S	60	100
66	BMW 4-SERIE	1377	D	100	120
67	MITSUBISHI ASX	1377	C	60	100
68	TOYOTA VERSO	1367	C	60	100
69	FIAT 500	1360	A	40	80
70	SUBARU XV	1336	C	60	100
71	FORD KUGA	1293	J-S	60	100
72	MAZDA3	1293	C	60	100
73	HONDA CR-V	1291	J-S	60	100
74	SUBARU FORESTER	1260	J-S	60	100
75	VW CADDY	1249	M-S	60	100
76	SKODA YETI	1198	C	60	100
77	SUZUKI VITARA	1196	J-S	60	100
78	CITROEN C3	1178	B	60	100
79	HONDA CIVIC	1176	C	60	100
80	KIA OPTIMA	1156	D	100	120
81	KIA SORENTO	1139	J-L	100	120
82	HYUNDAI I40	1025	D	100	120
83	MERCEDES B-KLASS	1010	M-S	100	120
84	VW TOURAN	942	M-S	60	100
85	FORD S-MAX	937	M-L	100	120
86	HONDA HR-V	936	C	60	100
87	AUDI A5	916	D	100	120
88	NISSAN X-TRAIL	901	J-S	60	100
89	TOYOTA PRIUS	887	B	60	100
90	CITROEN C4 PICASSO	883	M-S	60	100
91	KIA SOUL	870	M-S	60	100
92	KIA VENGA	859	B	40	80
93	CITROEN C4	857	C	60	100
94	NISSAN JUKE	854	B	40	80
95	CITROEN C4 CACTUS	844	C	60	100
96	PEUGEOT 3008	842	C	60	100
97	KIA CARENS	839	M-S	60	100
98	TESLA MODEL S	838	E	100	120
99	NISSAN LEAF	836	C	40	80
100	OPEL INSIGNIA	827	D	100	120

From these tables, it is possible to estimate the average battery capacity for new models to be 72 kWh, assuming a real life energy consumption of 0.2 kWh/km [130] and that only 85% of the total capacity can be used in order to extend the life of the battery. This provides a range of about 300 km. It is important to keep in mind that the energy consumption per driven kilometer and thus the electric range depend highly on the driving cycle, weather conditions and auxiliary loads. On the other hand, from a similar calculation, the average traction power is estimated to be 100 kW.

The fast chargers for LDVs are assumed to have the same charging power as Tesla superchargers currently have (120 kW) [131], and their total number is calculated assuming that the density of fast charging stations is five times higher than that of gas pumps along the highways. This results in about 48 vehicles per fast charging point for Sweden and compared to current deployment of fast charging infrastructure would be on the high side [40, 132]. On the other hand, the on-board charger is assumed to be 6.6 kW, which corresponds to the upgraded version available for the Nissan Leaf [133].

In those scenarios where the LDVs can benefit from the ERS infrastructure, their battery capacity is reduced to 15 kWh, which is on the high side of what current plug-in hybrid vehicles offer and should provide a range of around 60 km. This electric range is deemed sufficient to cover intra-city trips as well as to drive from the initial location to the major road where the ERS is available and from it to the final destination. In order to make a LDV capable of charging from the ERS infrastructure, it needs to be equipped with a pick-up and a DC-DC converter. In this work it is assumed that these components are rated for 25 kW, which is about twice the traction power needed for cruising in the highway. This matches the assumption of having ERS only on 50% of the road length (refer to Fig. 5.11).

For city buses the energy consumption is assumed to be 1.2 kWh/km [134], which does not account for the energy needed for heating. Selecting an average battery capacity for electric buses is a challenging task as the optimal capacity depends, among other factors, on the specific route where the bus is expected to operate, number of hours of continuous operation, etc. Since the intention of this work is not to provide an optimal set of specifications for the nation wide bus fleet, it is assumed that the buses need a range of 350 km to cover a full day of operation [135] in mild weather, which results in a required battery capacity of 500 kWh. The charging power required at the depot is 70 kW, which allows to fully charge the bus in 6 h.

When opportunity charging (180 kW) is made available for buses, the installed battery capacity is assumed to be 90 kWh, which provides an electric range of about 60 km. This could for example mean that buses need to charge for 5 minutes at the end stops after 30 minutes of driving. Additionally, in this case it is possible to reduce the required power for the on-board charger, which is set to 6.6 kW as for LDVs.

The assumptions made to define the specifications of the components on-board city buses are similar to those made on other independent studies and available buses/chargers in the market [135–139].

Distribution trucks use somewhere in the range of $0.8 - 1.7$ kWh/km depending on the drive cycle, slopes, load and required power for auxiliary loads. In this work, it is assumed that distribution trucks consume 1.5 kWh/km, which is on the high side of the aforementioned interval, and are equipped with a battery capacity that is sufficient for about 200 km (340 kWh). The charging power required at the depot is set to 30 kW, which allows to fully charge the battery in 10 h.

In those scenarios where opportunity charging is made available for distribution trucks, it is assumed that loading/unloading docks have a standard 3 phase 63 A outlet and that the trucks are equipped with a 43 kW OBC. In these cases, the battery capacity of the distribution trucks can be reduced to provide about 60 km of range (110 kWh). Additionally, the required power at the depot can also be reduced to 10 kW, which allows to fully charge the battery in 10 h.

Long haul trucks on the other hand consume somewhere in the range of $1.2-2.0$ kWh/km. The specific energy consumption, as in the case for distribution trucks, depends on a variety of factors which cannot be accounted for in a general way. In this work it is assumed that long haul trucks consume 1.6 kWh/km. In order to limit the impact of batteries on the payload of the truck, they are assumed to be equipped with 480 kWh, which is enough to provide more than 2 h of continuous driving, after which the truck must stop and replace the tractor for a fully charged one. This tractor-swapping approach requires fast chargers to be available at truck stops. If autonomous tractors are available in the future, this might be a desirable system [140]. If a tractor has used all of its available battery capacity when reaching the truck stop, it requires a charging power of about 400 kW in order to be fully charged within 1 h. On the other hand, if the truck has only been driving for 2 h at 80 km/h, it will be fully charged within 40 min. On top of needing a large number of fast chargers, this system would require to increase the total number of tractors in the fleet to preserve the number of driven kilometers per day. Assuming 8 h shifts, this system would result in only 6 h of driving per tractor, which means that the number of tractors in the proposed solution needs to be $4/3$ of the initial number of tractors in the fleet in order to preserve the number of driven kilometers in a shift. Overnight trucks are assumed to be able to charge at 40 kW, which is enough to provide a full charge in 9 h.

When the long haul trucks are able to take advantage of the dynamic charging infrastructure, their battery capacity can be reduced to 120 kWh which, as in the case of LDVs, provides a range of about 60 km. Moreover, the required power for the fast charging stations can be reduced to 110 kW, which would provide a full charge in less than 1 h. Additionally, the OBC can be reduced to 10 kW while preserving the ability to fully charge the battery overnight in 9 h as in the non-ERS case.

These assumptions have been presented in different seminars to be scrutinized by experts from the automotive industry and changes were made based on the resulting discussions prior to the publication of the different articles. However, it is important to keep in mind that all these assumptions can be challenged and that they do not represent an optimal solution for all applications and cases.

Bibliography

[1] K. G. Høyer, "The history of alternative fuels in transportation: The case of electric and hybrid cars," *Utilities Policy*, vol. 16, no. 2, pp. 63–71, 2008.

[2] C. Anderson and J. Anderson, *Electric and hybrid cars: A history*. McFarland, 2010.

[3] International Energy Agency (IEA), *Global EV outlook 2017: two millions and counting*, 2017. [Online] Available at https://www.iea.org/publications/freepublications/publication/GlobalEVOutlook2017.pdf (Date last accessed 14-November-2017).

[4] British Petroleum (BP), *BP Energy Outlook 2017 edition*, 2017. [Online] Available at https://www.bp.com/content/dam/bp/pdf/energy-economics/energy-outlook-2017/bp-energy-outlook-2017.pdf (Date last accessed 16-November-2017).

[5] Bloomberg New Energy Finance, *Electric Vehicle Outlook 2017*, 2017. [Online] Available at https://about.bnef.com/new-energy-outlook/ (Date last accessed 16-November-2017).

[6] U.S. Energy Information Administration (EIA), *International Energy Outlook 2017*, 2017. [Online] Available at https://www.eia.gov/outlooks/ieo/pdf/0484(2017).pdf (Date last accessed 14-November-2017).

[7] United Nations Framework - Convention on Climate Change (UNFCCC), *Paris Agreement - Status of Ratification*. [Online] Available at http://unfccc.int/paris_agreement/items/9444.php (Date last accessed 14-November-2017).

[8] United Nations Framework - Convention on Climate Change (UNFCCC), *Paris Agreement - Intended Nationally Determined Contributions (INDCs)*. [Online] Available at http://www4.unfccc.int/submissions/indc/Submission%20Pages/submissions.aspx (Date last accessed 14-November-2017).

[9] International Energy Agency (IEA), *CO_2 Emissions From Fuel Combustion Highlights 2017*, 2017. [Online] Available at `https://www.iea.org/publications/freepublications/publication/CO2EmissionsfromFuelCombustionHighlights2017.pdf` (Date last accessed 14-November-2017).

[10] U.S. Department of Energy, *Emissions from Hybrid and Plug-In Electric Vehicles*. [Online] Available at `https://www.afdc.energy.gov/vehicles/electric_emissions.php` (Date last accessed 14-November-2017).

[11] International Energy Agency (IEA), *Key World Energy Statistics 2017*, 2017. [Online] Available at `https://www.iea.org/publications/freepublications/publication/KeyWorld2017.pdf` (Date last accessed 16-November-2017).

[12] P. Liu, R. Ross, and A. Newman, "Long-range, low-cost electric vehicles enabled by robust energy storage," *MRS Energy and Sustainability-A Review Journal*, vol. 2, 2015.

[13] B. Nykvist and M. Nilsson, "Rapidly falling costs of battery packs for electric vehicles," *Nature Climate Change*, vol. 5, pp. 329–33, April 2015.

[14] S. Knupfer, R. Hensley, P. Hertzke, and P. Schaufuss, "Electrifying insights: How automakers can drive electrified vehicle sales and profitability," *McKinsey&Company, Jan*, 2017.

[15] F. Lambert, *Tesla confirms base Model 3 will have less than 60 kWh battery pack option, cost is below $190/kWh and falling*. [Online] Available at `https://electrek.co/2016/04/26/tesla-model-3-battery-pack-cost-kwh/` (Date last accessed 14-November-2017).

[16] R. Sarkar, *Office of Energy Efficiency and Renewable Energy FY 2016 Budget Overview*. [Online] Available at `https://energy.gov/sites/prod/files/2015/03/f20/FY%202016%20Transportation%20Webinar%20%20Presentation.pdf` (Date last accessed 14-November-2017).

[17] U.S. Department of Energy, *EV Everywhere Grand Challenge Blueprint*. [Online] Available at `https://energy.gov/sites/prod/files/2016/05/f31/eveverywhere_blueprint.pdff` (Date last accessed 14-November-2017).

[18] S. M. Lukic, J. Cao, R. C. Bansal, F. Rodriguez, and A. Emadi, "Energy storage systems for automotive applications," *IEEE Transactions on Industrial Electronics*, vol. 55, pp. 2258–2267, June 2008.

[19] S. M. Lukic and A. Emadi, "Effects of drivetrain hybridization on fuel economy and dynamic performance of parallel hybrid electric vehicles," *IEEE Transactions on Vehicular Technology*, vol. 53, pp. 385–389, March 2004.

[20] C. C. Chan, A. Bouscayrol, and K. Chen, "Electric, hybrid, and fuel-cell vehicles: Architectures and modeling," *IEEE Transactions on Vehicular Technology*, vol. 59, pp. 589–598, Feb 2010.

[21] D. Cabezuelo, J. Andreu, I. Kortabarria, I. M. de Alegría, and E. Robles, "Powertrain systems of electric, hybrid and fuel-cell vehicles: State of the technology," in *2017 IEEE 26th International Symposium on Industrial Electronics (ISIE)*, pp. 1445–1450, June 2017.

[22] A. G. Boulanger, A. C. Chu, S. Maxx, and D. L. Waltz, "Vehicle electrification: Status and issues," *Proceedings of the IEEE*, vol. 99, pp. 1116–1138, June 2011.

[23] M. F. Felgenhauer, M. A. Pellow, S. M. Benson, and T. Hamacher, "Evaluating co-benefits of battery and fuel cell vehicles in a community in california," *Energy*, vol. 114, pp. 360 – 368, 2016.

[24] I. TC69, "IEC 61851: Electric vehicle conductive charging system-Part 1: General requirements," *International Electrotechnical Commission (IEC), Tech. Rep., Forecast: October*, 2010.

[25] C. Toepfer, "SAE electric vehicle conductive charge coupler, SAE J1772," *Society of Automotive Engineers*, 2009.

[26] I. M. Jiménez, C. A. Carreras, and G. F. Aznar, "IA-HEV Task 20 Quick Charging Technology: Final report," tech. rep., CIRCE, 2015.

[27] A. Ahmad, M. S. Alam, and R. Chabaan, "A comprehensive review of wireless charging technologies for electric vehicles," *IEEE Transactions on Transportation Electrification*, vol. 4, pp. 38–63, March 2018.

[28] R. Bosshard and J. W. Kolar, "Inductive power transfer for electric vehicle charging: Technical challenges and tradeoffs," *IEEE Power Electronics Magazine*, vol. 3, pp. 22–30, Sept 2016.

[29] H. A. Danielsson and N. G. Vagstedt, *Worlds first electric road opens in Sweden*, 2016. [Online] Available at `https://www.scania.com/group/en/worlds-first-electric-road-opens-in-sweden/` (Date last accessed 11-November-2016).

[30] G. Asplund and B. Rehman, "Conductive feeding of electric vehicles from the road while driving," in *Electric Drives Production Conference (EDPC), 2014 4th International*, pp. 1–9, Sept 2014.

[31] Alstom, *APS - Ground level power supply*. [Online] Available at `http://www.alstom.com/products-services/product-catalogue/rail-systems/`

`Infrastructures/products/aps-ground-level-power-supply/` (Date last accessed 4-May-2017).

[32] Elonroad, *Elonroad Electric Road Technology*. [Online] Available at `http://elonroad.com` (Date last accessed 4-May-2017).

[33] I. S. Suh and J. Kim, "Electric vehicle on-road dynamic charging system with wireless power transfer technology," in *Electric Machines Drives Conference (IEMDC), 2013 IEEE International*, pp. 234–240, May 2013.

[34] S. Jeong, Y. J. Jang, and D. Kum, "Economic analysis of the dynamic charging electric vehicle," *IEEE Transactions on Power Electronics*, vol. 30, pp. 6368–6377, Nov 2015.

[35] N. Sakai, D. Itokazu, Y. Suzuki, S. Sakihara, and T. Ohira, "Single-seater vehicle prototype experiment powered by high frequency electric field on an asphalt-paved roadway," in *2016 6th International Electric Drives Production Conference (EDPC)*, pp. 101–104, Nov 2016.

[36] W. Zhang, S. C. Wong, C. K. Tse, and Q. Chen, "An optimized track length in roadway inductive power transfer systems," *IEEE Journal of Emerging and Selected Topics in Power Electronics*, vol. 2, pp. 598–608, Sept 2014.

[37] T. Tajima, H. Tanaka, T. Fukuda, Y. Nakasato, W. Noguchi, Y. Katsumasa, and T. Aruga, "Study of high power dynamic charging system," in *SAE Technical Paper*, SAE International, 03 2017.

[38] T. Tajima and H. Tanaka, "Study of 450-kw ultra power dynamic charging system," in *SAE Technical Paper*, SAE International, 2018.

[39] E. W. Wood, C. L. Rames, M. Muratori, S. Srinivasa Raghavan, and M. W. Melaina, "National plug-in electric vehicle infrastructure analysis," tech. rep., National Renewable Energy Laboratory (NREL), Golden, CO (United States), 2017.

[40] E. Lorentzen, P. Haugneland, C. Bu, and E. Hauge, "Charging infrastructure experiences in norway-the worlds most advanced ev market," in *EVS30 Symposium. Stuttgart, Germany, EN*, 2017.

[41] J. Smart and S. Schey, "Battery electric vehicle driving and charging behavior observed early in the ev project," *SAE International Journal of Alternative Powertrains*, vol. 1, no. 1, pp. 27–33, 2012.

[42] D. Bowermaster, M. Alexander, and M. Duvall, "The need for charging: Evaluating utility infrastructures for electric vehicles while providing customer support," *IEEE Electrification Magazine*, vol. 5, pp. 59–67, March 2017.

[43] M. Croucher and G. Higgs, *Electric vehicle charging study: a review of options for charging at homes without off-street parking*, 2015. [Online] Available at `http://content.tfl.gov.uk/ev-charging-options-for-homes-without-offstreet-parking.pdf` (Date last accessed 06-March-2018).

[44] M. Neaimeh, S. D. Salisbury, G. A. Hill, P. T. Blythe, D. R. Scoffield, and J. E. Francfort, "Analysing the usage and evidencing the importance of fast chargers for the adoption of battery electric vehicles," *Energy Policy*, vol. 108, pp. 474–486, 2017.

[45] W. Kempton and J. Tomić, "Vehicle-to-grid power fundamentals: Calculating capacity and net revenue," *Journal of power sources*, vol. 144, no. 1, pp. 268–279, 2005.

[46] P. Y. Kong and G. K. Karagiannidis, "Charging schemes for plug-in hybrid electric vehicles in smart grid: A survey," *IEEE Access*, vol. 4, pp. 6846–6875, 2016.

[47] M. Yilmaz and P. T. Krein, "Review of the impact of vehicle-to-grid technologies on distribution systems and utility interfaces," *IEEE Transactions on Power Electronics*, vol. 28, pp. 5673–5689, Dec 2013.

[48] J. A. P. Lopes, F. J. Soares, and P. M. R. Almeida, "Integration of electric vehicles in the electric power system," *Proceedings of the IEEE*, vol. 99, pp. 168–183, Jan 2011.

[49] S. Haghbin, S. Lundmark, M. Alakula, and O. Carlson, "Grid-connected integrated battery chargers in vehicle applications: Review and new solution," *IEEE Transactions on Industrial Electronics*, vol. 60, pp. 459–473, Feb 2013.

[50] M. Yilmaz and P. T. Krein, "Review of integrated charging methods for plug-in electric and hybrid vehicles," in *2012 IEEE International Conference on Vehicular Electronics and Safety (ICVES 2012)*, pp. 346–351, July 2012.

[51] N. Sakr, D. Sadarnac, and A. Gascher, "A review of on-board integrated chargers for electric vehicles," in *2014 16th European Conference on Power Electronics and Applications*, pp. 1–10, Aug 2014.

[52] Renault, *Renault Zoe features*, 2018. [Online] Available at `https://www.renault.ie/vehicles/new-vehicles/zoe/equipment.html` (Date last accessed 06-March-2018).

[53] Z. Tang, Z. Du, and F. Tang, "Electric automobile charging system and electric automobile having same," Jan. 6 2016. EP Patent App. EP20,120,862,873.

[54] A. S. Abdel-Khalik, A. Massoud, and S. Ahmed, "Interior permanent magnet motor-based isolated on-board integrated battery charger for electric vehicles," *IET Electric Power Applications*, vol. 12, no. 1, pp. 124–134, 2018.

[55] W. Lhomme, P. Delarue, T. J. D. S. Moraes, N. K. Nguyen, E. Semail, K. Chen, and B. Silvestre, "Integrated traction / charge / air compression supply using 3-phase split-windings motor for electric vehicle," *IEEE Transactions on Power Electronics*, vol. PP, no. 99, pp. 1–1, 2018.

[56] C. Shi, Y. Tang, and A. Khaligh, "A three-phase integrated onboard charger for plug-in electric vehicles," *IEEE Transactions on Power Electronics*, vol. 33, pp. 4716–4725, June 2018.

[57] G. Domingues-Olavarría, P. Fyhr, A. Reinap, M. Andersson, and M. Alaküla, "From chip to converter: A complete cost model for power electronics converters," *IEEE Transactions on Power Electronics*, vol. 32, pp. 8681–8692, Nov 2017.

[58] T. Friedli and J. W. Kolar, "A Semiconductor Area Based Assessment of AC Motor Drive Converter Topologies," *2009 Twenty-Fourth Annual IEEE Applied Power Electronics Conference and Exposition*, pp. 336–342, feb 2009.

[59] D. A. Neamen *et al.*, *Semiconductor physics and devices*, vol. 3. McGraw-Hill New York, 1997.

[60] A. Wintrich, U. Nicolai, W. Tursky, and T. Reimann, *Application manual power semiconductors, Semikron International GmbH*. ISLE Verlag, Illmenau, 2011.

[61] D. O. Neacsu, *Switching Power Converters: Medium and High Power*. CRC Press, 2013.

[62] R. Burkart and J. Kolar, "Component cost models for multi-objective optimizations of switched-mode power converters," in *Energy Conversion Congress and Exposition (ECCE), 2013 IEEE*, pp. 2139–2146, Sept 2013.

[63] N. Mohan and T. M. Undeland, *Power electronics: converters, applications, and design*. John Wiley & Sons, 2007.

[64] C. W. T. McLyman, *Transformer and inductor design handbook*. CRC press, 2011.

[65] V. C. Valchev and A. Van den Bossche, *Inductors and transformers for power electronics*. CRC press, 2005.

[66] S. Tumanski, *Handbook of magnetic measurements*. CRC Press, 2016.

[67] W. G. Hurley and W. H. Wölfle, *Transformers and inductors for power electronics: theory, design and applications*. John Wiley & Sons, 2013.

[68] F. Fiorillo, *Characterization and measurement of magnetic materials*. Academic Press, 2004.

[69] Cogent - a Tata Steel Enterprise, *Cogent Electrical Steel Datasheets*. [Online] Available at `https://cogent-power.com/downloads` (Date last accessed 5-April-2018).

[70] J. Muhlethaler, J. W. Kolar, and A. Ecklebe, "A novel approach for 3d air gap reluctance calculations," in *8th International Conference on Power Electronics - ECCE Asia*, pp. 446–452, May 2011.

[71] J. Hu and C. R. Sullivan, "Optimization of shapes for round-wire high-frequency gapped-inductor windings," in *Industry Applications Conference, 1998. Thirty-Third IAS Annual Meeting. The 1998 IEEE*, vol. 2, pp. 907–912 vol.2, Oct 1998.

[72] J. Mühlethaler, J. W. Kolar, and A. Ecklebe, "Loss modeling of inductive components employed in power electronic systems," in *Power Electronics and ECCE Asia (ICPE ECCE), 2011 IEEE 8th International Conference on*, pp. 945–952, May 2011.

[73] W. Chen, X. Huang, and J. Zheng, "Improved winding loss theoratical calculation of magnetic component with air-gap," in *Power Electronics and Motion Control Conference (IPEMC), 2012 7th International*, vol. 1, pp. 471–475, June 2012.

[74] J. Reinert, A. Brockmeyer, and R. De Doncker, "Calculation of losses in ferro- and ferrimagnetic materials based on the modified steinmetz equation," *Industry Applications, IEEE Transactions on*, vol. 37, pp. 1055–1061, Jul 2001.

[75] Electronicon, *Capacitors for Power Electronics — Application Notes — Selection Guide*, 2013. [Online] Available at `http://www.electronicon.com/fileadmin/inhalte/pdfs/downloadbereich/Katalog/neue_Kataloge_2011/application_notes.pdf` (Date last accessed 12-December-2015).

[76] P. Fyhr, *Electromobility - Materials and Manufacturing Economics*. PhD thesis, Lund University, 05 2018.

[77] C. L. Whaling, "Technology roadmap analysis 2013: Assessing automotive technology r&d relevant to doe power electronics cost targets," tech. rep., Synthesis Partners, LLC. US Department of Energy, 2013.

[78] M. Olszewski *et al.*, "Evaluation of the 2007 toyota camry hybrid synergy drive system," tech. rep., Oak Ridge National Laboratory, 2008.

[79] G. Bramerdorfer, A. C. Zăvoianu, S. Silber, E. Lughofer, and W. Amrhein, "Possibilities for speeding up the fe-based optimization of electrical machines: A case study," *IEEE Transactions on Industry Applications*, vol. 52, pp. 4668–4677, Nov 2016.

[80] A. Reinap, D. Hagstedt, F. Marquez, Y. Loayza, and M. Alakula, "Development of a radial flux machine design environment," in *2008 18th International Conference on Electrical Machines*, pp. 1–4, Sept 2008.

[81] D. Meeker, *Finite element method magnetics*. [Online] Version 4.0.1 (03 Dec 2006 Build). Available at `http://www.femm.info` (Date last accessed 2-May-2018).

[82] G. Domingues, A. Reinap, and M. Alaküla, "Design and cost optimization of electrified automotive powertrain," in *2016 International Conference on Electrical Systems for Aircraft, Railway, Ship Propulsion and Road Vehicles International Transportation Electrification Conference (ESARS-ITEC)*, pp. 1–6, Nov 2016.

[83] F. Márquez-Fernández, A. Reinap, Z. Huang, and M. Alaküla, "Dynamic evaluation of the overloading potential of a convection cooled permanent magnet synchronous motor," in *2011 IEEE International Electric Machines Drives Conference (IEMDC)*, pp. 13–18, May 2011.

[84] P. Fyhr, G. Domingues, A. Reinap, M. Andersson, and M. Alaküla, "Performance and manufacturability tradeoffs of different electrical machine designs," in *2017 IEEE International Electric Machines and Drives Conference (IEMDC)*, pp. 1–7, May 2017.

[85] F. Magnussen and C. Sadarangani, "Winding factors and joule losses of permanent magnet machines with concentrated windings," in *Electric Machines and Drives Conference, 2003. IEMDC'03. IEEE International*, vol. 1, pp. 333–339 vol.1, June 2003.

[86] T. Y. Lee, M. K. Seo, Y. J. Kim, and S. Y. Jung, "Cogging torque of surface-mounted permanent magnet synchronous motor according to segmented-stator core effect," in *2016 XXII International Conference on Electrical Machines (ICEM)*, pp. 200–206, Sept 2016.

[87] J. Yuan, C. W. Shi, and J. X. Shen, "Analysis of cogging torque in surface-mounted permanent magnet machines with segmented stators," in *2014 17th International Conference on Electrical Machines and Systems (ICEMS)*, pp. 2513–2516, Oct 2014.

[88] B. M. Klebanov, D. M. Barlam, and F. E. Nystrom, *Machine elements: life and design*. CRC Press, 2007.

[89] S. Radzevich and D. Dudley, *Handbook of Practical Gear Design*. Mechanical Engineering Series, Taylor & Francis, 1994.

[90] W. Lewis, "Investigation of the strength of gear teeth," *Gear Technology (USA)*, pp. 19–23, 1992.

[91] American Gear Manufacturers Association, *Fundamental rating factors and calculation methods for involute spur and helical gear teeth*. American Gear Manufacturers Association, 1994.

[92] B. Hamrock, S. Schmid, and B. Jacobson, *Fundamentals of Machine Elements*. McGraw-Hill series in mechanical engineering, McGraw-Hill Higher Education, 2004.

[93] American Gear Manufacturers Association and others, *Geometry Factors for Determining the Pitting Resistance and Bending Strength of Spur, Helical and Herringbone Gear Teeth*. American Gear Manufacturers Association, 1989.

[94] R. Willis, "Lightest-weight gears," in *Product Engineering*, pp. 64–75, January 1963.

[95] GWJ Technology, *eAssistant: the engineering assistant*. [Online] Available at `https://www.eassistant.eu/en/eassistant.html` (Date last accessed 15-June-2018).

[96] R. Andersson, "Electric traction machine design for heavy hybrid vehicles," lic. thesis, Lund University, Lund, Sweden, 2015.

[97] K. Zhou, A. Ivanco, Z. Filipi, and H. Hofmann, "Finite-Element-Based Computationally Efficient Scalable Electric Machine Model Suitable for Electrified Powertrain Simulation and Optimization," *IEEE Transactions on Industry Applications*, vol. 51, no. 6, pp. 4435–4445, 2015.

[98] S. Stipetić, D. Žarko, and M. Popescu, "Scaling laws for synchronous permanent magnet machines," in *2015 Tenth International Conference on Ecological Vehicles and Renewable Energies (EVER)*, pp. 1–7, March 2015.

[99] D. Žarko, M. Kovačić, S. Stipetić, and D. Vuljaj, "Optimization of electric drives for traction applications," in *2017 19th International Conference on Electrical Drives and Power Electronics (EDPE)*, pp. 15–32, Oct 2017.

[100] K. Ramakrishnan, S. Stipetić, M. Gobbi, and G. Mastinu, "Optimal sizing of traction motors using scalable electric machine model," *IEEE Transactions on Transportation Electrification*, vol. 4, pp. 314–321, March 2018.

[101] D. Buecherl, C. Bertram, A. Thanheiser, and H. G. Herzog, "Scalability as a degree of freedom in electric drive train simulation," in *2010 IEEE Vehicle Power and Propulsion Conference*, pp. 1–5, Sept 2010.

[102] J. K. Reed, J. McFarland, J. Tangudu, E. Vinot, R. Trigui, G. Venkataramanan, S. Gupta, and T. Jahns, "Modeling power semiconductor losses in hev powertrains using si and sic devices," in *2010 IEEE Vehicle Power and Propulsion Conference*, pp. 1–6, Sept 2010.

[103] E. Grunditz, *Design and Assessment of Battery Electric Vehicle Powertrain, with Respect to Performance, Energy Consumption and Electric Motor Thermal Capability*. PhD thesis, Chalmers University of Technology, 2016.

[104] M. G. Tehrani, J. Kelkka, J. Sopanen, A. Mikkola, and K. Kerkkänen, "Transmission configuration effect on total efficiency of electric vehicle powertrain," in *2014 16th European Conference on Power Electronics and Applications*, pp. 1–9, Aug 2014.

[105] X. Wu, B. Cao, X. Li, J. Xu, and X. Ren, "Component sizing optimization of plug-in hybrid electric vehicles," *Applied Energy*, vol. 88, no. 3, pp. 799–804, 2011.

[106] P. Caillard, F. Gillon, M. Hecquet, S. A. Randi, and N. Janiaud, "An optimization methodology to pre design an electric vehicle powertrain," *2014 IEEE Vehicle Power and Propulsion Conference, VPPC 2014*, 2015.

[107] A. Schönknecht, A. Babik, and V. Rill, "Electric powertrain system design of bev and hev applying a multi objective optimization methodology," *Transportation Research Procedia*, vol. 14, pp. 3611–3620, 2016.

[108] H. Piechottka, F. Küçükay, F. Kercher, and M. Bargende, "Optimal powertrain design through a virtual development process," *World Electric Vehicle Journal*, vol. 9, no. 1, 2018.

[109] G. Domingues-Olavarria, F. J. Márquez-Fernández, P. Fyhr, A. Reinap, M. Andersson, and M. Alaküla, "Optimization of electric powertrains based on scalable cost and performance models," *IEEE Transactions on Industry Applications*, pp. 1–1, 2018.

[110] Y. L. Vargas, *Highly Dynamic Drives for Electric Hybrid Vehicles: Electric Machine Design and Dynamic Test Method.* PhD thesis, Lund University, 2017.

[111] P. Ngatchou, A. Zarei, and A. El-Sharkawi, "Pareto multi objective optimization," in *Proceedings of the 13th International Conference on, Intelligent Systems Application to Power Systems*, pp. 84–91, Nov 2005.

[112] L. Zadeh, "Optimality and non-scalar-valued performance criteria," *IEEE Transactions on Automatic Control*, vol. 8, pp. 59–60, Jan 1963.

[113] J. Kennedy and R. Eberhart, "Particle swarm optimization," in *Neural Networks, 1995. Proceedings., IEEE International Conference on*, vol. 4, pp. 1942–1948 vol.4, Nov 1995.

[114] Y. del Valle, G. K. Venayagamoorthy, S. Mohagheghi, J. C. Hernandez, and R. G. Harley, "Particle swarm optimization: Basic concepts, variants and applications in power systems," *IEEE Transactions on Evolutionary Computation*, vol. 12, pp. 171–195, April 2008.

[115] P. Fyhr, G. Domingues, M. Andersson, F. J. Márquez-Fernández, H. Bängtsson, and M. Alaküla, "Electric roads: Reducing the societal cost of automotive electrification," in *2017 IEEE Transportation Electrification Conference and Expo (ITEC)*, pp. 773–778, June 2017.

[116] F. J. Márquez-Fernández, G. Domingues-Olavarria, L. Lindgren, and M. Alaküla, "Electric roads: The importance of sharing the infrastructure among different vehicle

types," in *2017 IEEE Transportation Electrification Conference and Expo, Asia-Pacific (ITEC Asia-Pacific)*, pp. 1–6, Aug 2017.

[117] G. Domingues-Olavarría, F. J. Márquez-Fernández, P. Fyhr, A. Reinap, and M. Alaküla, "Electric roads: Analyzing the societal cost of electrifying all danish road transport," *World Electric Vehicle Journal*, vol. 9, no. 1, 2018.

[118] M. Alaküla and H. Bängtson, "Cost analysis of electric land transport," tech. rep., Swedish Electromobility Centre, 2015.

[119] P. Nelson, K. Gallagher, and I. Bloom, "Batpac (battery performance and cost)," tech. rep., Argonne National Lab, 2017.

[120] International Energy Agency (IEA), *Global EV outlook 2018: Towards cross-modal electrification*, 2018. [Online] Available at `https://webstore.iea.org/global-ev-outlook-2018` (Date last accessed 10-October-2018).

[121] M. Smith and J. Castellano, "Costs associated with non-residential electric vehicle supply equipment: Factors to consider in the implementation of electric vehicle charging stations," tech. rep., U.S. Department of Energy, 2015.

[122] Rocky Mountain Institute, *Pulling back the veil on EV charging station costs*, 2014. [Online] Available at `http://blog.rmi.org/blog_2014_04_29_pulling_back_the_veil_on_ev_charging_station_costs` (Date last accessed 04-May-2017).

[123] L. Lindgren, "Analysis of grid connection for electric road systems (ers)," tech. rep., Division of Industrial Electrical Engineering and Automation, Lund University, 2018.

[124] Swedish Energy Agency, *Energy in Sweden - Facts and Figures 2016*, 2016. [Online] Available at `http://www.energimyndigheten.se/en/news/2016/energy-in-sweden---facts-and-figures-2016-available-now/` (Date last accessed 04-May-2017).

[125] Danish Ministry of Transport, *The Danish Transport System - Facts and Figures*, 2011. [Online] Available at `https://www.trm.dk/~/media/files/publication/.../facts-and-figures-netversion.pdf` (Date last accessed 04-May-2017).

[126] Danish Energy Agency, *Energy Statistics 2014*, 2016. [Online] Available at `https://ens.dk/sites/ens.dk/files/Statistik/energystatistics2014.pdf` (Date last accessed 04-May-2017).

[127] European Comission, *Climate Action: Reducing CO2 emissions from passenger cars*, 2016. [Online] Available at `https://ec.europa.eu/clima/policies/transport/vehicles/cars_en` (Date last accessed 04-May-2017).

[128] Trafikverket (Swedish Transport Administration), *PMSV3 Online tool.* [Online] Available at `https://pmsv3.trafikverket.se/` (Date last accessed 04-May-2017).

[129] European Commission, *REGULATION (EEC) No 4064/89 MERGER PROCEDURE*, 2011. [Online] Available at `http://ec.europa.eu/competition/mergers/cases/decisions/m1406_en.pdf` (Date last accessed 11-August-2018).

[130] U.S. Department of Energy, *The official U.S. Government source for fuel economy information*, 2017. [Online] Available at `https://www.fueleconomy.gov` (Date last accessed 02-February-2017).

[131] M. Longo, D. Zaninelli, F. Viola, P. Romano, R. Miceli, M. Caruso, and F. Pellitteri, "Recharge stations: A review," in *2016 Eleventh International Conference on Ecological Vehicles and Renewable Energies (EVER)*, pp. 1–8, April 2016.

[132] International Energy Agency (IEA), "Nordic EV outlook 2018: Insights from leaders in electric mobility," 2018.

[133] Nissan Retail Group, *Nissan Leaf charging options.* [Online] Available at `https://www.nissanretail.co.uk/new-nissan-cars/electric-vehicles/nissan-leaf/charging-options/` (Date last accessed 11-August-2018).

[134] L. Lindgren, *Full electrification of Lund city bus traffic: a simulation study*, 2015. [Online] Internal Report. Available at `https://www.iea.lth.se/publications/Reports/LTH-IEA-7255.pdf` (Date last accessed 06-July-2018).

[135] Z. Gao, Z. Lin, T. J. LaClair, C. Liu, J.-M. Li, A. K. Birky, and J. Ward, "Battery capacity and recharging needs for electric buses in city transit service," *Energy*, vol. 122, pp. 588 – 600, 2017.

[136] O. Olsson, A. Grauers, and S. Pettersson, "Method to analyze cost effectiveness of different electric bus systems," in *EVS29 International Battery, Hybrid and Fuel Cell Electric Vehicle Symposium. Montreal*, pp. 1–12, 2016.

[137] M. Rogge, S. Wollny, and D. U. Sauer, "Fast charging battery buses for the electrification of urban public transport—a feasibility study focusing on charging infrastructure and energy storage requirements," *Energies*, vol. 8, no. 5, pp. 4587–4606, 2015.

[138] Volvo AB., *Volvo 7900 electric specifications.* [Online] Available at `https://www.volvobuses.co.uk/en-gb/our-offering/buses/`

`volvo-7900-electric/specifications.html` (Date last accessed 11-August-2018).

[139] InsideEVs, *MAN Lion's City 12E Electric Bus Debuts At The 2018 IAA*, 2018. [Online] Available at `https://insideevs.com/man-lions-city-12e-debuts/` (Date last accessed 10-October-2018).

[140] Volvo AB., *Introducing Vera: the future of autonomous transport*. [Online] Available at `https://www.volvotrucks.com/en-en/about-us/automation/vera.html` (Date last accessed 11-August-2018).

Printed by Media-Tryck, Lund 2018 NORDIC SWAN ECOLABEL 3041 0903

LUND
UNIVERSITY

Lund University
Faculty of Engineering
Department of Biomedical Engineering
Division of Industrial Electrical Engineering and Automation
ISBN 978-91-88934-95-6
CODEN: LUTEDX/(TEIE-1090)/1-169/(2018)

9 789188 934956